EXPERIMENTAL OBSERVATION OF INTERNAL AND EXTERNAL KINKS IN THE RESISTIVE WALL MACHINE

by

William F. Bergerson

A dissertation submitted in partial fulfillment of
the requirements for the degree of

Doctor of Philosophy

(Physics)

at the

UNIVERSITY OF WISCONSIN–MADISON

2008

ACKNOWLEDGMENTS

To begin, it is paramount to point out the impossibility of adequately recognizing everyone properly who deserves credit. The list of those who deserve thanks extends well beyond these pages.

First and foremost I would like to thank Professor Cary Forest for taking me onto the project and helping me through the years with my development. Our conversations have helped me immeasurably with determining the nature of an experimentalist's job and function within the scientific community and furthered my education. Beyond the mentoring, his ability to receive initial and continuing funds for the project in this day and age of reduced or eliminated budgets is impressive to say the least. For all the above I am grateful.

Roch Kendrick deserves recognition and gratitude as well. While Dr. Forest fostered my intuition towards the physics of the problem at hand, Mr. Kendrick nurtured my grasp of the problem's physicality. I am indebted to his training in the laboratory and enabling me to build the internal diagnostic array. Naming just one diagnostic though is a discredit to everything else. Plasma experiments run on electricity and more electricity. I am proud to say that my ability to test and fix equipment that rolls into the laboratory is solely through his training regardless of the equipment having a 10 A 120 V single phase or a 50 A 480 V three phase plug that goes into the wall. Apart from the lessons he passed along, he also contributed a fantastic amount of time and energy to building and maintaining the machine as well.

When I started out on the project there was no data acquisition system. Developing the DAQ system as it stands today was only possible because Rob O'Connell and Paul Wilhite answered my constant and many questions about digitizers, MDSplus infrastructure, and writing code to wrapper function calls.

Also lacking when I started working in the laboratory was a bias system for the plasma current. Steve Oliva and I began working together on the vacuum system and commissioning of the voltage control bias circuit. Needs evolved and eventually he guided me in building the current controlled bias network. Without his continual answering of my questions there would be no improvement of the system and little ability to cleanly analyze the resistive wall mode. I am proud of the upgrade and remain humbled to have been invited to present its abilities to the MST engineering group.

As the laboratory took shape and analysis took the place of construction I worked closely with Dr. John Sarff and Professor Chris Hegna. Dr. Sarff taught me how to translate 5 Mbytes of data into the plots presented herein. Professor Hegna kept the door open after I finished classes and helped correlate the data to theory. Neither failed to answer the phone or the knock at the door to discuss the problems from either a theoretical or experimental perspective. My development as an experimentalist would be stunted without this mentoring.

The personal associated with the Madison Symmetric Torus also deserve thanks. I am indebted to being able to find so many dedicated and knowledgeable professionals down the hall from my office. I think I knocked on everyone's door at one point or another with questions ranging from physics to engineering to construction. Their willingness to share their time and talent will not be forgotten.

To my lab partner I wish the best of luck for a speedy finish and sound thesis. I hope the new probe work resolves questions raised herein.

Graduate school is tough, but made easier by one's peers. Drs. Nornberg, Spence, Bayliss, and Anderson were all senior students or recently graduated when I began and helped me navigate my way through the stormy waters. For the early years of working together and later years of just talking at the 'dice I am lucky to have had Drs. Tregre and Rocks around. Finally, I would be remise to not acknowledge Ms. Lefkow for her sharp commentary and observations regarding graduate school. Conversing was always a breath of fresh air.

In the laboratory itself, many undergraduates came through the doors and did great work. Brian Grierson was with us early on and has gone onto his own path and continued to bring commitment and dedication to the job. Sam Stambler deserves particular recognition for his work on the bias upgrade. Despite the time constraints inherent to being an undergraduate, he completed graduate level workmanship and his astute conversation saved us from going down the wrong direction many times. It was a joy to work with him while he was here in Wisconsin. Working in the lab without him has been less productive and enjoyable.

To my friends and family who stopped asking when I was going to graduate, thank you. For the others - I am graduating soon, I swear. Jest aside, without their continual support, graduate school would have been that much harder. They always helped me remember that graduate school is but one path of many.

And finally, thanks most to Sarah. From the sporadic evening burrito deliveries to the constant support you were and are fantastic.

Per Ardua Ad Astra

TABLE OF CONTENTS

Page

LIST OF TABLES

LIST OF FIGURES

Figure Page

Figure Page

NOMENCLATURE

MHD the acronym for magnetohydrodynamics, the study of the dynamics of electrically-conducting fluids.

RDR the acronym for the Rosenbluth, Dagazian, and Rutherford theory of internal kinks.

KS the acronym for the Kruskal and Shafranov theory of external kinks.

PFN the acronym for Pulse Forming Network. An electrical circuit used to deliver constant current for set duration.

PWM the acronym for Pulse Width Modulation. A type of electrical circuit in which the amount of current is controlled by the duration that a switch is on.

G Gauss, a unit of measure for magnetic inductance.

ABSTRACT

A cylindrical line tied screw pinch has been constructed at the University of Wisconsin-Madison with the goal of exploring the magnetohydrodynamic stability of current driven kinks in association with varying boundary conditions. The first plasma was created in the spring of 2004, and several milestones have since been achieved. Magnetohydrodynamic stability has been explored in relation to four different boundary conditions. In addition, a technique to precisely control the amount of current in the plasma throughout the pulse has been developed.

Internal kinks are observed to become unstable and grow when the safety factor $q = \frac{4\pi^2 r^2 B_z}{\mu_0 I_p(r) L}$ falls below 1 in the plasma. One internal mode has an $m = 1$ symmetric eigenmode peaked in the middle of the machine. The second internal mode is not symmetric and has an $m = 1$ eigenmode peaked at one end. The presence or absence of a conducting wall at the boundary does not substantially alter the growth or onset of these modes. The antisymmetric mode is noted to dominate the plasma when the current profile is undergoing fast relaxation events suggestive of reconnection. Experiments with two different wall conductivities have been carried out and the resistive wall mode has been identified. The resistive wall mode becomes unstable when the safety factor at the edge of the plasma is close to 1 and has a growth rate well correlated to predictions based on the wall conductivity and plasma parameters.

Chapter 1

Introduction

Magnetic pinches have a history which dates back to the beginning of fusion research. Controlling a plasma with a pinch appeared to be a straightforward path towards fusion energy. The high temperature and pressure inherent to a fusion reaction would be contained by the magneto-hydrodynamic (MHD) forces found within a pinch device. In the 1950s experiments around the world were underway to produce a controlled fusion reaction. These experiments initially failed to produce a sustainable reaction because of reoccurring instabilities that develop in the plasma.

A magnetic pinch is a configuration in which a current in a plasma and its own magnetic field interact through $J \times B$ forces to counter the outward push of the plasma pressure. A larger plasma current allows one to contain a larger plasma pressure. The logical end to this scenario is the containment of a plasma whose pressure is great enough to support a continuous fusion reaction. It should be stressed that it appeared one only needed a sufficiently large current to balance the fantastic plasma pressure associated with fusion.

The approach of using a plasma current to interact with its magnetic field can be applied in either linear or toroidal geometries. In the toroidal approach, both tokamaks and reversed field pinches (RFPs) utilize a plasma current to constrain the pressure within the plasma itself. Linear devices are classified as a z (Fig. 1.1), theta (Fig. 1.2), or screw-type (Fig. 1.3) pinch. Basic schematics for the different linear devices are supplied. Inspection of Figs. 1.1, 1.2, and 1.3 indicates that the name of the device denotes the direction along which current is flowing.

The dominant approach was the z pinch but attempts were also made with the theta pinch. In the z pinch, a cylindrical plasma carries a large axial current. The resulting azimuthal magnetic field couples with the current to produce a $J \times B$ force inwards towards the cylinder axis. The

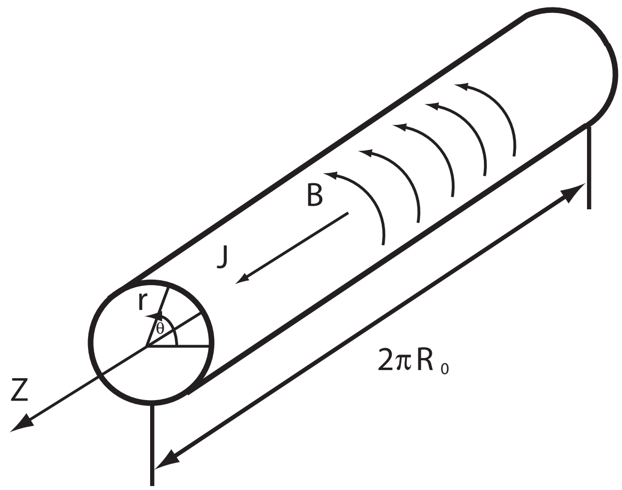

Figure 1.1 In a z pinch an axial current produces an azimuthal magnetic field. Figure from [15].

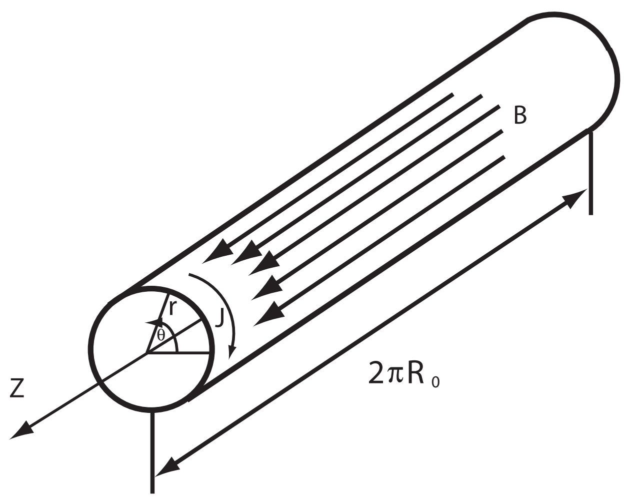

Figure 1.2 In the theta pinch, current flows in the azimuthal direction and the accompanying magnetic field is along the machine axis. Figure from [15].

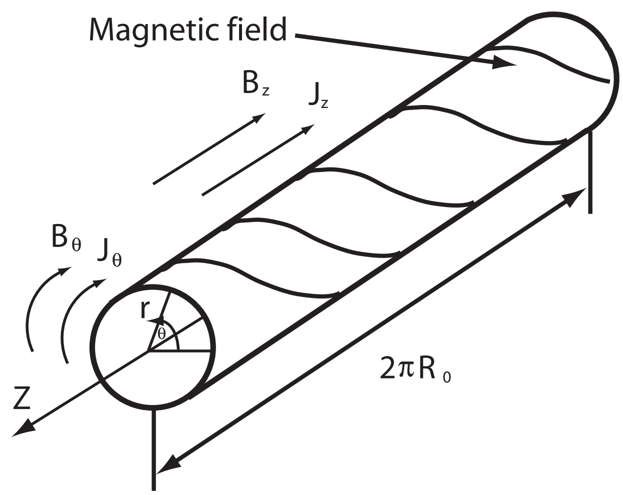

Figure 1.3 The screw pinch has current flowing in both the axial and azimuthal direction. The resulting magnetic field is twisted about the machine axis. Figure from [15].

outward plasma pressure is bounded by the inward $J \times B$ force. The theta pinch exploits the same relationship, but with an inversion in the orientation of the current and magnetic field. In the theta pinch, the current is in the azimuthal direction of a cylinder, while the magnetic field is along the axis. In both cases the plasma current interacts with its own magnetic field to pinch the plasma column into itself. A third variant to the pinch is the screw pinch. A screw pinch can be created by applying an axial magnetic field to a z pinch.

While the pinch held much promise, the concept evolved beyond linear devices into toroidal devices. The linear experiments all experienced variants of the same phenomena. The current column becomes unstable and dissociates. The z pinch is unstable to the sausage mode which is a runaway localized pinch within the current column. The localized pinching chokes the current column, much like two sausages being separated by twisting. A choke at one point in the column ultimately lead to a speedy disruption of the entire current column. This localized pinch instability, not global confinement, actually produced the majority of fusion neutrons measured in the early experiments.

The axial field in a screw pinch stabilizes the sausage mode but presents a new instability known as the kink for its physical ability to kink the current column out of the linear axial plane.

The analogy often used describes a string held between one's hands and twisted. After enough twisting, the string suddenly buckles (kinks) outward and redistributes the twist so that the string is twisted on itself. In the screw pinch, the magnetic field lines will kink if twisted past a certain point. The plasma column, streaming along the now twisted field lines, will disrupt by hitting the containment vessel.

It is important to stress that the above description, field lines buckling into the containment vessel, is exclusively related to the external kink. Kruskal and independently Shafranov (hereafter referred to as KS) [34, 59] analyzed the screw pinch and related quantifiable plasma parameters to the stability of the external kink. KS theory considers a plasma column, surrounded by vacuum in which the external kink creates a uniform helical displacement of the plasma. The displacement produces a hallmark B_r signature that is measurable outside the plasma.

The external kink is not to be confused with the internal kink. Kinks can have internal or external characteristics. Internal kinks have a similar helical structure and displacement, only inside the plasma. The plasma boundary is not shifted and no signature of B_r can be observed outside the plasma. Both internal and external kinks (without a conducting wall nearby) have growth rates related to the Alfvén time [34, 59, 52] and an instability regime governed by the safety factor q. Generally q is expressed as

$$q(r) = rB_z/RB_\theta, \tag{1.1}$$

where r is the minor radius and R the major radius. Essentially q is a measure of the twist in the field lines. The appropriate definition of q for finite length cylindrical plasmas is

$$q(r) = \frac{4\pi^2 r^2 B_z}{\mu_0 I_p(r) L} \tag{1.2}$$

where the radius of the plasma is given by r, $I_p(r)$ is the plasma current inside radius r, and L is the length of the plasma. When $q < 1$ inside the plasma, an internal $m = 1$ kink is unstable. External $m = 1$ kinks are unstable when $q_a < 1$, where $q_a \equiv q(a)$ is the safety factor at the plasma boundary. In either expression of the safety factor, it is obvious that as B_z is raised, q increases. Controlling B_z has long been a basic approach to pinch stability.

The KS theory of external kinks and the Rosenbluth, Dagazian, and Rutherford [52] theory (hereafter referred to as RDR) of internal kinks only consider long cylindrical geometries. Any boundary condition at the end of the cylinder is neglected. This is an appropriate assumption for a long cylinder or torus. However, with a finite cylindrical system line tying considerations may be relevant. In a line tied system there is a conducting boundary at the ends of a cylindrical system. The endplates in the system constrain the plasma displacement vector ξ such that $\xi = 0$ at the ends. The effect of line tying is always stabilizing and is not included in the KS or RDR theory. Considerations of line tying to the stability of kinks is discussed in Chapter 2.

Putting aside line tying considerations for the moment, fusion scientists realized linear pinches could not control or sustain a fusion reaction as they were grossly unstable and needed modification. In principle, a perfect conductor surrounding a screw pinch stabilizes the external kink. The B_r field elicits an eddy current response from the wall. The inductive response of the wall is identical in magnitude but opposite in direction and pushes the kink back into place. In a perfectly conducting wall the eddy currents responsible for B_r never decay away. The problem arises when one considers a real wall with finite conductivity. The kink is stabilized, but only so long as the eddy currents have not resistively decayed away.

If a conventional (resistive) wall is used to stabilize the external kink, the resulting instability is renamed the Resistive Wall Mode (RWM). The RWM is essentially the same instability as the ideal external kink previously described; however, the growth of the mode is now dependent on the time-scale at which flux can leak through the wall. On the time-scale of the wall $\tau_w = \mu_0 \sigma_w r_w \delta_w$ (σ_w is the conductivity, r_w is the wall radius, and δ_w is the wall thickness) flux soaks through the wall and provides a mechanism by which the plasma can access the free energy available to the external kink. For decades, the no wall kink and RWM placed a fundamental limit on plasma performance. As new configurations were developed and explored over the ensuing years, these instabilities restricted plasma performance. The no wall kink can be particularly destructive. Its fast Alfvénic time scale means that once initiated, little can be done to quell the resulting destruction of the current column. The inductive response from a current of this magnitude suddenly disrupting would be an engineering calamity.

The fusion community may be lessening their concern for the RWM as plasma rotation is known to stabilize the mode and active feedback gains acceptance and ability to quell the instability. Yet, the mode is of intrinsic interest to basic plasma physics. Furthermore, research into resistive effects on stability [11, 30], current profile effects [42, 43], and coupling between internal and external kinks are active areas of research.

This Thesis presents data measured on the Resistive Wall Machine (ReWM), a line tied screw pinch constructed to explore MHD. By driving current along the axis of a solenoidal field, current driven MHD instabilities are created and studied. It has been found that the no wall and RWM kinks become unstable when the magnetic field lines are twisted past a critical value inside or at the edge of the plasma, respectively. The result is significant not only as a stepping stone towards stabilizing the RWM in a line tied geometry, but also because it allows facile study of these modes in comparison to larger devices.

The rest of the chapter is organized as follows. First a review of the history of early pinch devices is given in Section 1.1. Both linear and toroidal experiments are discussed. It should be noted that the fundamental interest in the pinch warranted devices being constructed around the world. In Section 1.2 current research initiatives on toroidal devices into the RWM are reviewed as well as the differences between the ReWM and the machine it most closely resembles in terms of construction. Finally, the long term goals of the project and outline to the Thesis are found in Section 1.3.

1.1 Early Pinch Experiments

Colgate, Ferguson, and Furth claim the first experimental observation of the external $m = 1$ kink instability [9]. In the experiment a bias was applied across a cylinder pre-filled with deuterium to produce a plasma current. A solenoid wound around the vacuum vessel supplied an axial magnetic field. The diagnostics were two azimuthal flux loops and one axial flux loop. A net translation in the current column yields a clear $m = 1$ characteristic in B_θ. Changes in B_z result when the linear current column kinks into a helical structure that acts as a secondary solenoid. Comparison of the two azimuthal loops in conjunction with anomalous changes in B_z produce a time resolved signature of the kink in the current column. No explicit growth rate is reported; however, inspection of the magnetic traces indicates an Alfvénic time scale. Mode onset is noted to confirm the predictions of Rosenbluth [51], who produced theory analogous to KS.

A series of screw pinch devices at Los Alamos titled Columbus found additional evidence for the kink instability [66, 40]. Fig. 1.4 details the construction of Columbus II. Columbus II has a length of 30 cm and diameter of 10 cm and is capable of delivering a peak current of 800 kA in 2.2 μs while a surrounding solenoid produces an axial field up to 500 G. Columbus was designed to study fusion, not MHD. As such, the experimenters anecdotally report the plasma being $m = 1$ kink unstable amidst a prodigious number of neutron counts. No clarification is made as to weather the kink is internal or external in the machine.

Columbus T-1, was built to explicitly test if the kink could be stabilized by a conducting wall [3]. This machine, 6 m long and 15 cm in diameter, produces short lived plasma pulses (60 μs) grossly unstable to the kink. A 15 mm aluminum wall surrounds the plasma in an attempt to stabilize the kink. Analysis carried out by a combination of B_θ and B_z flux loops indicate a mode with helical structure. The mode is referred to as a spiral instability with steady-state motion or a large amplitude transverse Alfv́en wave. From the positioning of the probes it is ambiguous if the mode described is an internal or external mode. The rapid disassociation of the plasma in comparison to the wall time indicates that the plasma was not stabilized by the think aluminum wall.

Another version of the Columbus pinches was Columbus S-4. This cylindrical device was 13 cm by 61 cm with an external solenoid to provide an axial field. The discharge tube itself was porcelain. Burkhardt and Lovberg carried out basic studies on this device and noted a helical deformation in the current column consistent with an $m = 1$ kink. Furthermore, the group reported that additional axial field suppressed the $m = 1$ kink [5]. Onset criteria is not reported beyond being within expected values from theory.

A final pair of linear magnetic pinches are from the international community. In the first, a Russian group investigated the stability of the screw pinch [25]. The apparatus is shown in Fig. 1.5. The cylinder is roughly 20 cm in diameter and 80 cm in length. Between the plasma region and

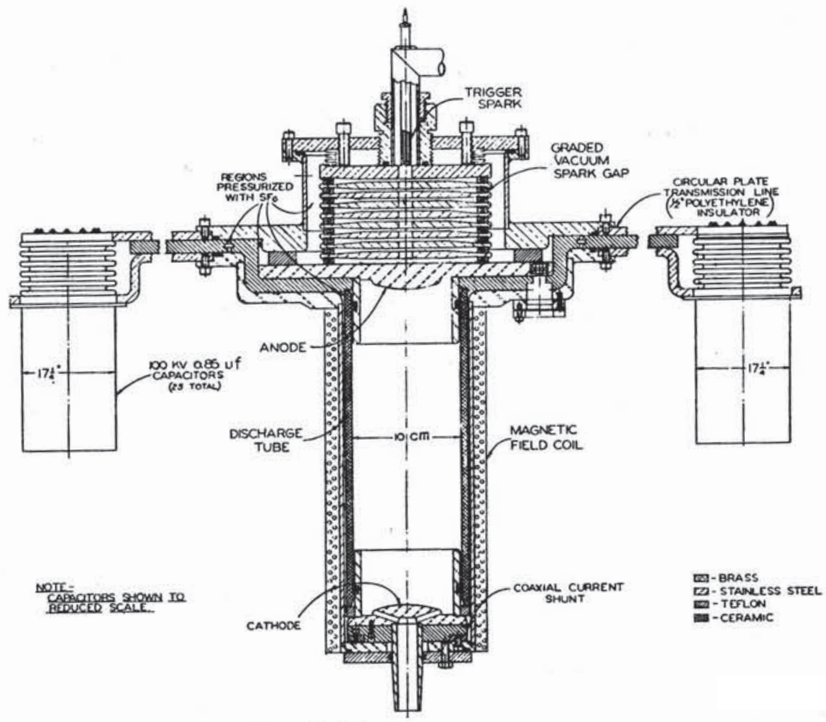

Figure 1.4 A schematic of the Columbus II machine at Los Alamos laboratory. Columbus II was one of the early linear pinch devices that observed a kink instability when plasma currents exceeded a critical value. Figure taken from [66].

surrounding solenoid is a 5 mm stainless steel tube for coaxial return of current. The experimental group found the current column to be stable so long as the KS criteria is not violated. Here again the probe setup on the machine allows the experimenters to look for either internal or external kinks. That the group compares the results to KS theory suggests that external kinks are observed.

The second example of the international effort directed towards plasma physics is a French group who sought mainly to test previously reported findings. In Reference [2], the group built a modest sized linear device, 14 cm radius and 90 cm length, with an external solenoid to produce an axial field and carried out fast photography studies on plasmas. They report optical evidence of the sausage instability when no axial field is used. With an axial field, the sausage mode is

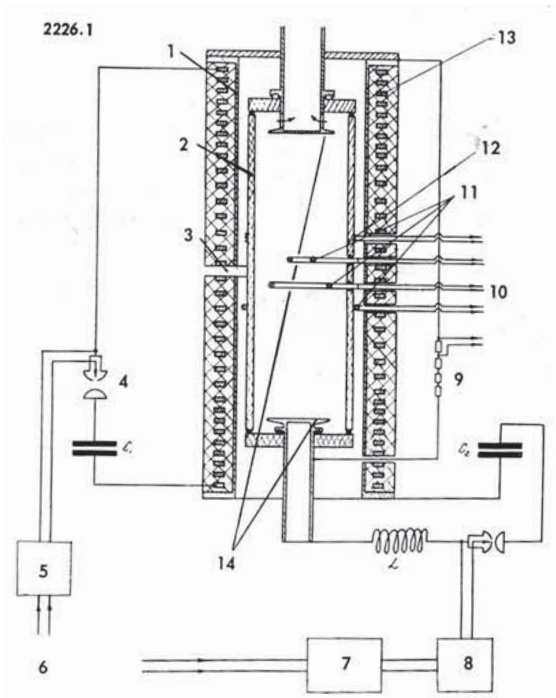

Figure 1.5 A schematic of a z pinch used for fusion studies in Russia. 1, coaxial return conductor; 2, porcelain tube; 3, slot; 4, spherical spark gap; 5, trigger circuit; 6, control board; 7, synchronization circuit; 8, trigger circuit; 9, voltage divider; 10, to oscillograph; 11, current measurements; 12, coil to measure axial magnetic field; 13, solenoid for axial magnetic field; 14, electrodes. Probe position allows for identification of either internal or external kinks. Figure taken from [25].

stabilized and longer discharges are noted. Clear identification of the kink mode is difficult as only a narrow window is available for photographic studies. However, the authors report that at the time of dissociation the plasma is grossly unstable to the external kink.

As mentioned in the introduction, the magnetic pinch is applicable in both linear and toroidal devices. Thus far these early experiments have all reported onset of the kink, either internal or external, in a linear device. The external kink though is not exclusive to cylindrical geometry. The theory of the external kink is a general instability dependent on the amount of twist in a field line, not the geometry of the surrounding machine. In keeping with the fundamental nature of the external kink instability, it should be no surprise to see identification of the mode in early toroidal geometries. The ZETA machine, built in England, was a large torus with a major radius of approximately 10 feet and minor radius of 2.5 feet. The machine is shown in Fig. 1.6. It is reported that

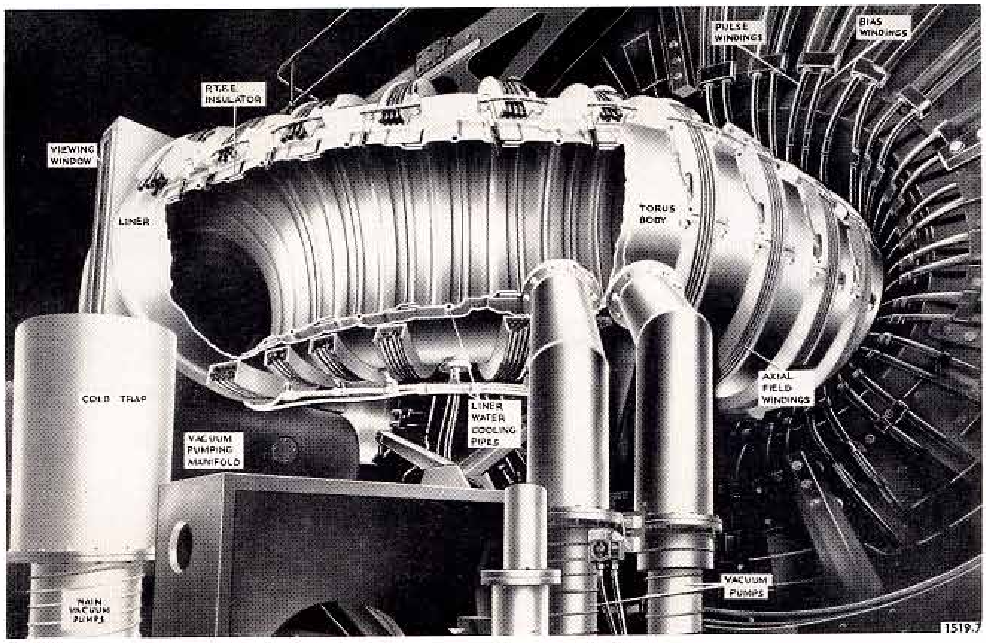

Figure 1.6 A cut away view of Zeta in which a quarter turn of the machine is visible. Note the large electromagnets toward the background surrounding the vessel tube. Figure taken from [6].

instabilities are numerous with a small axial magnetic field [6]. In particular when the threshold of external kink stability is surpassed the resistance and fluctuations increase dramatically.

Another torus, this one built in Russia, also found evidence of the kink instability. This device had a major and minor radius of 50 cm and 13 cm, respectively. A photo of torus in seen in Fig. 1.7. Relying on fast photography of the plasma, a helical band displaced from the magnetic axis is reported [12]. Additionally, as the axial field is decreased the net duration of the pulse is reduced and stability impaired.

A final identification of the external kink took place in a toroidal device in England [1]. The laboratory made a concerted effort to produce an external kink and then attempt to stabilize it with an outer conducting wall. The principle diagnostic was rapid photography. The plasma column, oval in shape and seen in Fig. 1.8, has a minor radius of 6 in. The vacuum chamber consisted of an inner layer of glass and outer layer of metal. The group reports fantastic photographic evidence of the kink, shown in Fig. 1.9, and notes the difficulty they had in effecting any stabilization with the conducting wall. Only with the largest physical discharges is any mitigation of the external kink

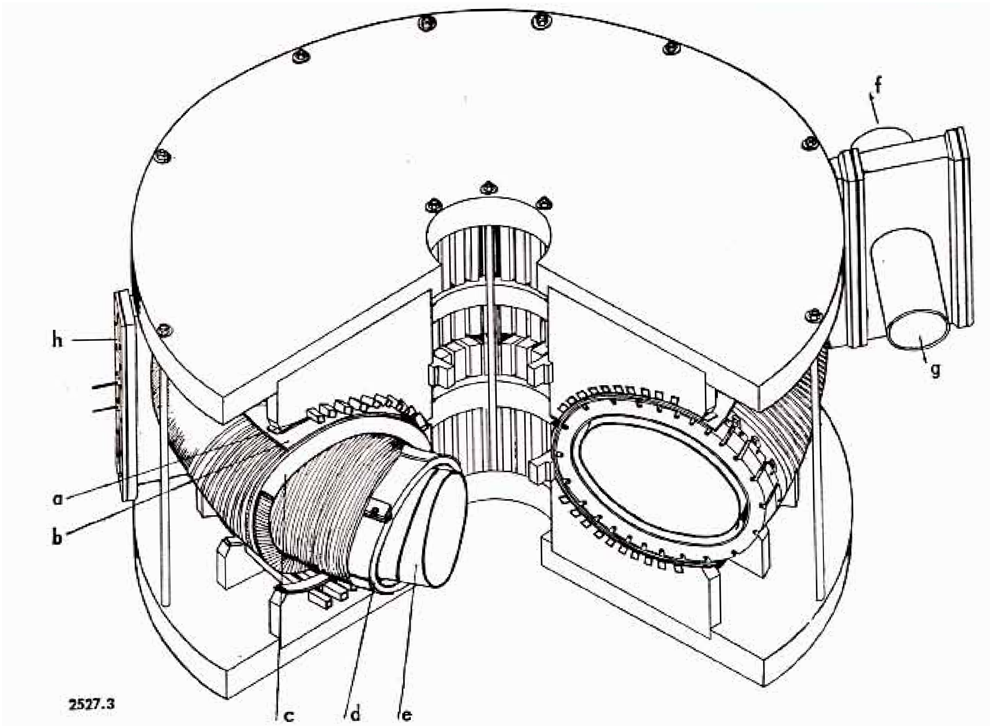

Figure 1.7 A schematic of a torus experimented with in Russia. At a, coil for vortex electric field; b, copper shield; d, a copper stabilizing coil; e, vacuum chamber made from a high resistance ally; f and g, pumping ports; h, window for probe insertion. Figure taken from [12].

found. This result is reinforced by the theory of the external kink in conjunction with a perfectly conducting wall. Only with a narrow gap between the plasma and wall can any measurable increase in stability by coupling the plasma to the wall eddy currents be achieved.

The early experimental devices leave many questions unanswered. All share a common trait that the creation and ability to maintain an axial current are intertwined. In either the linear or toroidal pinches a voltage is applied to break down and bias gas to produce a plasma and current. The current itself mitigates the plasma from neutralizing. The subsequent kink destroys the current column and also serves to neutralize the plasma. Quite simply these machines are ill posed to investigate what happens after the plasma kinks because the kink itself typically eliminates the current column which maintains the plasma. In keeping with this approach, these experiments are all very transient in shot lifetime. The rapid kink action, a result of very large, uncontrolled current

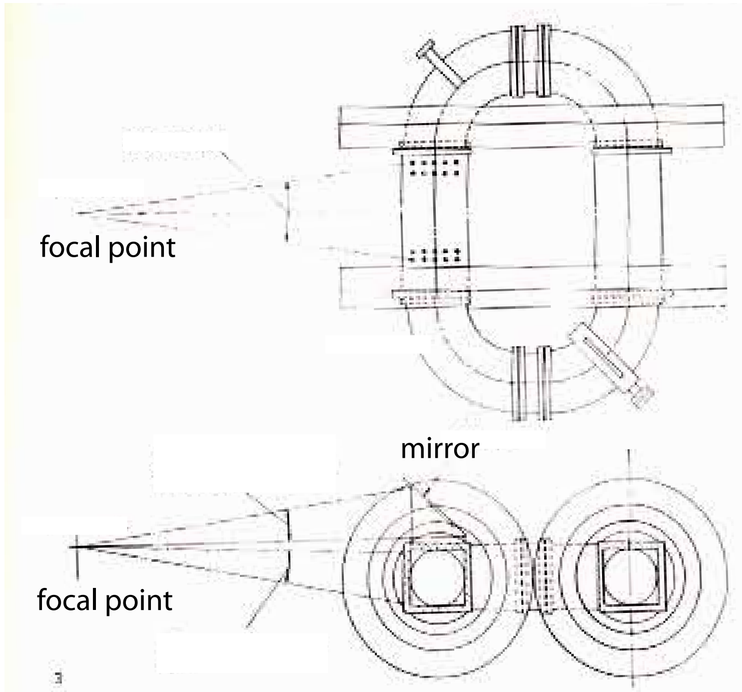

Figure 1.8 A top down schematic of another toroidal device in England. The magnets are the overdrawn rectangles just outside of the linear section. The viewpoint for photography is given as the focal point. To aid in the documentation, a mirror was used to view a different orientation of the plasma. Figure taken from [1].

discharges, limits the total lifetime of the pulse. While this is not surprising, one wonders about the outcome of a mild kink that would result from a carefully controlled current discharge, or the effect of a plasma that is not directly dependent on the current.

Furthermore, the linear devices discussed made no attempt to test any predictions from line tying theory. That the theory had yet to be developed is obviously one obstacle; however, even with a well developed theory, the experiments were too transitory to observe the subtle modifications to external kink stability brought about by line tying. The short pulses found in these experiments also eliminated any opportunity to study the longer RWM. In keeping with the difficultly of accurately measuring stability parameters it should be noted that the experiments were only able to conclude that conducting walls did not offer marked improved stability.

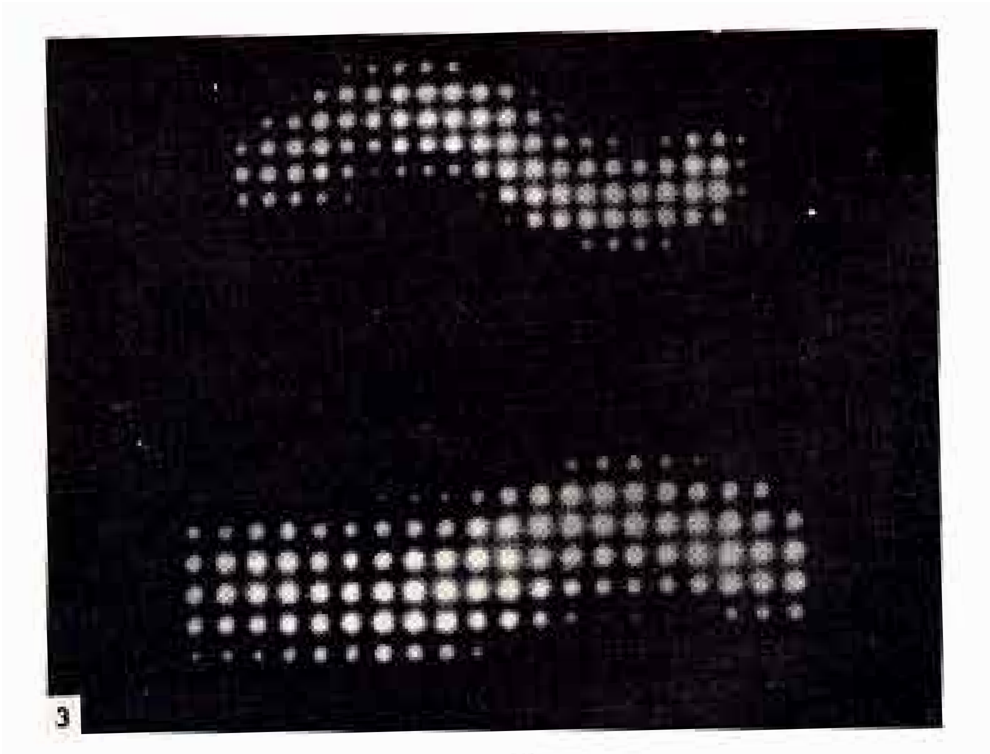

Figure 1.9 Published photo of the kink from the torus described in [1]. Argon gas was used in this discharge. The two images are viewing the same portion of the plasma; however, the upper image is a viewed with the mirror (described in Fig. 1.8 while the lower image is a direct view.) Figure taken from [1].

1.2 Connections to Current Research

The machine which most closely resembles the ReWM is the Reconnection Scaling Experiment (RSX) in Los Alamos [17, 19, 18]. Both machines utilize the same plasma gun to source the plasma and are linear screw pinch devices. While RSX maintains that only one end of their machine is line tied, line tying considerations must still be considered for both machines. Despite these similarities, the machines have different thrusts in their research. The plasma in RSX is too far from the conducting wall to effectively study wall modes. Additionally, the RSX plasma consists of three plasma guns, spaced over 3 cm apart, to source the plasma. The ReWM with its tight gun placement is better able to produce a large plasma close to the wall to study wall modes.

The external kink mode and the RWM limit pressure in tokamaks and the pulse length in RFPs. Tokamaks (DIII-D and HBT-EP), spherical tokamaks (NSTX), and reversed field pinches (Extrap T2R and RFX) all have active RWM research initiatives because stabilization or control can improve the efficiency of the fusion reaction. Without the ability to quell the resistive wall mode, plasma pressure and hence fusion power are limited.

DIII-D has demonstrated RWM stabilization with sufficient plasma rotation [64, 22, 21] and established the importance of minimizing residual field errors [20] which slow rotation and ultimately destabilize the RWM. Recently, the program has sought to determine the minimum rotation necessary for mode stabilization [49]. This latest work focuses on the rotation at a particular point in the plasma and differences in critical rotation rates when slowing the plasma rotation with either torque or magnetic braking.

NSTX also studies the RWM. From the initial identification [55] to the subsequent studies on passive stabilization through rotation [56, 61, 57] NSTX has repeated aspects of the work on DIII-D in a spherical tokamak. NSTX reports that a particular rotation profile across the majority of the plasma, not just at a particular location, is needed to stabilize the RWM [62]. Research has also been undertaken to unify rotational stability parameters in NSTX and DIII-D [50]. These studies also examine the RWM in JET [26]. In addition, NSTX demonstrated control of the RWM with active feedback control on the mode [58].

HBT-EP is another device exploring the dynamics of the RWM. The first studies reported wall stabilization of plasma modes but were unable to conclusively determine if the RWM was in fact present [31]. Subsequent work found the RWM and tested both active feedback stabilization techniques [8, 41] and passive stabilization through plasma rotation [60]. The active feedback techniques are sophisticated enough to produce plasmas close to the ideal wall stability limit [33].

Active feedback has also been applied outside of tokamak devices. Perhaps the most dramatic results so far have come from the Extrap T2R and RFX reversed field pinch experiments, where active feedback stabilization has been used to simultaneously stabilize a spectrum of RWMs, allowing long pulse RFP operation with thin shells [4, 46].

These devices are dedicating substantial time and energy into understanding the details of the RWM and how it can be stabilized. This strong, continuing interest in the RWM serves as motivation for this project. It should be noted that it is far easier to carry out RWM studies on the ReWM than on any of the larger machines mentioned. Beyond the relevance to the fusion community the ReWM is a basic plasma experiment. The ReWM is a line tied plasma and study of the RWM has not previously been reported in this configuration. Furthermore, the small scale of the ReWM allows the program to be more nimble in its objectives. Stabilization of the RWM has focused on rotation or active feedback; however, another option exists which will be discussed in Section 1.3.

1.3 Goals and Thesis Outline

A different solution to the RWM, which does not require active feedback or exotic superconducting materials, is to design a basic magnetic configuration inherently stable to external kinks and RWMs. Gimblett proposes a method for passive stabilization of the RWM in a cylinder [24, 23] with two resistive walls rotating relative to one another. Provided these separate thin walls are close to the plasma boundary with sufficient differential rotation, the RWM can be stabilized. In essence, differential rotation mandates that the RWM cannot lock to both walls simultaneously to access the external free energy. The expression for the magnetic field in the moving wall is governed by the induction equation:

$$\frac{\partial \tilde{\mathbf{B}}}{\partial t} = \nabla \times \left(\mathbf{v} \times \tilde{\mathbf{B}} - \eta \tilde{\mathbf{J}}\right), \tag{1.3}$$

where, η and $\mathbf{v}$ are the resistivity and velocity of the wall, respectively. The introduction of $\mathbf{v}$ is the keystone to the stability. The induced field is now dependent on a controllable parameter, increased rotation yields stronger feedback from the wall. With sufficient rotation the wall mimics a perfectly conducting wall. Testing this hypothesis is one of the main program goals for the ReWM.

Just as the small nature of the ReWM allows it to test passive stabilization through shell rotation, it also opens the possibility to substitute the rigid shell with a liquid metal for RWM stabilization [48, 16, 67]. The ReWM is well suited to carry out the comparison of stabilization properties between a moving rigid conductor and flowing liquid conductor. Demonstrating mode stability with differential rotation of rigid shells is an important question in basic plasma physics. Unfortunately, it is not terribly useful in current fusion devices. While a spinning shell is not feasible in a toroidal geometry, it is at least topologically possible to surround a toroid with a flowing liquid metal. At PPPL study is underway to explore improved plasma performance with lithium as a surface material [32]. Interestingly, this improvement of performance is unrelated to mode stability. Determining mode stabilizing properties of a flowing liquid metal would have far reaching implications for the fusion program.

Separate from exploring future RWM stabilization schemes, the experiments described in Section 1.1 deserve a modern examination. The initial screw pinch experiments never considered line tying modifications to the kink stability. These experiments were also subject to the fundamental limitation that any kink activity would likely disrupt the current column and effectively end the pulse as the plasma would neutralize without ohmic heating. The short pulse in these experiments also precluded study of the RWM with its longer time scale. Initial experiments were under-diagnosed to ascertain if the observable external kinks had any correlation to internal kinks. In terms of fusion research, the experiments in the 1950s were certainly able to conclude that formidable obstacles existed in turning the screw pinch into a fusion reactor. Left by the wayside though were many questions in basic plasma physics.

The initial goal of the ReWM has been to explore the ideal kink and RWM with a fuller set of diagnostics. The ReWM's ability to create a kink instability with decoupled plasma and current sources allows for extended plasma pulses (ms instead of μs) and control over the amount of plasma current. The project also seeks to compare and contrast basic MHD between toroidal systems and line tied systems. A long term machine objective is to test passive stabilization schemes for the RWM. Of course, prior to stabilizing, the RWM itself must be identified. This thesis culminates in identification of the RWM in the ReWM.

Chapter 2 briefly discusses the modifications and extensions to KS theory over the decades. The theoretical model used to analyze the ReWM is presented and attention is paid to the distinction that line tying introduces in developing a dispersion relation. With the dispersion relation, the effect of a perfectly conducting wall's presence or absence upon mode onset and growth can be determined. Of greater utility though is the section presenting predictions for growth of the RWM in the ReWM. These growth estimates serve as a principle benchmark in identifying one mode in Chapter 5 as the RWM.

Chapter 3 describes the ReWM, diagnostics used to measure MHD, as well as the basic order of events in a plasma shot. Prior to work on this Thesis, the ReWM did not exist. The Chapter discusses aspects of building an experiment when starting with an empty room. Initial work focused on the physical needs of the machine itself (vacuum vessel, pumping system, and power supplies). As the machine and power supplies became functional and reliable, the diagnostics and digitizers to take and record data presented herein were built.

Chapter 4 presents the initial data taken on the ReWM. For this chapter, the ReWM has an insulating wall at the boundary which mimics the no wall boundary condition discussed in Chapter 2. Predictions from Chapter 2 are presented and contrasted to the data. The Chapter concludes with basic experiments on mode stability and current profiles as well as a comparison between predicted and measured eigenmodes of B_r.

Chapter 5 presents data on internal and external modes in the ReWM with two different conducting walls present. Primary studies were in conjunction with a boundary that had a wall time of .5 ms. Follow-up experiments utilized a composite wall at the boundary with a wall time of 7 ms. Comparing the data from two walls (with distinct wall times) facilitated identification of the RWM as its growth is dependent on the different wall times.

Finally, Chapter 6 discusses the results from Chapters 4 and 5. Internal modes are seen with and without a conducting boundary. The no wall growth is slower than expected but in keeping with predictions when the evolving status of the current profile is taken into account. The growth of the RWM is well matched to predictions; however, the onset of the mode is unexpected. One question raised in determining mode onset is the measurement of q in the plasma and to what degree is it accurately measured in the ReWM. Finally, data from the ReWM is compared to predictions of a plasma with bulk resistivity, sheath layers at the endplates, and bulk flow. These are all modifications to the theory presented in Chapter 2.

Chapter 2

Theory

The model of the current driven kink has been extended upon substantially since the initial investigation in KS theory. The fundamental interest in the external kink has warranted its coverage in Freidberg's textbook on idea MHD [15]. Freidberg's review itself is drawn from Newcomb [45]. In the 1970s two important modifications to KS theory occurred. At the beginning of the decade Rosenbluth, Dagazian, and Rutherford (RDR) [52] contributed their theory of internal kinks in long cylindrical systems. Throughout the decade astrophysicists identified line tying as a stabilizing factor in linear geometries and coronal loops [47, 13, 29]. Note that the kink in coronal loops is often thought of as an internal kink. From KS to RDR, the theory of the kink evolved from an external to an internal kink. Later, the internal kink stability was modified with line tying. The RDR theory itself was explicitly reexamined with line tying in recent work by Huang [30]. Finally, Hegna and Ryutov applied line tying considerations to the external kink [28, 53].

Thus far resistivity in the plasma has been neglected; however, work at Los Alamos [11, 63, 10] has addressed resistive effects on kink stability. In References [11, 10] internal kinks are explicitly examined in relation to global resistivity and possible tearing modes, while Reference [63] utilizes a nonlinear time-dependent equations of resistive MHD to explore spheromak formation, another environment in which line tied kinks are found. This work adds to and refines the results in References [69, 68, 27, 44] where tearing instabilities are considered in a line tied geometry.

2.1 Line Tying

After the initial linear screw pinch experiments, described in Section 1.1, the fusion community directed experimental and theoretical efforts towards toroidal devices. The solar community's contribution of line tying dynamics modified the stability of the linear screw pinch. Coronal loops and screw pinch laboratory plasmas have essentially the same twisted magnetic configuration. That loops are curved cylinders is obvious but secondary to the magnetic similarity. Coronal loops are also known to transition quickly into an unstable regime which destroys the loop and releases massive amounts of energy. Unlike laboratory screw pinches though, coronal loops are more stable and long lived before instability onset. Hood and Priest not only related the loop instability to the kink common in laboratory plasmas, but also attributed the preceding stability partially to line tying.

The twist in coronal field lines results from footprint motion at the ends of the loop. If the photosphere is slowly rotating in opposite directions at the endpoints, the field lines in the corona will twist. As in the screw pinch, the twist is stable up to a critical value after which relaxation (kinking) occurs. Some of the loop stability and long lifetime is attributed to the slow twisting rate at the footprints; however, line tying constraints also stabilize the loop. Direct experimental observation of the kink process in coronal loops is presented in References [39, 37].

The intersection of field lines with a conducting boundary, known as line tying, stabilizes coronal loops. With the Sun, the dense and highly conducting photosphere itself provides the line tying. In the linear laboratory experiments described in Section 1.1 the anode and cathode (for biasing the plasma) are typically made from copper and provide a line tying boundary condition. Line tying forces shorter wavelength perturbations to vanish at the ends of the cylinder, be it a screw pinch or coronal loop. The effect of line tying is always stabilizing. Analysis undertaken by Hood and Priest demonstrates that a higher critical twist is achieved when a plasma is stabilized with line tying [29].

2.2 Internal Kink Dynamics

Chapter 1 briefly differentiated mode onset and the magnitude of $B_r(r = a)$ when external or internal kinks are considered. The external kink is further examined in Section 2.3 with attention to developing predictions of mode growth and the B_r eigenfunction at the surface of the plasma. Here we only present a brief overview of the internal kink as the bulk of the discussion in Chapter 6 is focused on the external kink.

There are essentially three phases for the internal kink to consider. Initially, the mode undergoes an ideal, linear phase dependent on the actual current profile itself. In this range Huang [30] presents results from an eigenvalue code with line tying taken into consideration. Above a critical current the plasma twists into a helical distortion in either line tied or periodic systems. In periodic systems, RDR non-linear theory predicts the mode has a steep gradient in ξ_r at the rational surface. Interestingly, the fastest growing mode in a line tied system also has a jump in ξ_r at the same location. In a line tied system the gradient in ξ_r is thickened and the growth slowed. Huang's work is an extension of linear RDR theory to a line tied system.

Following the linear growth phase, the non-linear effects dominate the mode dynamics. In Reference [38] a non-linear three dimensional code is utilized to track the evolution of the kink beyond the linear phase. In the various current equilibriums examined, current consolidates in the middle of the machine because $\xi_r = 0$ at the ends. Line tying forces the instability to build at the mid-plane between the endplates. This is in contrast to a periodic system where the stress of the instability is allowed to be distributed along the entire axial direction.

Finally, in order to accommodate computational demands, finite resistivity must be included to follow the mode dynamics. In this final phase the inclusion of resistivity can alter the magnetic topology. Without resistivity, field lines have to maintain some fixed mapping in r and θ from one endplate to another. With resistivity in the plasma the field lines can migrate and terminate at a different location. Chapter 4 identifies a mode with these characteristics.

An alternate consideration of the internal kink is one in which bulk resistively is present in the plasma. This differs from resistive effects localized to the endplates in a line tied system. The latter case is essentially a sheath and considered in Section 6.5.1. This scenario is examined in Reference [11] with a numerical analysis. With resistivity the growth rate of the internal kink is proportional to the amount of resistivity in the plasma. Additionally, the onset criteria for the mode is relaxed and mode growth is seen below the critical current in an ideal plasma.

2.3 Stability of the Line Tied External Kink

The following analysis draws heavily upon Hegna's consideration of a line tied screw pinch in Reference [28]. Only the external kink is examined; however, different boundary conditions at the wall are considered. While this Thesis does not present data on the RWM in conjunction with a spinning rigid conductor, it is one of the program goals for the ReWM and the stability of such a boundary condition will be discussed.

For the plasma modeled, ideal MHD is considered in a cylindrical system in which $\nabla p = 0$, the length is greater than the radius ($l \gg r$), and magnetics such that $B_z \gg B_\theta$. Again, line tying in the system is imposed with perfectly conducting endplates at $z = 0$ and $z = L$. Between the plasma radius, at a, and the first wall, at b, a vacuum exists. For completeness a second wall is considered at c to accommodate not only the final analysis of a spinning shell, but also the experimental condition of one wall with high resistance at b and a second wall with low resistance at c. Data taken with two stationary walls is presented in Chapter 5.

While finite length breaks the periodicity in the axial direction, it is undisturbed in the poloidal direction and a Fourier analysis, where $\tilde{\xi} \sim \xi(r,z)e^{im\theta}$, is appropriate. The ideal MHD magnetic perturbation and displacement vector can be written as

$$\tilde{\mathbf{B}} = \mathbf{B}(r,z)e^{im\theta} \tag{2.1}$$

$$\tilde{\xi} = \xi(r,z)e^{im\theta}, \tag{2.2}$$

where m is the poloidal mode number. While any value of m is valid, only the $m = 1$ mode is considered in the rest of this analysis. The force-free equilibrium is given by

$$\mathbf{B_0} = B_{z0}(r)\hat{\mathbf{z}} + B_{\theta 0}(r)\hat{\theta}, \tag{2.3}$$

and

$$\nabla \times \mathbf{B_0} = \frac{\lambda(r)}{\mu_\mathbf{0}} \mathbf{B_0}, \tag{2.4}$$

where $\lambda(r)$ is the current profile. The linear momentum and induction equations are

$$-\omega^2 \rho_0 \tilde{\xi} = \tilde{\mathbf{J}} \times \mathbf{B_0} + \frac{\lambda}{\mu_\mathbf{0}} \mathbf{B_0} \times \tilde{\mathbf{B}} - \nabla \tilde{\mathbf{p}}, \tag{2.5}$$

$$\tilde{\mathbf{B}} = \nabla \times \left(\tilde{\xi} \times \mathbf{B_0} \right). \tag{2.6}$$

By assuming that the plasma is incompressible ($\nabla \cdot \tilde{\xi} = 0$), the radial component of Equation 2.5 reduces to

$$\omega^2 \nabla_\perp \cdot [\mu_0 \rho_0 \nabla_\perp (r \tilde{\xi}_r] = -\mathbf{B_0} \cdot \nabla [\nabla_\perp{}^\mathbf{2} (r \tilde{B}_r)] + \frac{i B_0}{r} \frac{d\lambda}{dr} (r \tilde{B}_r), \tag{2.7}$$

where

$$\nabla_\perp{}^2 = \frac{1}{r} \frac{\partial}{\partial r} \left(r \frac{\partial}{\partial r} \right) + \frac{1}{r^2} \frac{\partial^2}{\partial \theta^2}. \tag{2.8}$$

A significant simplification to Equation 2.7 can by made by constructing an idealized flat current profile with the Heaviside step function $\Theta(x)$. Specifically the current profile is represented as

$$\lambda(r) = \lambda_0 \Theta(a - r). \tag{2.9}$$

While this restriction to the current profile limits the applicability of this model to the plasma, the insight gained provides a starting point to understanding the plasma in the ReWM. Realizing that $\rho = \lambda = 0$ when $r = a+$, one can integrate Equation 2.7 with respect to r to obtain

$$\omega^2 \mu_0 \rho_0 \tilde{\xi}_a \Delta_\xi = (\mathbf{B_0} \cdot \nabla) \tilde{B}_a (\mathbf{\Delta}_+ - \mathbf{\Delta}_-) + i B_0 \lambda_0 \tilde{B}_a, \tag{2.10}$$

with $\tilde{B}_a = \tilde{B}_r(r = a)$, $\tilde{\xi}_a = \tilde{\xi}_r(r = a)$, and

$$\Delta_\xi = \frac{1}{\tilde{\xi}_a} \left. \frac{d(r\tilde{\xi})}{dr} \right|_{r=a-}, \tag{2.11}$$

$$\Delta_- = \frac{1}{\tilde{B}_a} \left. \frac{d(r\tilde{B}_r)}{dr} \right|_{r=a-}, \tag{2.12}$$

$$\Delta_+ = \frac{1}{\tilde{B}_a} \left. \frac{d(r\tilde{B}_r)}{dr} \right|_{r=a+}. \tag{2.13}$$

Finally, with the linear induction equation, $\tilde{B}_a = (\mathbf{B_0} \cdot \nabla)\tilde{\xi_a}$, and current profile given in Equation 2.9, the eigenmode equation must satisfy

$$\left[\frac{1}{r}\frac{d}{dr}\left(r\frac{d}{dr}\right) - \frac{1}{r^2}\right][\omega^2\mu_0\rho_0 r\tilde{\xi}_r + (\mathbf{B_0} \cdot \nabla) r\tilde{B}_r] = \mathbf{0}. \tag{2.14}$$

Enforcing the regularity of the eigenmode along the machine axis, $\omega^2\mu_0\rho_0 r\tilde{\xi}_r + (\mathbf{B_0} \cdot \nabla) r\tilde{B}_r \sim r$, Equation 2.10 reduces to

$$\omega^2\rho_0\mu_0\tilde{\xi}_a = (\mathbf{B_0} \cdot \nabla)\tilde{B}_a(\Delta_+ - 1) + iB_0\lambda_0\tilde{B}_a. \tag{2.15}$$

Equation 2.15 and the linear induction equation from above can be coupled together to express the displacement at the plasma boundary as

$$\omega^2\rho_0\mu_0\tilde{\xi}_a = (\mathbf{B_0} \cdot \nabla)^2\tilde{\xi}_a(\Delta_+ - 1) + iB\lambda_0(\mathbf{B_0} \cdot \nabla)\tilde{\xi}_a, \tag{2.16}$$

Moreover, $\tilde{\xi}_a = \xi(z)e^{i\theta}$ can be applied to Equation 2.16 to construct a second-order differential equation for $\xi(z)$ expressed below

$$\omega^2\frac{\rho_0\mu_0}{B_{z0}^2}\xi = \left(\frac{d^2\xi}{dz^2} + 2i\frac{B_{\theta a}}{aB_{z0}}\frac{d\xi}{dz} - \frac{B_{\theta a}^2}{a^2B_{z0}^2}\xi\right)(\Delta_+ - 1) + \lambda_0\left(i\frac{d\xi}{dz} - \frac{B_{\theta a}}{aB_{z0}}\xi\right) = 0. \tag{2.17}$$

In Equation 2.17 $B_{\theta a} = B_{\theta 0}(r = a)$. By assuming a solution of the form $\sim e^{ikz}$ two roots for k can be found.

$$k_{1,2} = -\frac{B_{\theta a}}{aB_{z0}} + \frac{\lambda_0}{2(1-\Delta_+)} \pm \sqrt{\frac{\lambda_0^2}{4(1-\Delta_+)^2} + \frac{\omega^2}{\nu_A^2(1-\Delta_+)}}, \tag{2.18}$$

where $\nu_A^2 = B_{z0}^2/\mu_0\rho_0$. Thus far no restrictions have been placed upon the eigenmode and the solutions of the form $e^{ik_1z} + e^{ik_2z}$ are generally valid; however, the plasma in the ReWM has line tying constraints that are applicable to the solutions found. Specifically, line tying mandates that $\tilde{\xi}_r(z = 0) = \tilde{\xi}_r(z = L) = 0$. This restraint can simply be satisfied with the quantization condition

$$k_1 - k_2 = \frac{2n\pi}{L} \tag{2.19}$$

In Equation 2.19 n is simply an integer. With the above constraints $\xi(r)$ takes the form

$$\tilde{\xi}_r(r,\theta,z) = f(r)e^{i\theta + i(k_1+k_2)z/2}\sin\left(\frac{n\pi z}{L}\right). \tag{2.20}$$

Coupling Equation 2.20 into Equation 2.17 allows one to produce an eigenvalue equation for the growth rate

$$\frac{2n\pi}{L} = \sqrt{\frac{{\lambda_0}^2}{(1-\Delta_+)^2} + \frac{4\omega^2}{{\upsilon_A}^2(1-\Delta_+)}}, \tag{2.21}$$

Thus far the structure of ξ and growth of the mode have only been expressed generally in terms of Δ_+. The term is straightforward and easily defined in Equation 2.13; however, the expression does not convey the physics captured in Δ_+. Quite simply, Δ_+ provides for continuity in $B_r(r)$ as $r = 0 \rightarrow \infty$ at $B_r(r = a)$. By ensuring this continuity at the plasma boundary the MHD inside and outside the plasma are joined. Thus, ξ and the growth rate are dependent upon both the plasma parameters and the electro-magnetic properties outside the plasma. Again, just to restate the fact, this is only true with external kinks. Internal kinks dynamics are not modified by the physical environment outside the plasma.

In a plasma as described above without any walls at $r = b, c$, $\Delta_+ = -1$ (details given in Section 2.4). For the no wall plasma, $\tilde{\xi}$ is given below.

$$\tilde{\xi}_r(r,\theta,z) = f(r)e^{im\theta + in(\frac{2\pi}{Lq_a} + \frac{\lambda_0}{4})z} \sin\left(\frac{n\pi z}{L}\right) \tag{2.22}$$

Appendix B contains additional details and discussions about the no wall eigenfunctions of both $\xi_r(z)$ and $B_r(z,\theta)$ and how they differ from a periodic system.

In the line tied geometry at least two counter propagating modes are required to satisfy the boundary conditions. The most unstable modes are those with the lowest mode numbers, namely $m = 1$ and $n = 1$. In line tied plasmas, higher order modes ($m > 1$) are almost completely stable. The stability criteria for the ideal $m = 1$ kink and corresponding RWM in the line tied screw pinch are only slightly modified; however, with particular current profiles and wall locations, line tying does offer additional stability [53]. In experimental plasmas, the extra stability is more the exception than the rule. The KS prediction for mode onset is generally still valid and points to the robustness of the $m = 1$ external kink in solar and laboratory plasmas.

2.4 Effects of Ideal and Resistive Boundary Conditions

The problem of determining growth and onset of the external kink when there are walls beyond the plasma is more related to basic electricity and magnetism than full MHD theory. Principle mode dynamics are determined by MHD stability; however, this stability model must be self consistent in the presence of a wall or walls outside the plasma. As will be shown in this section, the quantity Δ_+ matches the environment outside and inside the plasma.

Provided that the plasma is constrained within $r = a$, the space beyond $r = a$ is a vacuum region where MHD relations can be simplified significantly. In the vacuum region the magnetic field can be expressed as $\mathbf{B} = \nabla\tilde{\phi}$ where $\tilde{\phi} = e^{i\theta}\phi$. This in turn implies that $\nabla^2\tilde{\phi} = 0$. With the geometric assumptions made previously, $L \gg r$, ϕ can simply be expressed as linear combinations of r and $1/r$ with coefficients that are related by the boundary conditions at the walls and infinity. Thus an expression for B_r is built for each section, be it within the plasma ($r < a$), between the plasma and first wall ($a < r < b$), between the two walls ($b < r < c$), or from the second wall to infinity ($c < r < \infty$). Continuity of B_r is ensured by matching the functions for B_r at each section interface. To ease this process a bit, the walls are assumed to be thinner than the electromagnetic skin depth. This is referred to as the thin wall assumption.

In order to determine how B_r behaves within each wall the linear induction equation, given below, must be used.

$$\frac{\partial \tilde{B}_r}{\partial t} + \mathbf{V} \cdot \nabla \tilde{B}_r = \frac{\eta_i}{\mu_0}\frac{1}{r}\nabla^2(r\tilde{B}_r) \tag{2.23}$$

where $\mathbf{V}$ is velocity and η_i represents the resistivity of the individual walls. The eddy current flowing in the wall is a response to the radial magnetic field outside the wall. The dependence between the two can be found by integrating across the wall. For the stationary wall at b that relationship is

$$\gamma\tau_b\tilde{B}_r \mid_{r=b} = b\, \frac{d\tilde{B}_r}{dr}\Bigg|_{r=b-}^{r=b+}. \tag{2.24}$$

For a rotating wall at c the equivalent expression is

$$\left(\gamma + i\frac{V_c}{c}\right)\tau_c\tilde{B}_r \mid_{r=c} = c\, \frac{d\tilde{B}_r}{dr}\Bigg|_{r=c-}^{r=c+}. \tag{2.25}$$

In both expressions $\tau_{b,c}$ is the wall time for the appropriate wall. For the first wall, $\tau_b = \mu_0 b\delta_b/\eta_b$, where δ_b is the thickness of the wall and η the resistivity. Similarly, for the second wall $\tau_c = \mu_0 c\delta_c/\eta_c$. As a matter for later ease in bookkeeping the following quantities are defined.

$$\Delta_b = \frac{\gamma\tau_b}{2}, \tag{2.26}$$

$$\Delta_c = \frac{\gamma\tau_c}{2} + i\frac{R_c}{2}, \tag{2.27}$$

where $R_c = V_c\tau_c/c$ is the Reynolds number for the rotating wall. Of course the second wall at c can be stationary in this analysis. Under such circumstances $V_c = 0$ and Δ_c reduces to conventional form.

The objective in modeling the ReWM is to determine an expression for Δ_+ which encompasses all the relevant boundary conditions with proper matching across interfaces. Equations 2.24 and 2.25 provide matching constraints at the walls. Thus, determining a proper expression for Δ_+ is now algebraic and given by

$$\Delta_+ = \frac{-1 - \Delta_b\left[1+\left(\frac{a}{b}\right)^2\right] - \Delta_c\left[1+\left(\frac{a}{c}\right)^2\right] - \Delta_b\Delta_c\left[1+\left(\frac{a}{b}\right)^2\right]\left[1-\left(\frac{b}{c}\right)^2\right]}{1 + \Delta_b\left[1-\left(\frac{a}{b}\right)^2\right] + \Delta_c\left[1-\left(\frac{a}{c}\right)^2\right] + \Delta_b\Delta_c\left[1-\left(\frac{a}{b}\right)^2\right]\left[1-\left(\frac{b}{c}\right)^2\right]} \tag{2.28}$$

While not immediately obvious, Equation 2.28 is simple to manipulate into various limits. Without any walls present, $\Delta_{b,c} = 0$ and $\Delta_+ = -1$. For a perfectly conducting wall at b, $\Delta_b \to \infty$ and the wall at c can be ignored. With an ideal wall at b, Equation 2.28, Δ_+ reduces to the following

$$\Delta_+ = 1 - \frac{2}{1-\left(\frac{a}{b}\right)^2}. \tag{2.29}$$

In order to calculate the growth rate of the external kink in the presence of boundary conditions that are resistive, the dispersion relation in Equation 2.21 should be modified to account for the slow time scale associated with flux leaking through the wall. Because wall times are so much longer than Alfvénic times, the kinetic energy of the mode may be ignored. With this assumption ($\omega^2 = 0$ and $n = 1$), Equation 2.21 reduces to

$$1 - \Delta_+ = \frac{2}{q_a}. \tag{2.30}$$

To determine the mode growth when a resistive wall is present Δ_+ is determined from Equation 2.28 and substituted into Equation 2.30. With only a single resistive wall at b, Equation 2.28 simplifies to

$$\Delta_+ = \frac{-1 - \Delta_b\left[1 + \left(\frac{a}{b}\right)^2\right]}{1 + \Delta_b\left[1 - \left(\frac{a}{b}\right)^2\right]} \tag{2.31}$$

Combining Equations 2.30 and 2.31 yields the growth for the RWM in terms of Δ_b. The final expression for γ is in Section 2.6.

The dispersion equation (Equation 2.21) and comprehensive expression for the jump condition (Equation 2.28) determine the dynamics of the ideal external kink. Specificity of the growth only requires the appropriate limits to be taken with both equations. The interaction between the boundary condition and growth rate of the external kink will be explored in the following sections.

2.5 External Kink Growth and Onset With and Without an Ideal Wall

In order to establish an understanding of the external kink it is useful to consider the presence or absence of an ideal, or perfectly conducting, wall. Without resistance, the eddy currents in an ideal wall that stabilize the external kink never resistively decay away. The basic result is an increase in stability for the external kink and ability to pass more current through a plasma before mode onset.

In Section 2.4 it was shown that the jump condition, Δ_+, for a plasma with no wall at the boundary is equal to -1. In order to determine the growth of the external kink, Equation 2.21 must be utilized in conjunction with the expression for Δ_+. Following a slight reshuffling of terms, the dispersion relation is equal to

$$\omega^2\tau_A^2 = \frac{1}{2}\left(1 - \frac{1}{q_a^2}\right) \tag{2.32}$$

where $\tau_A = L/2\pi v_A$. When $q_a < 1$ the mode is unstable and growing. Thus, the line tied external kink without a wall is unstable when

$$q_a < 1. \tag{2.33}$$

As stated previously, this is the same stability condition found in KS theory. This characterization of the no wall kink is the appropriate model for analyzing the plasmas with a Pyrex wall in Chapter 4 as this boundary cannot produce any stabilizing eddy currents.

For the sake of completion, attention is turned to the presence of a perfectly conducting wall located at radius b in relation to the plasma radius at a. As in the no wall example, an expression for Δ_+ must be found before considering mode growth or onset. From Section 2.4, $\Delta_+ = 1 - 2/(1-(a/b)^2)$. Using this expression for Δ_+ with Equation 2.21, the dispersion relation for the external kink in the presence of a perfectly conducting wall is

$$\omega^2\tau_A^2 = \frac{1}{2\left[1-\left(\frac{a}{b}\right)^2\right]}\left[1-\frac{\left[1-\left(\frac{a}{b}\right)^2\right]^2}{q_a^2}\right]. \tag{2.34}$$

Inspection of Equation 2.34 indicates that the mode is unstable when $q_a < 1-(a/b)^2$. Thus a window of stability exists where the external kink is stabilized with an ideal wall. Mode onset is governed by the location of the wall, at b, in relation to the outer radius of the plasma, at a. As the wall is located closer to the plasma, the kink is increasingly stabilized.

The onset and growth of the external kink with and without a perfectly conducting wall at the boundary is plotted in Fig. 2.1. Note that the growth rates have been reduced by a factor of 1000. Without any wall, the kink begins to grow when $q_a < 1$. The ideal wall reduces q_{onset} from 1, to a value below 1. Once unstable, the kink grows very fast in either limit.

2.6 Growth and Onset of the RWM

Section 2.5 considered the stability threshold and growth for an external kink in a plasma with and without a perfectly conducting wall. So long as there are eddy currents in the wall the external kink can be stabilized beyond the no wall limit. However, a conventional wall has finite resistivity which allows the eddy currents to decay away. Between the perfect wall and no wall limiting cases exists a band where the plasma is stable with a perfectly conducting shell but unstable without a shell. This band

$$1-\left(\frac{a}{b}\right)^2 < q_a < 1 \tag{2.35}$$

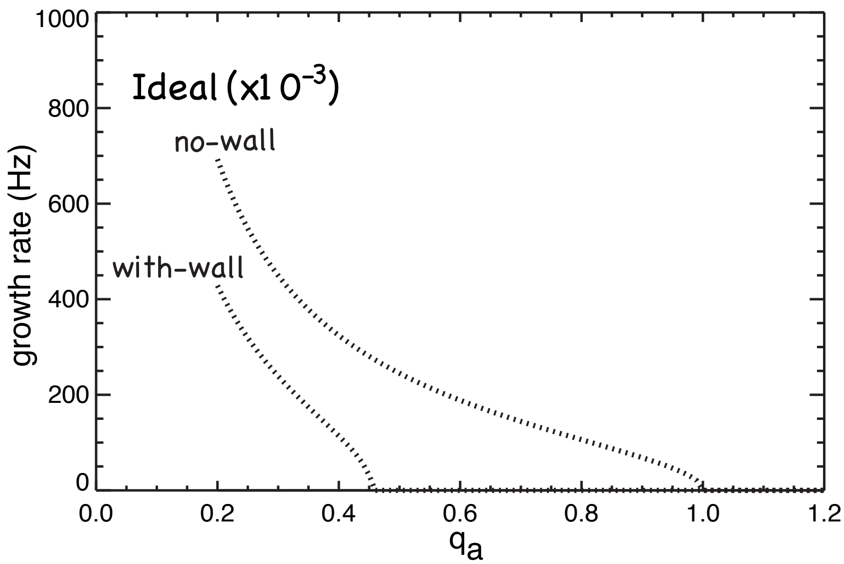

Figure 2.1 Growth rates for the ideal external kink in a line tied pinch with and without a perfectly conducting wall present. For the plot, the plasma radius a = 7.5 cm and the perfect wall radius is at $b = 10$ cm. With an ideal wall a window of stability is present when $.45 < q < 1$. Note that the ideal modes grow approximately 1000 times more quickly.

is the region of the RWM. Finite wall resistance allows the kink mode to grow on the much slower wall time rather than the fast Alfvènic. For a plasma with uniform current density and well defined radius a surrounded by vacuum, the growth rate of the RWM is

$$\gamma = \frac{2}{\tau_w}\frac{1-q_a}{q_a - \left(1-\left(\frac{a}{b}\right)^2\right)}. \tag{2.36}$$

To obtain Equation 2.36 one needs only to couple Equation 2.30 and Equation 2.31 from Section 2.4 together and solve for γ in Δ_b. The essence of the RWM in a cylindrical line tied screw pinch is captured in Fig. 2.2 where the onset and growth rate for the RWM have been added to the with wall (perfect wall) and no wall growth rates from Fig. 2.1. While RWM onset is identical to the no wall external kink, it growth is a fraction of the no wall kink.

Some of the experiments performed in Chapter 5 use only one resistive wall at the boundary. For these experiments, Equation 2.36 is sufficient to determine the degree to which the measured and predicted growth rates match. However, a different set of experiments utilize two walls at the

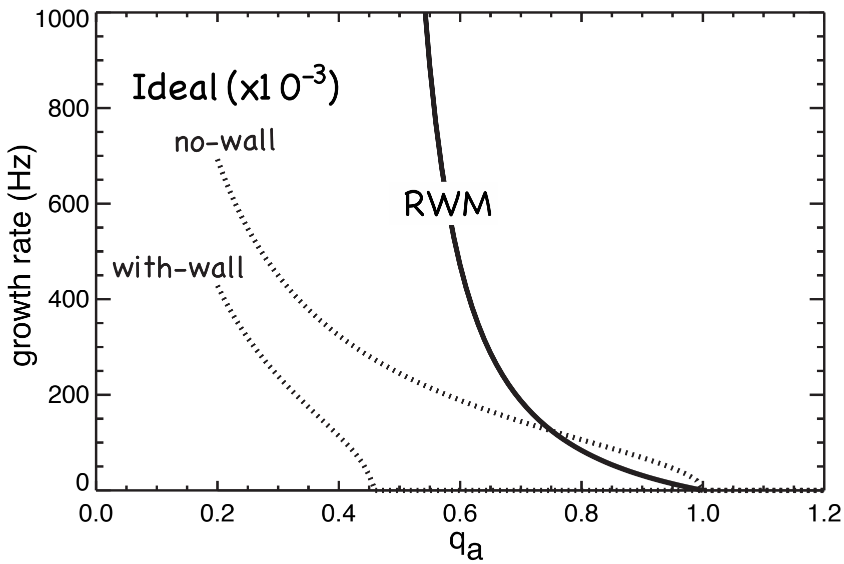

Figure 2.2 Growth rates predicted for ideal modes and the RWM in a line tied pinch. The plasma radius a = 7.5 cm, the stationary wall radius $b = 10$ cm. The wall time $\tau_b \approx 10$ ms. With a conducting wall, mode onset is identical to the no wall kink onset. Note that the ideal modes grow approximately 1000 times more quickly.

boundary with different wall times. The growth predicted from Equation 2.36 is incomplete for this condition. To account for independent walls and wall times, one must use the full expression for the jump condition given in Equation 2.28 in association with the modified dispersion relation in Equation 2.30. Performing these steps and solving for the common growth rate, γ, in both walls yields

$$\gamma = -\frac{1}{\epsilon}\left[\frac{1}{\tau_c} + \frac{X_c}{\tau_b X_b}\right] \pm \frac{1}{\epsilon}\sqrt{\left[\frac{1}{\tau_c} + \frac{X_c}{\tau_b X_b}\right]^2 - \frac{4X_\infty \epsilon}{X_b \tau_b \tau_c}}, \tag{2.37}$$

where $\tau_{b,c}$ refers to the wall time of the respective walls, ϵ indicates one wall location in relation to the other, and $X_{b,c,\infty}$ indicates the strength of the ideal MHD drive for a no wall, perfect wall at b, and perfect wall at c configuration, respectively, and are given below.

$$\epsilon = 1 - \left(\frac{b}{c}\right)^2 \tag{2.38}$$

$$X_b = 1 - \frac{1 - \left(\frac{a}{b}\right)^2}{q_a} \tag{2.39}$$

$$X_c = 1 - \frac{1 - \left(\frac{a}{c}\right)^2}{q_a} \tag{2.40}$$

$$X_\infty = 1 - \frac{1}{q_a} \tag{2.41}$$

Just as the growth rate for two stationary walls can be solved for, the generalized case with a secondary spinning shell can be analyzed. Without presenting the details of such a calculation it is noted that with a sufficient rotation rate, the boundary condition of two shells with differential rotation can stabilize the external kink to a degree dependent on rotation. As with an ideal wall close to the plasma boundary, a window of stability opens below $q_a = 1$. Actual mode onset is determined by the rotation rate in the second shell.

2.7 Linear and Toroidal Geometries

Toroidal geometries like the tokamak are known to be unstable to external kinks beyond the $m = 1$ mode. In fact, modes with corresponding m and n are unstable when the value of q_a is just below any rational value. The operator of the machine has a significant challenge because the current ramp up will necessary push q_a through a series of mode rational surfaces. An important advantage of line tied systems is that many modes other than the $m = 1$ external kink are stable. Ryutov shows explicitly that the stability of higher order modes is modified with line tying constraints in Reference [53]. Modes with $m > 1$ are completely stable with a hollow current profile; however, the stability lessens as the inner region of the current profile fills in.

Chapter 3

Experimental Apparatus

A new line tied cylindrical device has been constructed to study current driven kinks. The plasma length is approximately 1.2 m and the diameter can be adjusted from 6 to 20 cm. Four solenoidal magnets produce fields up to 500 G. The solenoids can be powered to produce a uniform or mirror axial field along the machine axis. 19 electrostatic guns produce the plasma and a separate external supply biases the plasma. After initial powering, the machine is fully operable from a remote setting. Flux loops are positioned to monitor B_r outside the vacuum vessel, and B_z and B_θ just inside the vacuum vessel. A segmented anode allows for q to be calculated at three different points in the plasma. Diagnostics, digitizers, and supporting hardware and software were developed to sample and record 5 Mbytes per shot.

3.1 Vacuum Vessel

The ReWM is a line tied cylindrical screw pinch. Figures 3.1 and 3.2 are a mechanical drawing and actual photograph of the ReWM, respectively. From the beginning the ReWM has been designed to be adaptable to different experimental conditions. The plasma length is $\approx$ 1.2 m long with a radius that can be adjusted between 3 and 10 cm. The current and density can be varied at the plasma source to produce hollow or peaked profiles. The vessel wall itself is removable and allows for experimentation with different boundary conditions at the wall.

The ReWM is able to examine plasma MHD with different wall materials, and slight differences in diameter, while not effecting the vacuum quality. This is achieved with neoprene bladders. The bladders, located at the junction of the shell and end chamber, are connected to an independent pressurized air supply, see Figure 3.1. As the bladders inflate, they automatically center the shell and because they provide a dynamic seal, they are far more flexible than typical vacuum seals. This flexibility allows for experiments with an insulating wall, $r = 3.74$ in, or a stainless steel wall $r = 3.87$ in. Accommodating an eighth of an inch difference in radius with a copper or o-ring seal would be impossible. The neoprene seals also accommodate the slight ovalness inherent to the shells when they are machined by the rolling and annealing process. The flexibility of the seal does not adversely effect the vacuum quality.

The base pressure for the ReWM is about 1×10^{-7} torr. A turbo molecular pump in conjunction with a roughing pump are sufficient to maintain the base pressure. When probes are placed on the machine for diagnostic purposes, they are typically pumped with another roughing pump so as to minimize the differential pressure at the vacuum interface and not raise the base pressure in the vessel. With a turbo and multiple roughing pumps, some centralized control and interlock system is required for ease of operation and safety. Such an interlock and control scheme has been built for the lab.

At the core of the vacuum system is the turbo molecular pump. The turbo pump is the single most expensive and fragile item in the vacuum system. Fortunately, turbo pumps have a well defined and avoidable failure path: sudden exposure to high pressure. Shortly after the pump was tested for basic functionality, an interlock system was designed and built to protect the pump. The interlock monitors pressure in the machine, turbo pump, and bladders. Should the machine or turbo pressure abruptly rise or the line pressure to the bladders fail, the turbo is partially shut down and put into a safe mode.

The ReWM is a linear device without the typical pre-fill of gas. Most of the machines from Section 1.1 had gas present in the chamber before producing a plasma current. The plasma production source, described in Section 3.3, streams gas into the machine prior to producing a plasma or bias. To prevent the build up of gas in the machine, the end chambers are designed to have a large volume to accept gas expansion. These expansion chambers can be seen in Figure 3.1 at the anode and cathode.

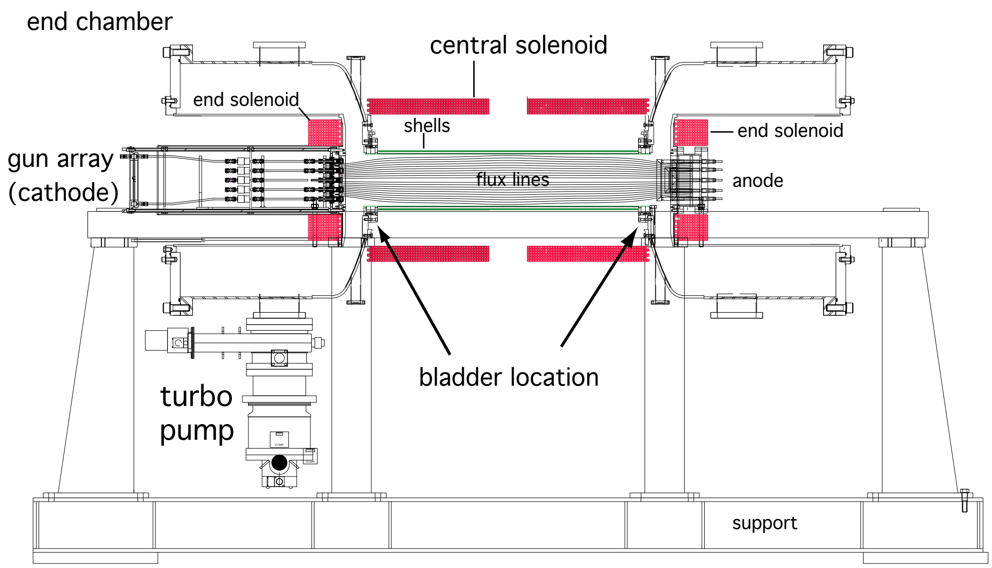

Figure 3.1 A cut away schematic view from the side of the ReWM. The magnets are in red. The ReWM has hollow end chambers designed to mitigate gas build up as the guns are discharged.

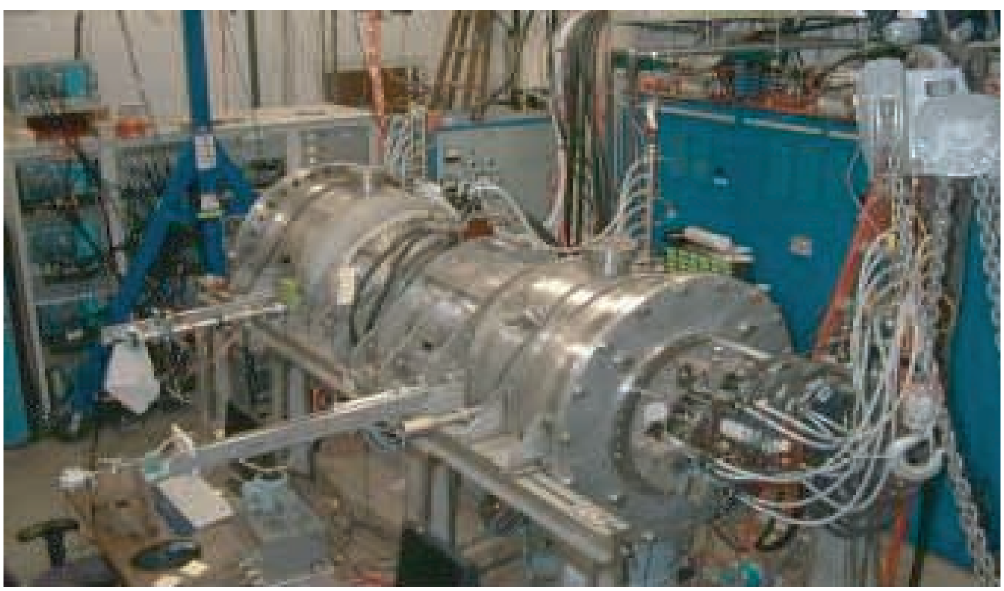

Figure 3.2 A picture of the ReWM. Attached probes are seen on the right side of the picture. In the foreground, the water cooling and electrical leads can be seen. Towards the right some of the capacitor banks for the bias are visible, while in the background left CAMAC crates for digitizers are seen. In the center background is one of the power supplies for the axial solenoids.

3.2 Magnetic Field

The axial magnetic field is produced with four solenoidal magnets shown in Figure 3.1. The central and end solenoids can be run independently to produce either uniform, pinched, or flared magnetic fields. The axial field for the plasmas described in this Thesis were between 250 and 500 G with mirror ratio $.95 < R_m < 1.2$, where $R_m \equiv B_{L=0m}/B_{L=.6m}$. This range of R_m is the maximum achievable with the existing power supplies and cooling system.

For several years, the laboratory had only one power supply which itself required restoration before it could be turned on. Formerly, the power supply was a 480 V three phase DC supply with an analog timing circuit to fire the SCRs. While the DC and AC side of the circuit were in decent order, the timing circuit and water cooling system required a complete overhaul. The analog control was replaced with a digital control device built by third party vendors. The new digital control could be interfaced with an external connection for remote operation. The rehabilitated power supply could be electrically connected to the four solenoids in series to produce fields up to 500 G. With the remote control portion added into the circuit all adjustments could be made quickly from the control room without having to venture into the laboratory.

After some time, a second supply became available. Following its commission, it powered the two end solenoids in series. The power supplies were divided between either the central or end solenoids so as to maintain magnetic symmetry when operating the machine. In this fashion power supply A would carry one current load while power supply B may match it or not. Naturally, if the supplies were matched, the magnetic environment was identical to one power supply connected to all solenoids in series. However, different current loads in the supplies allowed for experiments in which the mirror ratio was adjusted.

3.3 Plasma Source

The plasma source is composed of 19 electrostatic guns [14] packed in a hexagonal array. Figure 3.3 is a schematic view looking directly at the nozzles of the guns. An individual gun is shown in Fig. 3.4. The gun is a ring stabilized arc discharge able to produce up to 1 kA at $\approx$ 150

V with a low level of impurities. The size and temperature of the plasma and current profile from a gun has been measured to have a Gaussian profile with a half maximum radius of approximately 2 cm and a temperature of $\approx$ 2 eV, see Fig. 3.5. The gun power supply is a pulse forming network (PFN) tuned to deliver a 10 ms pulse. The amount of current discharged (and plasma produced) in each pulse is adjustable. Power supplies can be wired in series to obtain multiples of 10 ms discharges; thus, three PFNs in series with one gun will produce a 30 ms pulse of adjustable amplitude. Each gun can also support an external bias to act as a cathode. With an applied bias the plasma becomes a current carrying plasma.

The plasma guns are held in place by the cathode array, a photo of which is shown in Fig. 3.6. The cathode array physically supports the guns, electrical leads, and fueling for the 19 guns. The guns are typically fueled with either hydrogen or deuterium. Plasmas with noble gases have been demonstrated in the past. A solenoidal puff valve controls the gas flow to each gun. The valve is powered by a high voltage pulse adjustable in length. Gun-to-gun spacing in the cathode array is 3.5 cm which provides a current source (the array in its entirety) which varies by less than %25. There is expected to be an additional merging of the current filaments, such as that observed in References [17] and simulated in [65] to smooth out the azimuthal variation of the current profile.

3.4 Plasma Current

A significant amount of development for the ReWM has gone towards the ability to produce and control current in the plasma. One way this machine differs from those discussed in Section 1.1 is that it has one circuit responsible for producing the plasmas (the PFN power supply) and a second independent circuit to bias the plasma and produce a current. Any kink or RWM resulting from current drive is decoupled from the actual plasma source. Chiefly this allows for the observation of dynamics past the onset of the kink. Fundamental to the ReWM is the bias system which allows for the study of current driven instabilities.

The bias circuit can be run in two distinct ways: voltage or current control. The current control method is much more complicated and detailed in Appendix A. Voltage control of the bias system is straightforward. Shortly after the plasma gun has begun its discharge, a second switch in series

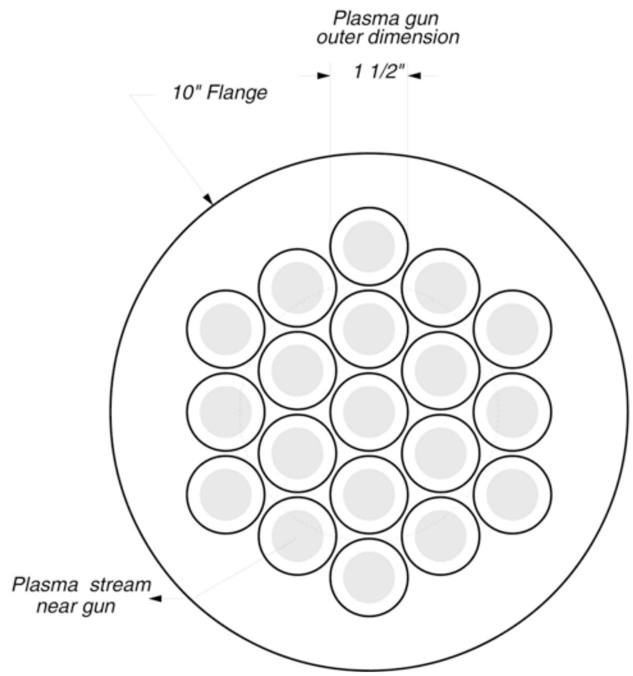

Figure 3.3 A facing view of the gun nozzles at the cathode. The solid gray circles represent the tube diameter which discharges the plasma and the black circles are the outer circumference of each gun.

Figure 3.4 A single gun. The gun nozzle is on the left. In the middle is a nylon fitting to serve as an electrical break between the gun and gas line. At the right is the solenoid valve to control gas flow to the arc region. The solenoid is pulsed by a high voltage signal sent through a co-ax cable.

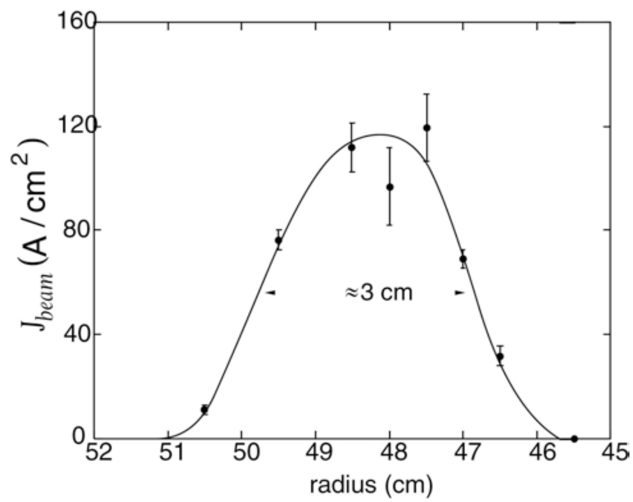

Figure 3.5 Radial profile of the emission current measured with a movable Rogowski coil. The arc and bias are each 1000 A. Figure from [14]

with a bias capacitor closes for several ms. As long as the gun produces a plasma and the capacitor sustains a modest voltage (80 V) across the anode and cathode, a plasma current will be sustained. There are three drawbacks to this approach. First, the experimenter has control only over the voltage across the plasma column, not the amount of current actually carried in the plasma. Second, the plasma current is slave to the inherent RC droop found when a capacitor powers a current. The plasma shot will end with less net current. Third, voltage control incorrectly assumes a constant impedance in the plasma throughout the discharge. Despite these objections, initial experiments were carried out with a voltage control scheme. The enumerated concerns are muted in the no wall experiments because the time scale of the instability is far faster than the shot lifetime. Essentially, the expected dynamics are fast enough that details associated with the end of the pulse are secondary to the initial pulse conditions.

The alternative to voltage control of the bias system is current control. The interested reader is strongly encouraged to read Appendix A for a detailed description of this system's inner workings. While current control is a complicated and difficult control scheme, the advantage is plotted in Figure 3.7. Here, seven separate current control circuits are working concurrently to produce the plasma current.

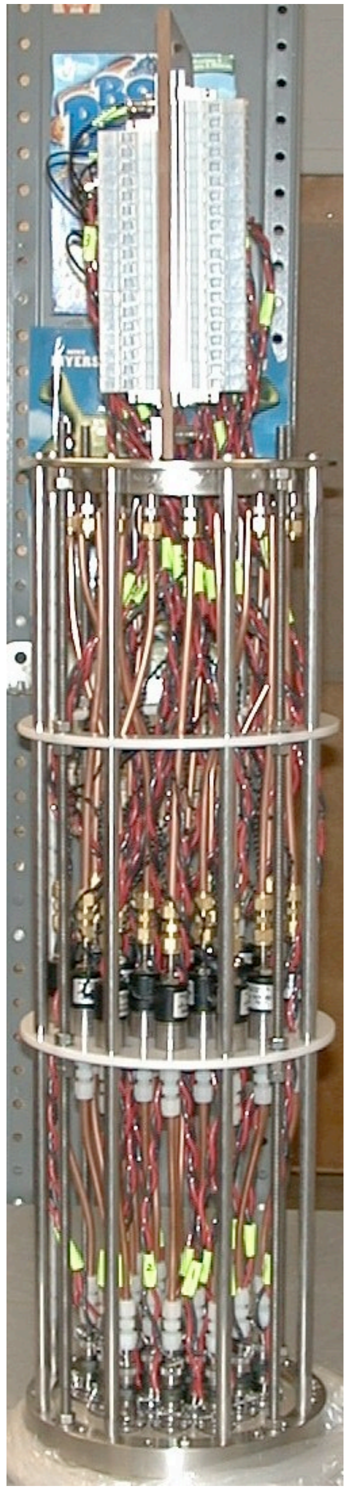

Figure 3.6 The assembled cathode array. At the top are the electrical junctions for the arc leads. The black cylinders towards the middle are the solenoid valves. Within the support structure the gas and arc lines are seen. The gun nozzles are at the bottom of the photo and not visible from this perspective. The cathode array as a whole serves to stabilize and hold gas lines, puff valves, and electrical leads.

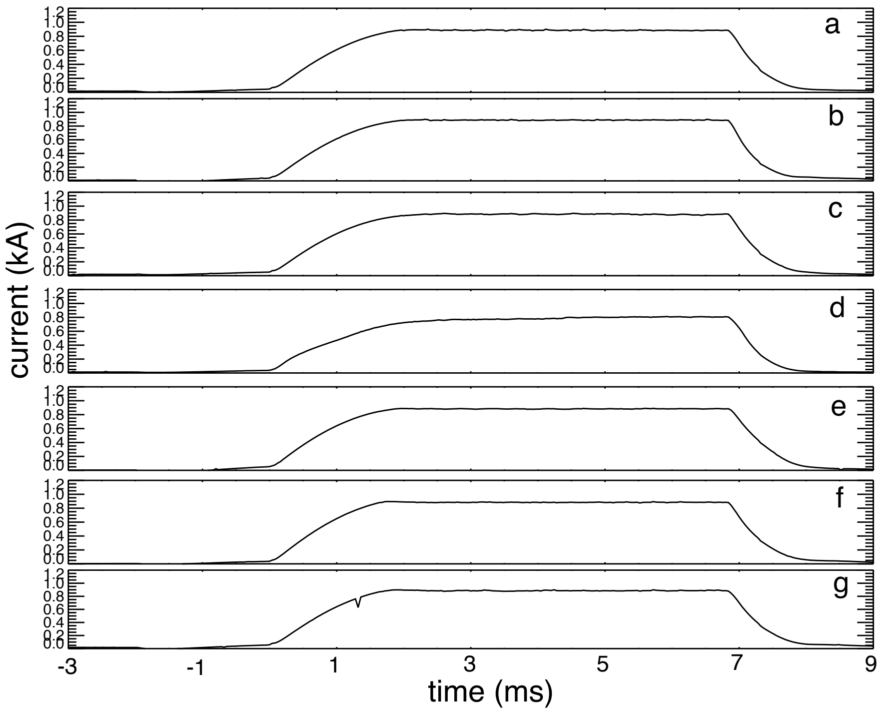

Figure 3.7 The seven current profiles for circuits a-g when matching a DC voltage signal corresponding to 875 amps. The smooth flattop and adjustable net amplitude is necessary for repeatable current drive in the plasma. This shot is executed with a 7 ms pulse but extending the pulse to 20 ms is trivial.

The Pulse Width Modulation (PWM) system allows for flat top current profiles with a single robust switch and three modest sized capacitor banks. For RWM studies in the ReWM, the net current could not vary on the time scale of the wall time as this would limit the ability to differentiate the physics of the external kink and current drive.

3.5 Machine Control

Machine control is through National Instruments Corporation's FieldPoint input/output modules and software. FieldPoint and its supporting software allows the experimenter to remotely control relays and interact with digital or analog input and output modules.

In the ReWM laboratory, FieldPoint operates the DC power supplies for the magnets and controls aspects of the bias system. For the DC supplies, FieldPoint turns the power supplies on, controls necessary liquid cooling, and determines the current in the solenoids. FieldPoint is also interfaced with the DC supplies to act as a composite software and hardware interface. In this fashion, if a safe condition is violated in the lab the FieldPoint software initiates a hardware signal that places the power supply into a standby or safe mode. The bias system is also managed by FieldPoint. The amount of charge applied to the individual banks is governed by simple computer adjustment. In this fashion, one is able to remotely set the bias to facilitate needed current levels in the plasma. Inherent to this operation is a software interlocked system that protects itself. A trivial example is the inability to execute both a charge and discharge command to the bias banks as such a command would damage the hardware.

3.6 Diagnostics

The q profile is determined by measuring the plasma current profile at the anode. The anode endplate is segmented into three concentric rings to measure the current profile (outer radii of .023, .052, and .081 m, respectively), see Fig. 3.11. Current flow to the anode is measured with Rogowski coils which are integrated prior to digitization. A simplistic technique to calculate q measures the current at three different radii from the segmented anode and then assumes that B_z is constant along the machine axis. Equation 1.2 is utilized to calculate q. In fact, B_z varies along the machine. With the measurement of I_p from the anode and compensation for the variation of B_z throughout the ReWM a better calculation of q is possible.

An improved method accounts for the non-uniformity of B_z by calculating a series of local measurements from a computer model that incorporates the solenoid's geometric position. The twist is then quantified by performing a Runge-Kunta integration along the field line with the local calculations of B_z and assumed constant current within a flux surface. Calculating q with this approach compensates for deviations from a uniform magnetic field stemming from the gaps between the four solenoids and is a necessary technique when $R_m \neq 1$. Without correcting for the

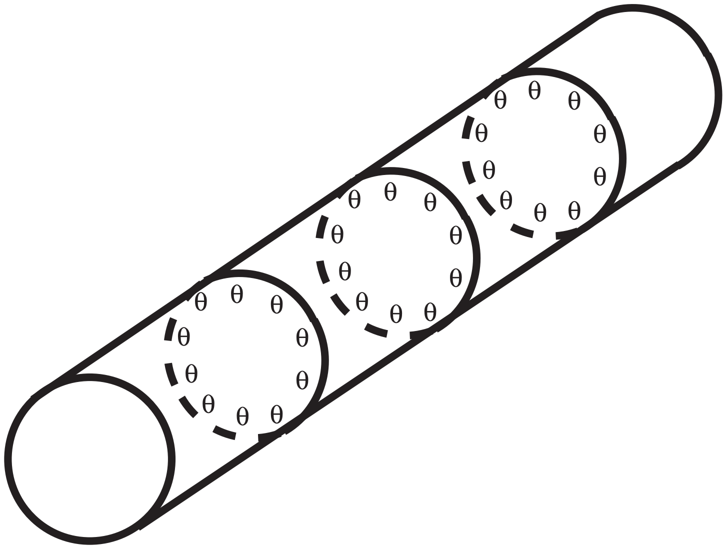

Figure 3.8 There are three rings just inside the vacuum vessel that anchor the B_θ coils. Coil location is depicted with a θ.

non-uniformity of B_z, $q_{r=2cm} = .8$ and $q_{r=5cm} = .96$ for a sample plasma shot. With the correction $q_{r=2cm} = .65$ and $q_{r=5cm} = .75$.

MHD activity is monitored by 120 flux loops. These coils are subdivided into 10 B_z coils along the machine axis, 3 sets of 10 B_p coils evenly spaced along the machine axis, and 80 B_r coils. The B_p and B_z coils are just inside the stainless steel wall and have an effective area of 45 cm^2, while the B_r coils (each 6.5 cm by 12.5 cm) with an effective area of 730 cm^2 provide the full two-dimensional structure of $B_r(r = a, \theta, z, t)$ just outside the wall. Figures 3.8 and 3.9 depict the location of the B_θ, and B_z coils, respectively, inside the vacuum vessel. The B_r coils are constructed with flexible circuit technology. The coils are 10 turn loops printed on a Kapton substrate. In Fig. 3.10 one sheet of B_r coils can be seen wrapped around the machine. Two such sheets provide full coverage of the plasma column. The signals from the flux loops and undergo analog integration prior to digitization.

The internal coils to measure B_p and B_z present a difficult problem to stable machine control. The central region of the ReWM where MHD studies are undertaken is essentially a tube. For a variety of reasons the machine functions best when this tube is capacitively and not directly coupled

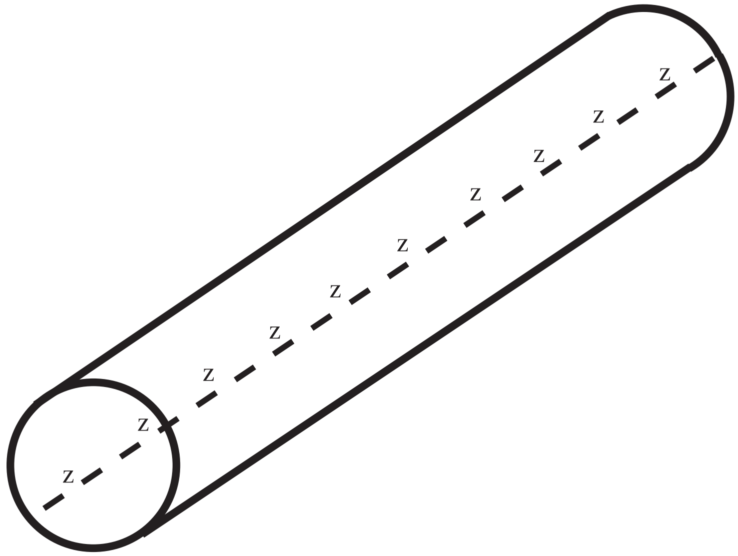

Figure 3.9 There is one strip running along the machine axis to which the B_z coils are affixed. Coil locations are marked with a z.

to ground. Thus, shortly after a shot is initiated, the tube itself supports a charge. The internal coils sit at the inner wall of the tube; however, the voltage across the coil must be brought outside the machine, itself at ground, to a bank of digitizers, also at ground. Therefore, the coils responsible for picking up B_p and B_z must not only be grounded at the digitizer, but also be designed stoutly enough to ensure they do not electrically short to the plasma or tube. Should the plasma etch the coils sufficiently to short the coil to the tube voltage, the digitizer bank would fail entirely.

Finally, the power supplies for the plasma guns produce four independent signals apiece. Each supply measures the arc and bias voltage with voltage isolation units and the arc and bias current with current shunts. The measurement across the current shunt is itself sent through a voltage isolation unit prior to digitization.

3.7 Data Acquisition

The data gathered and presented in this Thesis was obtained with a Computer Automated Measurement And Control (CAMAC) system with a General Purpose Interface Bus (GPIB) serial highway. With a control computer operating linux and proper coding, the GPIB highway allows for low

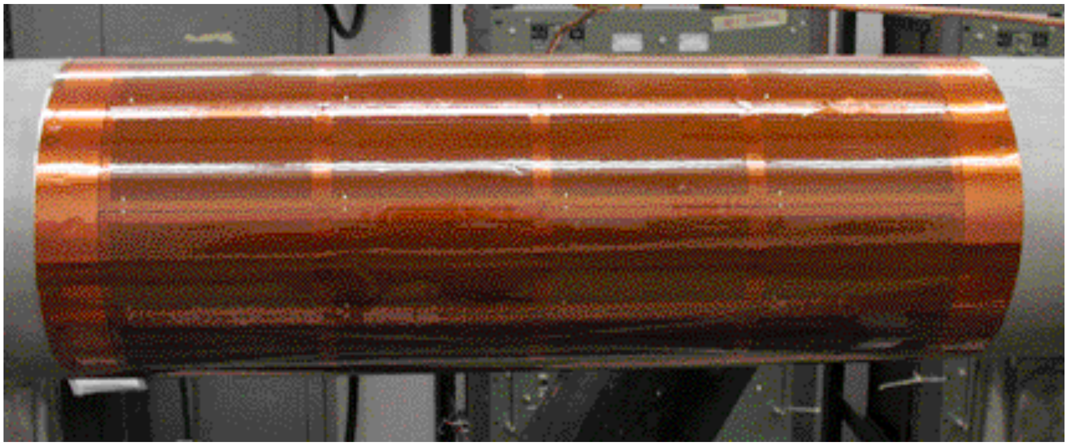

Figure 3.10 A picture of one sheet of B_r flux loops wrapped around the stainless steel vacuum interface used in some of the experiments. Two such sheets are needed for full coverage of B_r on the machine. Because the loops are printed on flexible circuit sheets, they can be easily wrapped around the cylinder. The solenoids have been removed in this picture.

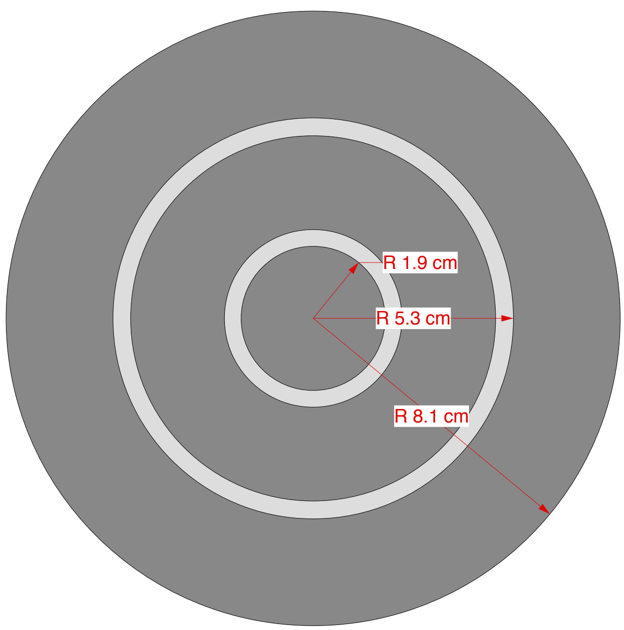

Figure 3.11 A facing schematic view of the anode and dimensions of each ring. By monitoring the currents flowing to the individual rings q can be calculated.

MHz data readouts. Experimental timing as well as digitizer setup, control, and readout are controlled by Interface Description Language (IDL) scripts. The IDL scripts utilize the tree structure inherent to MDSplus to store all recorded data into a particular node for later analysis. MDSplus does not control the data cycle or digitizer interface. MDSplus serves only as a tree structure to which data is written. With the interface as written the experimenter needs a mouse click to initiate a cycle which prepares the digitizers, fires the plasma, and collects the data through a preprogrammed timing cycle. The mouse click begins the sequential calling of hundreds of subprograms which themselves interface with the separate CAMAC crates, digitizers, and timing modules in the lab.

While the ReWM might be modest in scale compared to other machines studying plasma physics, it produces a significant amount of data on a per shot basis for its size. There are 120 magnetic signals, 76 signals from the gun power supplies, 3 to capture the plasma currents flowing to each section of the anode, and a host of other signals recorded for tracking of machine parameters. These 200 some signals are digitized with the LeCroy 6810, DSP 4012A controller, DSP 5200 series of memory, DSP 2810/2860 digitizer, Kinetic Systems 4022, and LeCroy 8212 and 8800 memory unit. These units are all 12 bit. All digitizers are controlled with LeCroy 8901A crate controllers and are triggered with a master trigger. The B_r magnetics and plasma currents from the anode are sampled at 1 MHz, while the B_p and B_z magnetics are sampled at 500 kHz. All magnetics and plasma current signals are synchronously sampled. The remaining signals are not as critical and recorded at lower speeds between 5 and 20 kHz. Generally these remaining signals are not synchronously sampled due to digitizer constraints.

All digitizers require some sort of initiation cycle that programs certain parameters (number of samples, clock speed, ratio of pre to post trigger samples) into the unit's memory. Sometimes this puts the unit directly into a digitization cycle. More often, a second set of commands is issued to start the digitization cycle or prepare the unit to receive an external trigger. At the conclusion of the cycle, the digitizer memory must be copied onto the computer's hard drive. Each and every digitizer requires this basic sequence of control. To illuminate the difficultly of issuing a single command from the IDL interface to the digitizer, the following example is offered.

A command that originates from the IDL environment is executed and calls a C wrapper/driver, written for the linux operating system. The command must be wrapped from some general ASCII text in IDL to a GPIB command at the C wrapper/driver; however, the wrapping must conform to the GPIB communication standard expected at the crate controller. The GPIB command is then coherent to the CAMAC crate controller, a GPIB device itself. The crate controller then issues commands to the proper digitizer in its crate by way of the CAMAC backplane. At this point the entire process must be repeated backwards, automatically, to report a successful communication. The crate controller must be instructed to listen for a response from the digitizer and subsequently send that response back to the computer. To complicate matters a bit, there is no common digitizer language. Each digitizer is controlled by a unique set and order of commands. There are different speeds at work as well. Linux communicates at one rate, while the CAMAC back plane at another, and the GPIB bus at a third rate. If any one entity in the cycle is forced to wait too long, the entire system crashes. The communication is much like the childhood game of telephone, with impatient and angry children.

Beyond the difficultly of completing a single communication cycle between the programmer and a digitizer, the reality is that every shot creates over 2.5 million 12 bit numbers at the digitizers. The digitizers must be prepared, triggered, and downloaded within a 4.5 minute shot cycle. The system must be stable, persistent failures in the cycle will lead to an unacceptable amount of down time. A fatal error in 5% of the shots is barely allowable from the standpoint of wasted effort in running the ReWM.

Beyond the code architecture responsible for collecting the data, the hardware component of the data cycle also required a significant amount of development. The digitizers are housed in CAMAC crates. A substantial amount of data is collected with the LeCroy 6810. This unit offers an unusual amount of flexibility in terms of input parameters for the signals. The trade off is power consumption and low signal density. A single CAMAC crate can house four 6810s. This CAMAC will in turn require 500 watts of electricity. Thus, the CAMAC crate manages to both collect 16 channels of data and serve as a medium sized space heater. The heating impact from one CAMAC is negligible; however, five such units (80 B_r signals and 16 signals per crate) operating over the course of an hour will easily raise the room temperature. Without industrial room cooling and forced air cooling for the CAMACs, the crates and digitizers fail within 90 minutes from excess heat.

Inherent to stable machine and digitizer operation is a solid low impedance ground system without ground loops. At best a ground loop would interfere with the data cycle, at worst it would cause a catastrophic fault in the plasma current which would damage any number of subsystems. For this reason, the turbo pump is actually maintained at ground, but electrically isolated from the machine. To eliminate ground loops, all pertinent devices in the laboratory are at machine ground and checked to ensure that no ground loops are present. Because various control boxes and the digitizers receive their power from a power transformer (480 V three phase to 120 V three phase) the entire system is unstable to capacitive coupling to ground. Mitigation of this problem requires specialized isolation transformers beyond the budget of the laboratory.

3.8 Mechanics of a Shot

Coordinating the system requires the proper timing of gas discharge for the plasma guns, firing the gun arc, firing the bias supply for the plasma current, and a trigger for the data cycle at the appropriate time. The gas is triggered initially because a 10 ms delay is built into the hardware between the gas puff and arc trigger. The delay ensures an ample supply of gas at the gun nozzle when the arc fires. After the gas puff but before the gun arc firing, the digitizers are sent a trigger to begin taking a set number of samples. 11 ms after the gas puff the arc fires, and 1 ms after the arc fires, the bias begins to source plasma current. The bias system actually has a timing program unto itself and the reader is directed to Appendix A for the details. The entire cycle is controlled by a two button interface program written in IDL. The first button performs all the digitizer initialization and set up. The second button starts the trigger cascade that sequentially triggers the gas, digitizers, gun arc, plasma current, and final writing of the data to the computer hard drive.

Finally, it should be stressed that none of these subsystems existed prior to the research presented herein. The machine, DC supply for the magnetic field, digitizers, control code for both machine and digitizers, ground network, and plasma current supply all had to be established prior to any research on the MHD of current driven kinks in the ReWM.

Chapter 4

No Wall Plasma Results

Two modes are observed in the ReWM when operated with a Pyrex wall. These modes grow when the safety factor $q = \frac{4\pi^2 r^2 B_z}{\mu_0 I_p(r) L}$ falls below one inside the plasma. The spatial structure of the first eigenmode, the ideal mode, is similar to the predicted structure for an ideal line tied external kink. The growth rate of this mode is slower than expected but commensurate with predictions when an evolving current profile is considered. The second mode, the resistive mode, is correlated to fast relaxation events which flatten the current profile. This broadening of the current column suggests reconnection activity in the plasma. The eigenmode of the resistive mode also suggests the magnetic topology is altered during these events.

This chapter reports results from experimental campaigns in which the ReWM is operated with a Pyrex wall. The majority of the data presented here is for plasmas created by the central seven guns. The bulk plasma has a radius $a \approx 6$ cm in this configuration. Without a conducting wall, τ_w is not relevant and the Alfvèn time ($V_a \approx 150$ km/s) is predicted to dominate dynamics in the plasma. Current driven instabilities are the focus of the work presented. The variation of current injected from the individual guns is small. There is less than a 10% percent difference between guns. Thus, the drive for the instabilities, the plasma current, is known to be consistent throughout the experiments. A schematic of the machine configuration is shown in Fig 4.1. These plasmas are biased with a voltage control scheme which allows for pulse lengths many times longer than τ_A. The mirror ratio of the magnetic field is maintained close to 1, while the field as a whole is varied between 250 and 500 Gauss. The principle diagnostics are the segmented anode which allows for

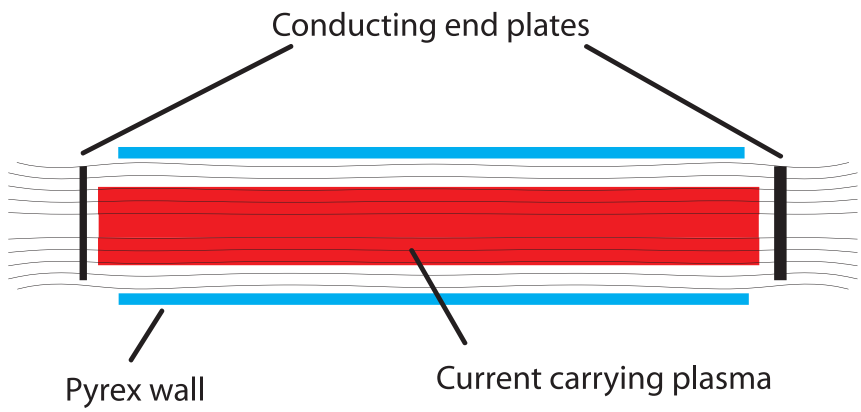

Figure 4.1 The experimental setup of the initial plasmas described in this Chapter. The wall is Pyrex and central guns are used. This leaves a region between the wall and plasma column of low density plasma. At both ends of the machine are conducting plates that satisfy the line tying boundary conditions.

calculations of q at three radii in the plasma and the 80 B_r coils. The Pyrex wall provides results which can be compared to the with-wall studies in Chapter 5.

4.1 Predicted Stability of the External Kink

The stability of the external kink without a conducting wall is covered in detail in Chapter 2. A brief reexamination of the results from that chapter are repeated here. Line tied screw pinches are unstable to the external kink when $q_a < 1$ but can be stabilized with a close fitting perfectly conducting shell. Figure 4.2 captures this relationship with plasma parameters relevant to the ReWM. The no wall external kink instability threshold mirrors the KS instability condition and is unstable when

$$q_a < 1, \tag{4.1}$$

with a growth rate given by

$$\omega^2\tau_A^2 = \frac{1}{2}\left(1 - \frac{1}{q_a^2}\right), \tag{4.2}$$

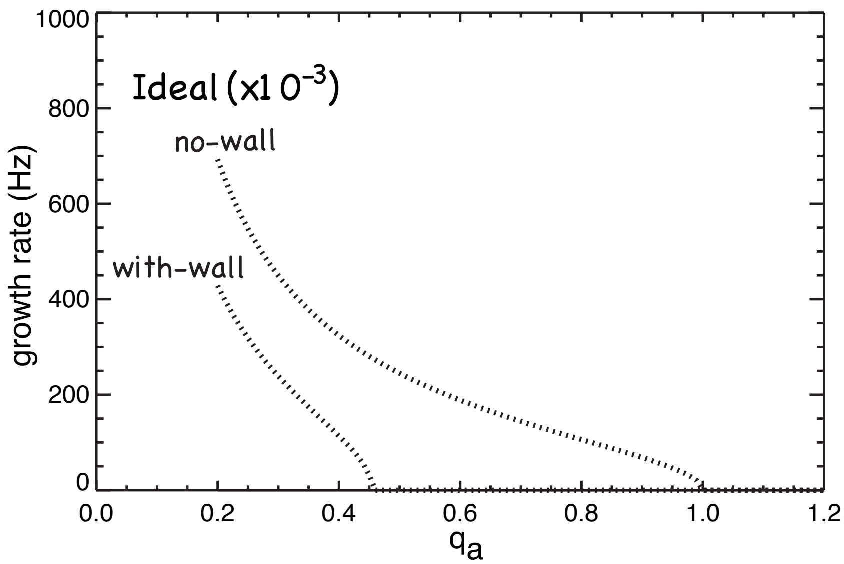

Figure 4.2 Growth rates for the ideal external kink in a line tied pinch with and without a perfectly conducting wall present. For the plot, the plasma radius a = 7.5 cm and the perfect wall radius is at $b = 10$ cm. Note that the ideal modes grow approximately 1000 times more quickly.

where $\tau_A = L/2\pi v_A$. With a close fitting perfectly conducting wall the external kink onset is determined by

$$q_a < 1 - \left(\frac{a}{b}\right)^2, \tag{4.3}$$

where b is the radius of the wall and a the radius of the plasma [36, 53]. The growth rate itself is modified from the no wall case but still Alfvénic. The ideal external kink grows very quickly once it becomes unstable with or without a perfectly conducting shell. Between the no wall and perfectly conducting wall limits is the regime of the RWM, which itself is presented in Chapter 5.

4.2 Modes in the Resistive Wall Machine

The time history of a typical plasma is seen in Fig. 4.3. The gun arc begins at $t = 0$ ms, with the bias for the plasma current applied at $t = 1$ ms and lasting for 8 ms. The ramp up of the current in Fig. 4.3 (a) corresponds to the q profile dropping in Fig. 4.3 (b). Notice that the current reaches its maximum within 2 ms of initiation. The abrupt changes in the q profile and current traces from

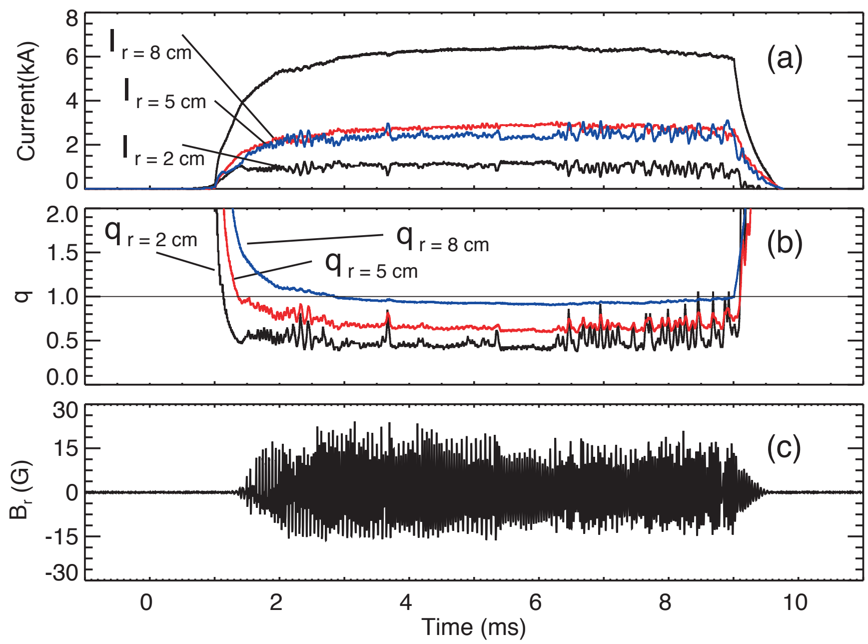

Figure 4.3 The time history of a typical shot in the ReWM. The current flowing to each segment of the anode (red, blue, and black correspond to measurements at r = 8.1, 5.2, and 2.3 cm respectively) as well as total current. In this shot B_z = 350 Gauss. The value of q at the three radii corresponding to (a) are shown in (b). B_r as measured by integrating the voltage from an external flux loop is plotted in (c). MHD activity is large when $q < 1$.

the segmented anode are solely a result of plasma dynamics; external conditions are unchanged throughout the plasma pulse. Figure 4.3 (c) shows B_r from a flux loop near the center of the plasma at $L = 0.6$ m. In general, strong MHD begins when q drops below 1 and saturates within a millisecond. A concern with the voltage controlled bias scheme is that the inherent RC droop in the current will effect the MHD of the plasma. This is not an issue in these plasmas because the MHD saturates well before any noticeable decrease in the current.

The top plot of Fig. 4.4 is an example of a spectrogram described in Appendix B. The power spectra are calculated with 1024 samples ($\approx$ 1 ms with data recorded at 1 MHz) every 0.5 ms. The brighter colors correspond to larger normalized peaks in the power spectrum. At the bottom of Fig. 4.4 are the traces for q measured throughout the shot. Immediately obvious from the spectrogram is that at least two distinct modes are seen that are intermittently excited during the shot. The high

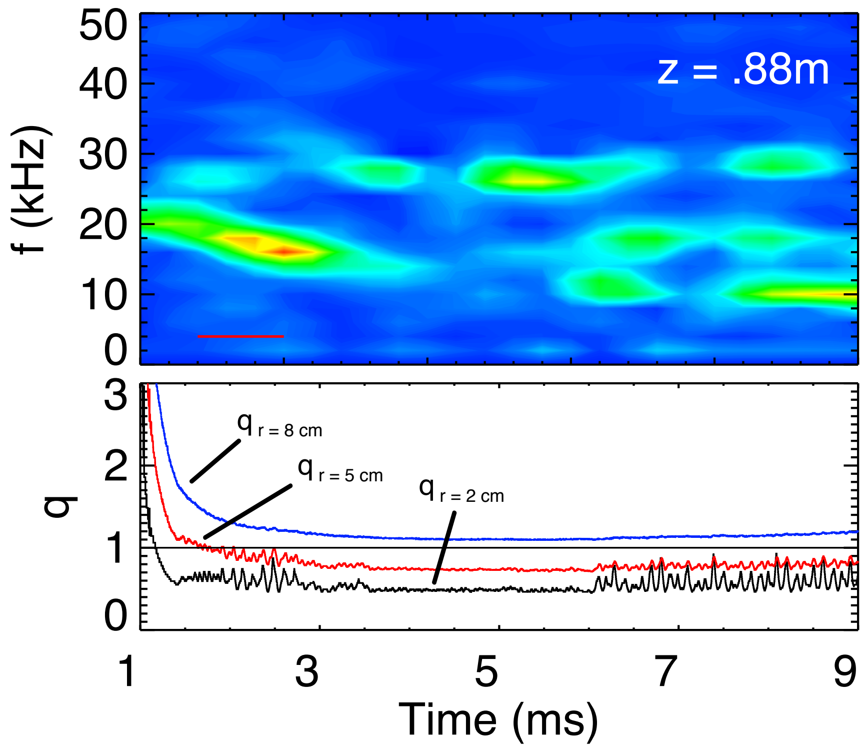

Figure 4.4 A spectrogram of B_r in the top plot with the measured values of q in the lower plot. Bright spots indicate mode presence in the plasma. The 10 kHz feature dominates when the q profile is not quiescent. Conversely, the high frequency mode (30 kHz) dominates when the q profile is flat. Mode dynamics can be studied by observing the brightness and frequency evolution over the course of the shot of a particular mode.

frequency mode, around 30 kHz, is dominant during quiescent periods in the q profile. When the q profile is undergoing relaxation dynamics, seen later in the shot and discussed in Section 4.3, a lower frequency mode dominates around 10 kHz. The feature close to 20 kHz is an overtone of the 10 kHz mode.

Figure 4.5 is a contour plot of B_r on the machine surface made from a selected range of frequencies (20-30 kHz). A clear $m = 1$ signature is present. In the figure, the three plots above the contour plot are measurements of $B_r(\theta)$ at three different axial points on the ReWM. Each ring of flux loops corresponds to one of the three vertical black lines on the contour plot. $B_r(z)$ is plotted below the contour plot. It is taken from the horizontal black line on the contour plot. In the no

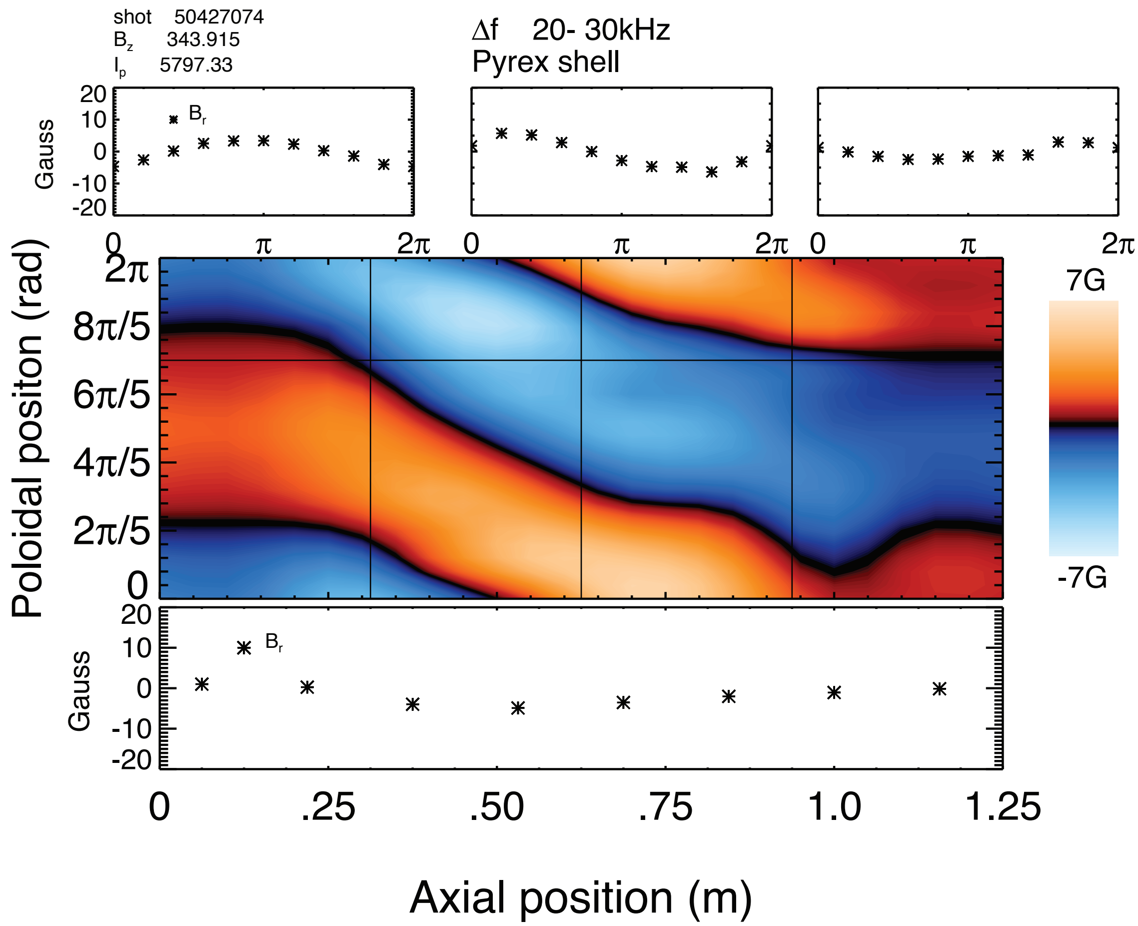

Figure 4.5 The reconstructed eigenmode of the high frequency mode. The clear helical structure of the mode can be seen in the contour plot. The band path filter is from 20 to 30 kHz. Plotted above the eigenmode are poloidal slices of B_r, taken from the vertical lines drawn over the contour plot. Below is $B_r(z)$ from the horizontal line seen on the contour plot.

wall studies, the additional plots of $B_r(z)$ and $B_r(\theta, z \approx .25, .5, .75m)$ are only meant to reinforce data shown in the contour plot, no extra information is presented. In addition to the robust $m = 1$ structure, the contour plot captures the helical structure of the mode as well. The mode is peaked in the middle and decreases but does not go to zero towards the ends.

Figure 4.6 is a contour plot of the mode at 10 kHz, initially identified in Fig. 4.4, and highlights the different characteristics it has from the mode at 25 kHz. This mode is smaller, 3 G compared to 7 G for the 25 kHz mode. More noticeable though is that the low frequency mode has an eigenmode unlike the mode at 25 kHz. The mode is at a maximum at the anode and nonexistent at the cathode. The helical structure is still present but close inspection reveals a helicity distinct from the previous mode. Recall from Fig. 4.4 that these two modes dominate the plasma when different dynamics are more pronounced. When the current profile is undergoing relaxation events, manifested in the choppy q profile, the lower frequency mode dominates. We have chosen to refer to the low frequency mode as the resistive mode because its structure suggests resistivity in the plasma (discussed in Section 4.3). Conversely, we have labeled the high frequency mode, the ideal mode, because its structure largely matches predictions from theory (discussed in Section 4.5).

The ideal eigenmode saturates into a rotating, helical equilibrium. Fig. 4.7 shows the power spectrum of a single B_r trace with no relaxation activity occurring in the current profile in (a), while in (b) the plasma is undergoing many reconnection events. Figs. 4.7 (c) and (d) show $B_r(z, \theta = const)$ profiles along the machine axis stepped a half period in time. The peak in (a) and (b) at 25 kHz represents the rotation of the ideal mode. The rotation rate itself is consistent with the $E \times B$ rotation from a radially varying plasma potential. The potential in the plasma is due to the biasing of the plasma guns that drives the current. Plotting the modes stepped a half period in time allows one to see the spatial oscillation of the modes. The eigenmode of the resistive mode, shown in Fig. 4.6 and Fig. 4.7 d. is discussed further in the below section.

4.3 Reconnection

In addition to the two modes in the plasma, there is evidence for abrupt current profile relaxation. This behavior is most easily identified as the spike-like features on the q profile evolution, and can occur as discreet events (such as the event at 3.7 ms in Fig. 4.3), or periodically at a regular frequency (such as the phase between 6 and 9 ms). Fig. 4.8 shows profiles of the current density and q before and after a relaxation event (as measured directly by the anode rings). The relaxation causes the current density to decrease near the center of the plasma while increasing at the edge. Hence q flattens and approaches 1 throughout the plasma. Recall that the current and plasma sources are stable throughout the shot. Variation of total current between the guns is less than 10%.

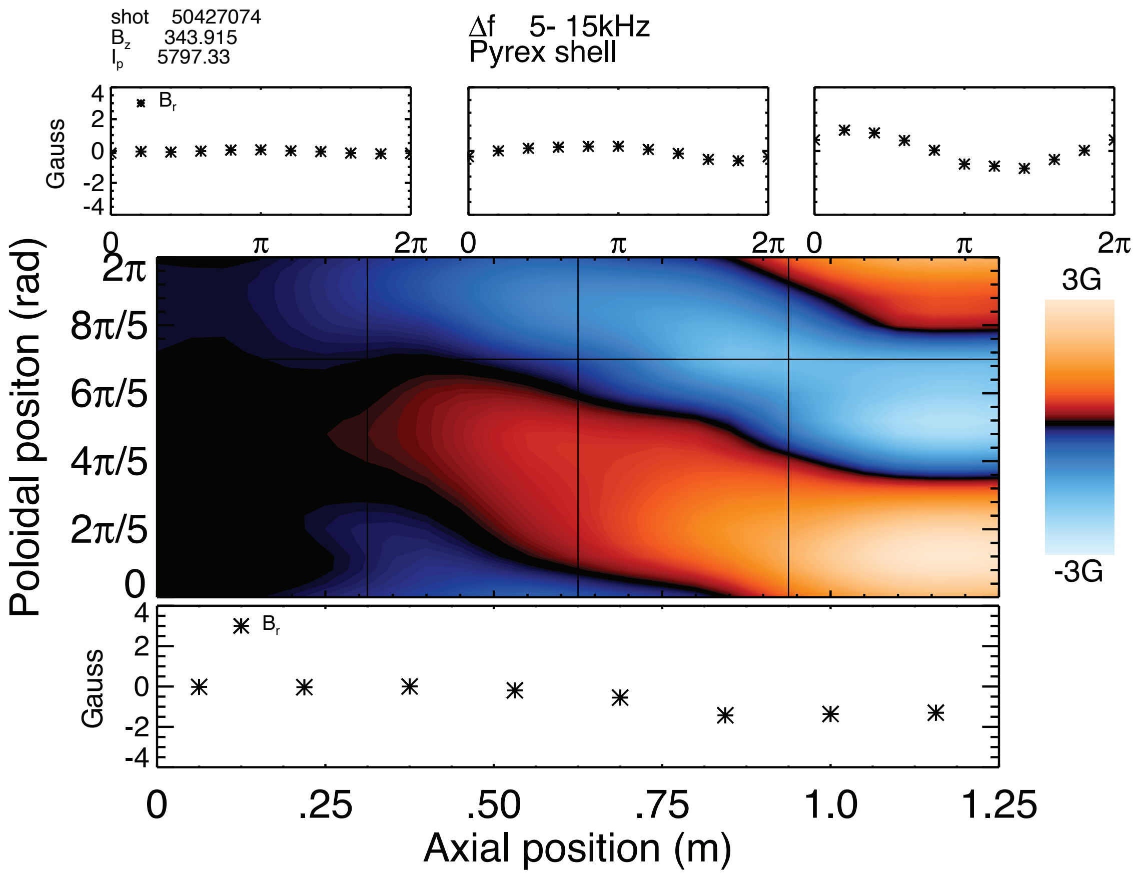

Figure 4.6 The reconstructed eigenmode of the low frequency mode. This mode is localized to the anode end of the machine and has a helical displacement like the high frequency mode, but with a different helicity. The band path filter is from 5 to 15 kHz. Plotted above and below the contour plot are subplots of B_r as in Fig. 4.5.

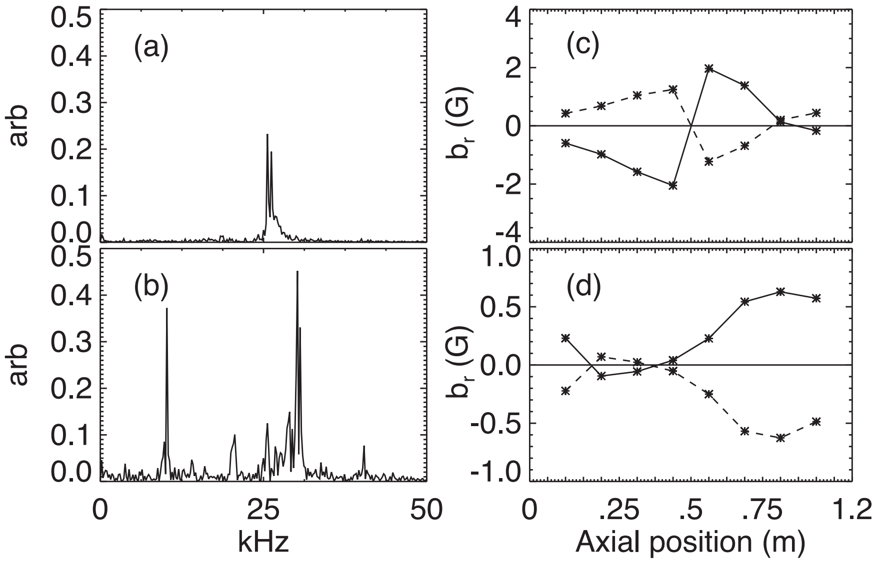

Figure 4.7 In (a) [$B_z = 270$ Gauss, $I = 5000$ amps] and (b) [$B_z = 270$ Gauss, $I = 7000$ amps] the frequency spectrum of a single fluxloop from the saturated phase with and without relaxation. The spectra are taken for a time interval from 5 to 9 ms and correspond to the saturated phase. In (c) and (d) the solid and hashed lines are the instantaneous axial profiles of B_r at fixed poloidal angle, band pass filtered, and then plotted at two different times separated by half a period. The standing wave structure shown in (c) corresponds to the mode at 25 kHz in (a), while the low frequency mode in (d) corresponds to the 10 kHz mode in (b).

The magnetic fluctuations associated with the relaxation events are not consistent with the eigenmode structure of a line tied ideal kink mode predicted in one dimension in Fig. B.2 in Appendix B. Additionally, the frequency spectrum changes in the presence or absence of relaxation. Without relaxation, a single, monochromatic mode is observed at high frequencies (Fig. 4.7 (a)), while in the presence of periodic relaxation, a low frequency mode, the resistive mode, appears with an amplitude that is small near the cathode end but large at the anode end of the machine seen in Fig. 4.7 (d) and Fig. 4.6. The large fluctuations at the anode end can only occur if the plasma topology changes. Ideal MHD activity preserves the mapping of current from the cathode end to fixed points on the anode end, while resistive reconnection within the plasma allows the mapping to be broken. The current source, fixed in space due to the plasma guns, exits the plasma

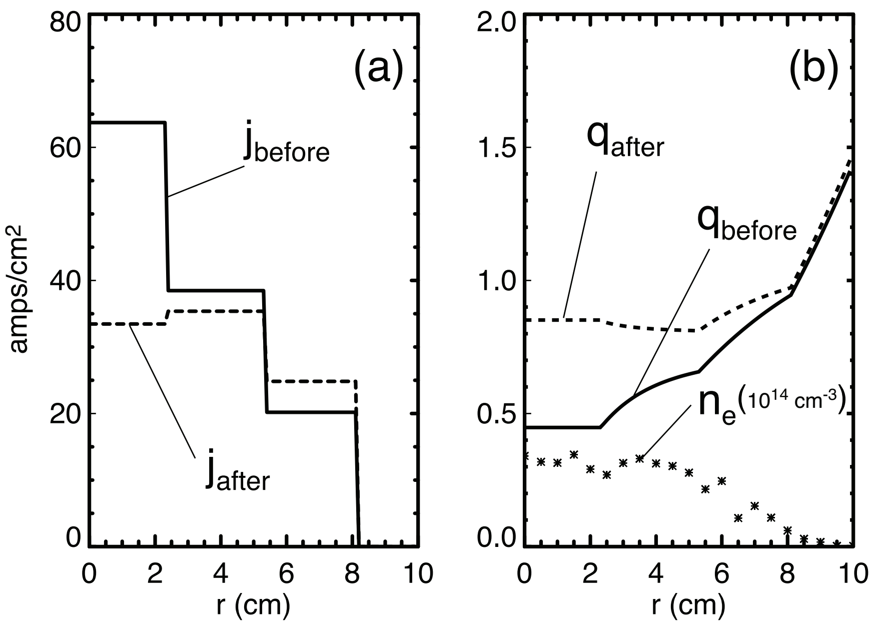

Figure 4.8 (a) The current density measured by the segmented anode (solid and dashed lines correspond to before and after the relaxation event at 3.7 ms in Fig. 4.3). (b) The q profile corresponding to the current density is plotted along with the density profile as measured by a Langmuir probe.

at the anode at a different radius when reconnection occurs, resulting in the large low frequency fluctuations at the anode end in conjunction with relaxation events.

The argument relating antisymmetic eigenmodes to reconnection is also made in References [38, 63]. In these numerical studies it is possible to trace an individual field line and see effects of resistivity in the plasma. Without reconnection, field lines have some mapping between the endplates. With reconnection, the field lines now map to a different position. Both numerical studies report a signature of reconnection to be a mode that originates like the ideal mode, but terminates differently. This behavior precisely describes the resistive mode in the ReWM.

4.4 Onset and Growth of the Ideal Mode

The evolution of the MHD activity (shown in Fig. 4.9) prior to saturation shows a $m = 1$ kink mode begins to grow when q drops below 1 at the center of the plasma. Fig. 4.9 (c) shows the amplitude of the poloidal $m = 1$ mode from one band of 10 flux loops at fixed axial location. The

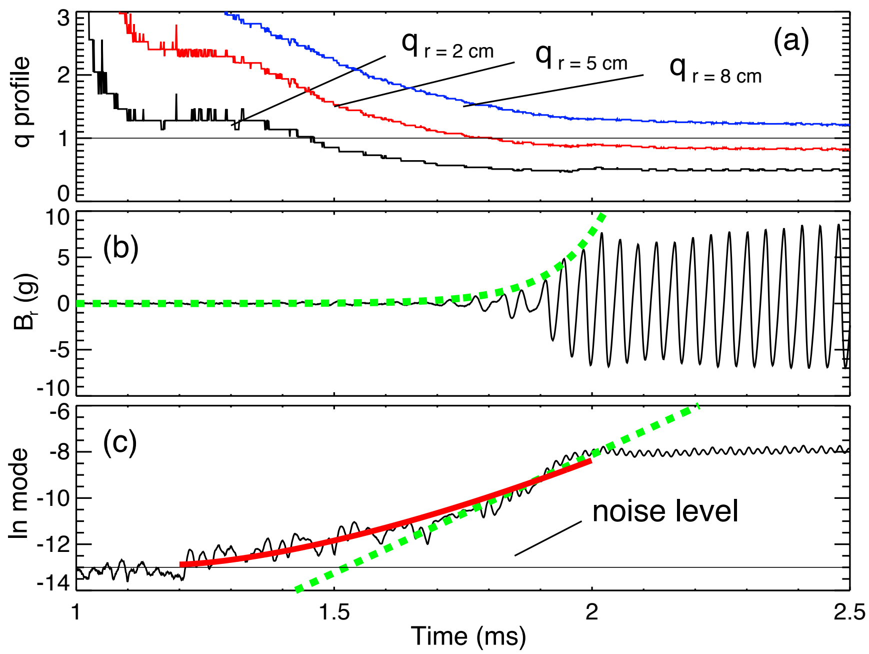

Figure 4.9 (a) q profile evolution near marginality (B_z = 270 Gauss). (b) The time history of B_r for a single flux loop and the best fit exponential. In (c) the logarithm of the $m = 1$ mode amplitude is plotted with an $e^{\gamma t^{3/2}}$ curve and the simple exponential. The horizontal line across the bottom in (c) is the noise level of the signal and indicates that the mode first becomes detectable at 1.22 ms.

sinusoidal variation in Fig. 4.9 (b) reflects plasma rotation, and the envelope highlights the growth of the mode. The mode begins to grow when $q_0 = q(r = 0) \approxeq 1$. Recall from Fig. 3.5 that the guns produce a peaked current profile which forces $q_0 < q_{r=2cm}$. This justifies the conclusion that it is $q_0 < 1$ and not $q_{r=2} < 1$ that determines the mode onset condition.

The growth rate is not accurately represented by a single number due to the increasingly unstable current profiles. If the equilibrium is static the amplitude should grow according to $e^{\gamma t}$. The straight dashed line in Fig. 4.9 (c) (corresponding to $\gamma = 10.22 \times 10^3$ sec^{-1}) is a good fit only after 1.7 ms. Between 1.2 ms and 1.7 ms the growth rate is smaller as the plasma is only marginally unstable. It can be shown that if the plasma equilibrium changes slowly with time, the mode amplitude grows according to $e^{\overline{\gamma}(t)^{3/2}}$ [7]; the $\overline{\gamma}(t)^{3/2}$ dependence fits the data throughout the growth phase, with $\overline{\gamma}$ =6.31$\times 10^3$ sec$^{-2/3}$.

4.5 Corollary Experiments

Separating the power supplies for the bias and plasma production circuits allows for the creation of plasma without any external bias current. With the cathode array the central gun can be pulsed and biased, while only pulsing the surrounding six guns. The schematic of this experiment is shown in Fig. 4.10. This ability allows one to experimentally examine the stability of various current profiles. Calculating such an effect is very difficult and points to the ability of the ReWM to probe current profiles and their resulting MHD. Figure 4.11 is the compilation of such an experiment. On the left three trances a single gun is pulsed and biased which forces q_a below 1. When $q_a < 1$ the MHD activity, measured with B_r, increases dramatically. For comparison, the middle three plots show reduced MHD when q_a is above 1. The plasma in the middle traces is created with one gun pulsed and biased. On the rightmost trio, seven guns are producing plasma; however, only the central gun is carrying an external bias. The larger plasma has the effect of raising the value of q_a above 1 which in turn almost eliminates the measured MHD.

The physics behind the stabilization can be thought of two ways. Intuitively, surrounding the central current column with a layer of conducting plasma should be stabilizing. The outer plasma mimics a highly conducting wall. It was previously noted that external kinks can be partially stabilized with a close fitting conducting wall. In this experiment the stabilization is directly seen in the reduced level of recorded MHD. In another way, the external kink seen with one gun becomes an internal kink, unobservable outside the plasma with the surrounding unbiased plasma. The unbiased plasma can be thought of as readjusting the current profile of the entire column. This argument is shown in Fig. 4.12. With the additional guns pulsed, the plasma has a larger radius, but the current is unaltered. This forces q_a to increase. With the extra plasma, $q_a > 1$ and the external kink is stable.

Rigid comparisons between the ideal linear theory in Reference [28] and the plasma in the experiment are improper. A discussion of differences between the ReWM plasma and assumptions used to model it are presented in Section 6.4. An interesting general examination of the theory concerns the validity of the displacement vector ξ and the degree to which it accurately describes

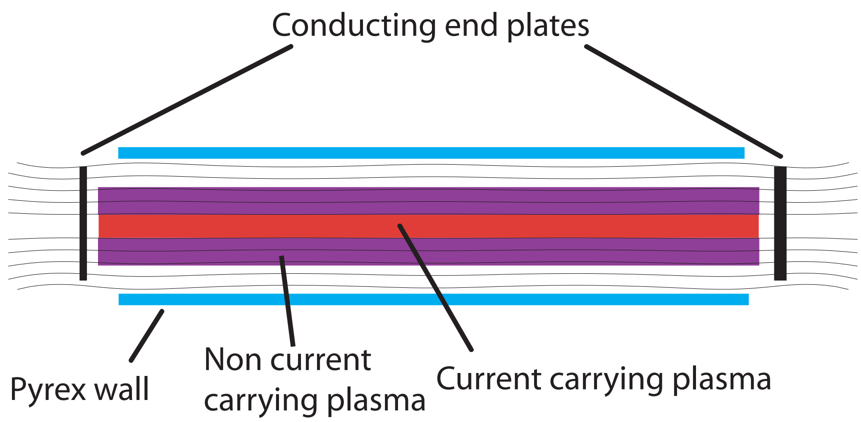

Figure 4.10 The experimental setup of the plasmas in this set of experiments. The central gun is arced and carries a bias. The surrounding 6 guns are only arced to produce plasma. No current is carried in this region.

the eigenfunction of B_r. In principle, one could put plasma parameters into the calculation for B_r, expressed in Equation B.2, and make direct comparisons. This step has been performed and can be found in Appendix B. Machine parameters determine the one dimensional eigenmodes plotted in Figs. B.2 and B.3. However, the likelihood of gaining any information from one dimensional comparisons is limited due to the known differences between the model and experiment. The full coverage of the vacuum vessel with B_r coils allows for general trends to be seen in the eigenmode structure without being distracted by extraneous details. Trends between experiment and theory are important and should be more robust than particular predictions.

An important feature of ξ, given in Equation 2.22, is its dependence on q_a. To test the validity of the predicted eigenmodes, B_r is generated for plasmas with different values of q_a. In Fig. 4.13 q_a is adjusted from 0.33 to 1.17. One can clearly see that as q_a increases in Fig. 4.13 the helicity of the mode decreases. The pitch of the helix is more horizontal. A similar trend is seen in experimental plasmas, shown in Fig. 4.14. In Fig. 4.14, q_a is varied from .5 to 1.4. Inspection of Fig. 4.14 reveals the same straightening of the mode as q_a increases. Directly comparing real and predicted mode structures for a particular value of q_a is problematic; however, the trend of less helicity with larger q_a is maintained in both theory and experiment.

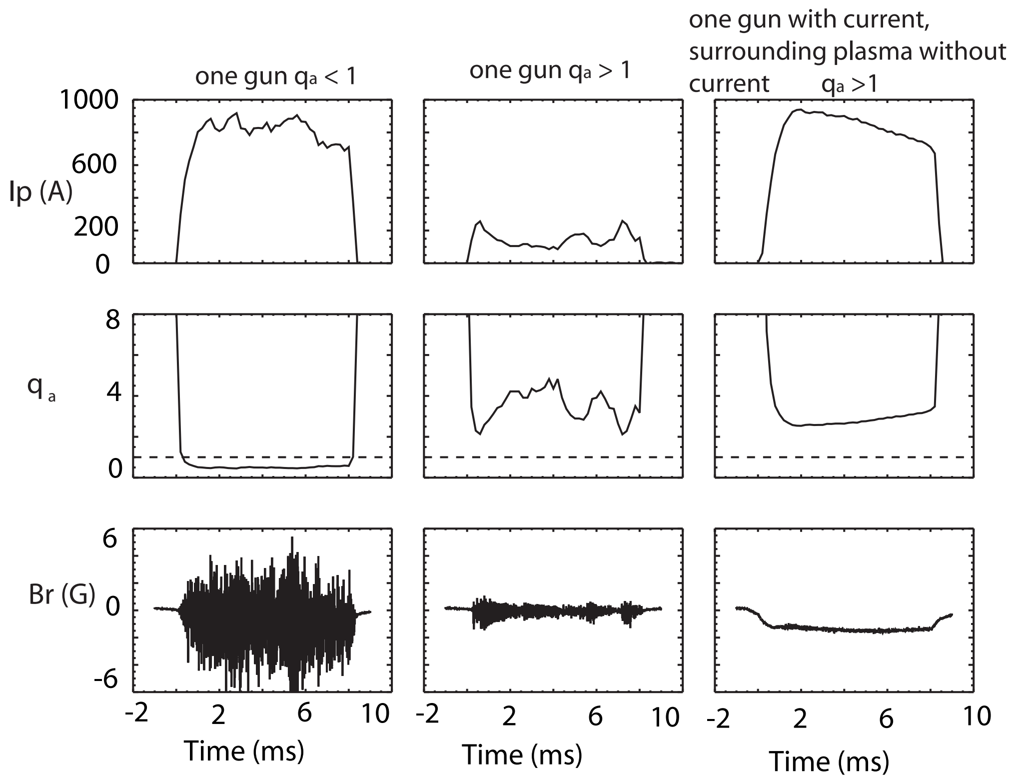

Figure 4.11 On the left three plots a plasma is shown to be unstable when $q_a < 1$ as seen by increased MHD in B_r. In the middle three plots, the same plasma can be seen to be stable when $q_a > 1$, again as viewed through the MHD trace in B_r. Finally, in the right three plots, a surrounding plasma without plasma is demonstrated to stabilize the plasma from the left most plots.

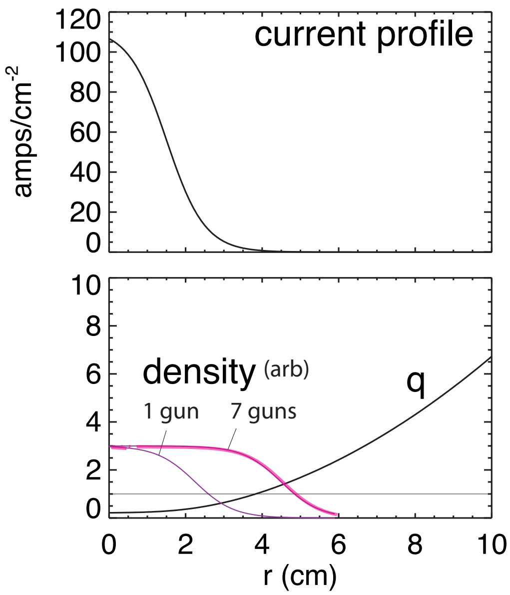

Figure 4.12 By increasing the size of the plasma while keeping the current column unchanged, the plasma effectively has a larger value of q_a. This effect can be seen by looking at the intersection of q and the density, when seven guns are used the intersection occurs when $q > 1$.

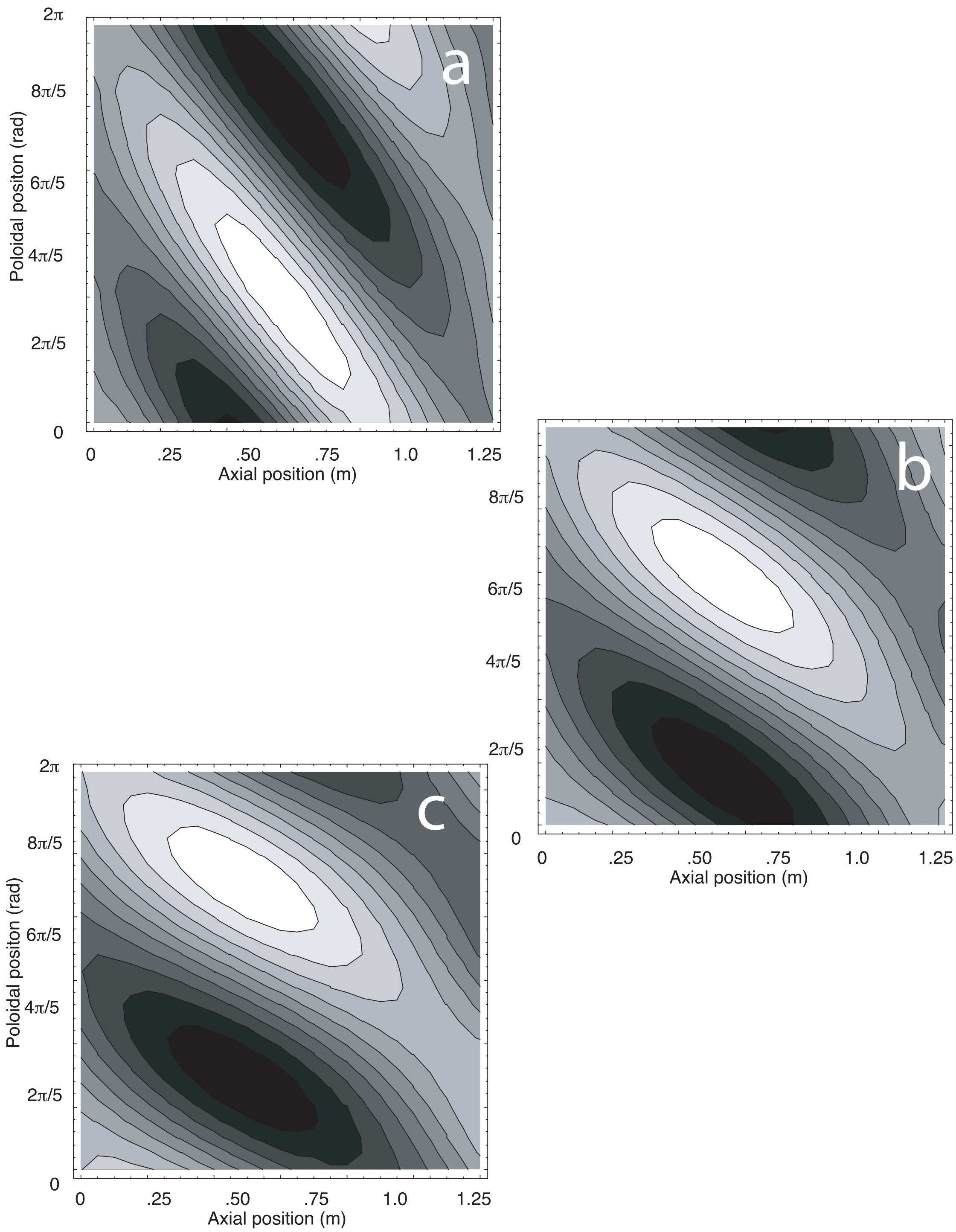

Figure 4.13 Contour plots of the predicted eigenmodes for plasmas in the ReWM. The mode's maximum and minimum are represented by the light and dark islands. For the plots, $I_p = 5000$ A, a = 8 cm. B_z is adjusted from 100 to 225 to 350 G, in (a), (b), and (c), to adjust q_a from .33 to .75 to 1.17. As q_a increases the mode has less helicity or twist.

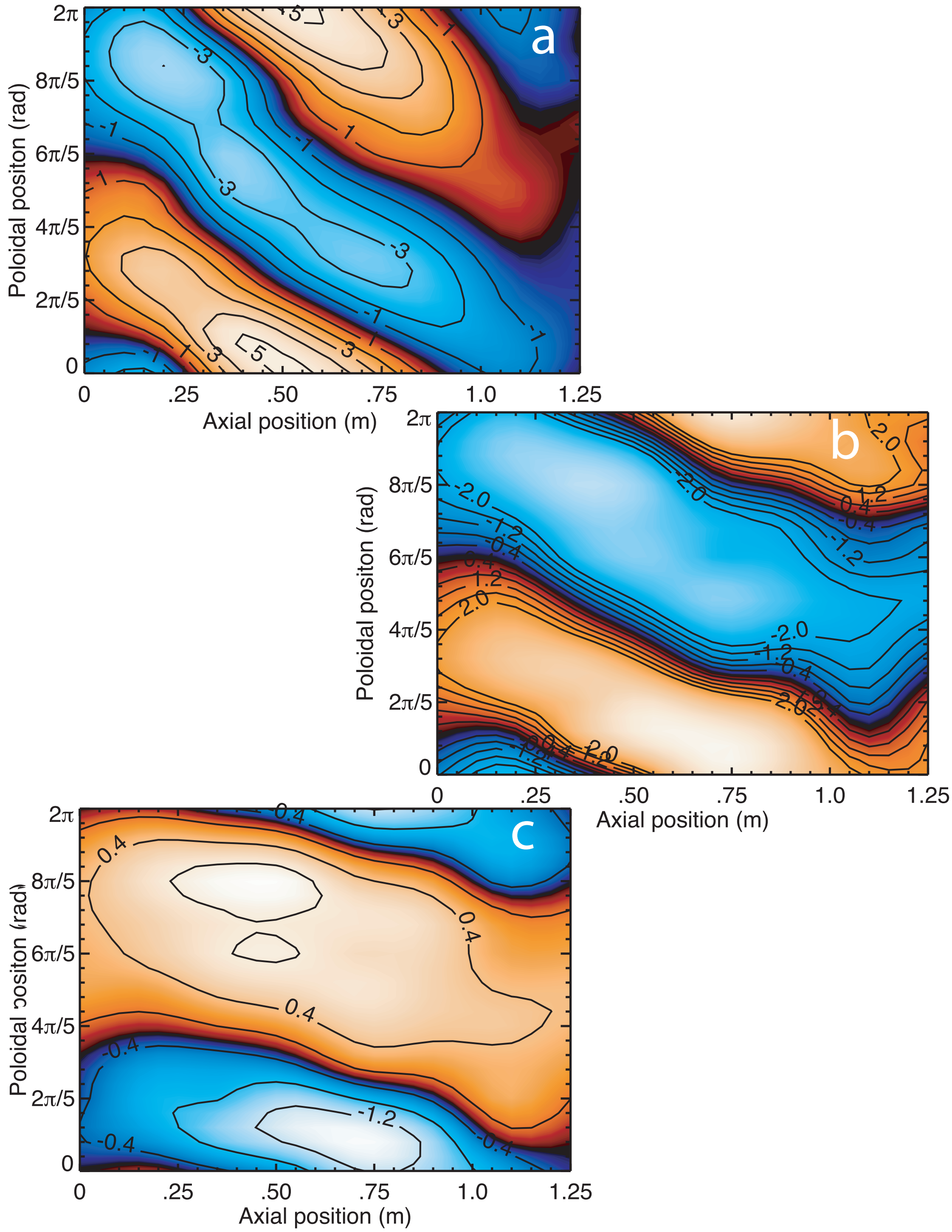

Figure 4.14 Contour plots from the measured values of B_r. The mode's maximum and minimum are represented by lighter shades of orange or blue. In (a) q_a = .56, (b) q_a = .85, and for (c) q_a = 1.4. Plotted on the contour are lines of constant B_r, in (a) the line of -3 corresponds to -3 G. As predicted in Fig. 4.13, the helicity decreases as q increases.

Chapter 5

Results From a Plasma with a Conducting Wall

Experiments on a linear line tied screw pinch have been performed with conducting wall boundary conditions. Modes observed with an insulating boundary are still present. The growth and onset of these modes with a conducting wall at the boundary suggests that these are internal modes. A third mode is observed in conjunction to the internal modes. Growth of this mode scales with the wall time and indicates that this is the RWM. While the eigenmode of the RWM matches predictions from theory, its onset is slightly different from $q_a = 1$. Empirical observations of interactions between the internal kinks and external RWM are presented.

The Pyrex wall in the ReWM was removed and results from experimental campaigns with two different conducting boundary conditions are reported. The Pyrex tube was initially replaced with a stainless steel tube with $\tau_w \approx$ .5 ms, where $\tau_w = \mu_0 b \delta_b / \eta_w$ with the wall radius equal to b. Following the stainless steel experiments, a thin copper sleeve was slid over the stainless steel. The composite wall has $\tau_w \approx$ 7 ms. Schematics of the machine configurations are shown in Fig. 5.1 and Fig. 5.2. One goal of the experimental campaigns has been to diagnose the growth and onset of the RWM. Understanding the RWM and its relationship to τ_w in the ReWM is a prerequisite for future attempts to stabilize the RWM with spinning shells.

The plasmas in these experiments are largely unchanged from those described in Chapter 4. Plasmas are created with the central six (no central gun) or seven guns being arced and biased. The anode described previously is used. In addition to the 80 B_r coils, 30 B_θ and 10 B_z flux loops have been installed just inside the vacuum wall. Further details about the flux loops can be found in

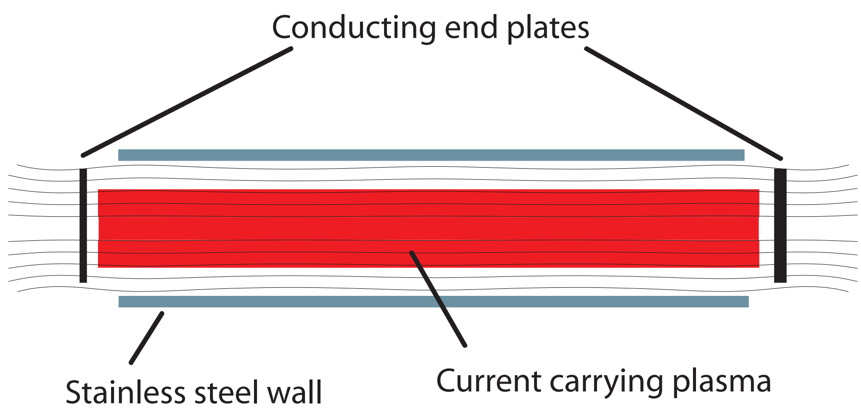

Figure 5.1 The experimental setup for some of the plasmas described in this Chapter. The wall is stainless steel, with $\tau_w \approx .5$ms. Only the center guns are used. This leaves a region between the wall and plasma column of low density plasma. At both ends of the machine are conducting plates that satisfy the line tying boundary conditions.

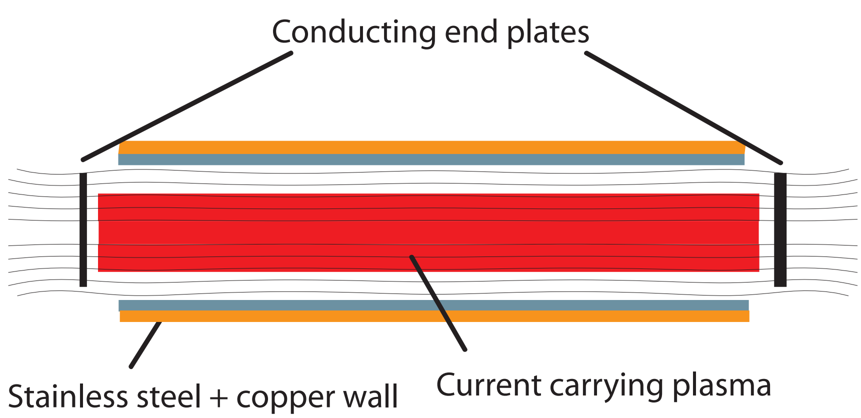

Figure 5.2 The addition of a close fitting outer copper sleeve to the configuration described in Fig. 5.1. With the two walls together, $\tau_w \approx 7$ms.

Section 3.6. The plasmas reported in this Chapter have an axial field between 250 and 400 Gauss with $.95 < R_m < 1.2$.

5.1 Predicted Stability of the RWM

Figure 2.2 from Section 2.6 is plotted again in Figure 5.3 to refresh the differences between the ideal external kink and the RWM. With no boundary, the external kink begins to grow when $q_a < 1$. A close fitting perfect conductor can stabilize the mode. From Fig. 5.3, the kink with an ideal wall is stable when $q_a > .45$. At this point the external kink destabilizes and grows. A resistive wall, one in which the eddy currents decay away, has slower growth. Onset for the RWM is identical to the no wall external kink. The RWM (solid trace) in Fig. 5.3 is roughly 1000 times slower than the no wall or perfect wall kinks. With a single resistive wall, the RWM growth rate is

$$\gamma = \frac{2}{\tau_w} \frac{1 - q_a}{q_a - \left(1 - \left(\frac{a}{b}\right)^2\right)}, \tag{5.1}$$

as derived in Chapter 2.

5.2 Impact on Modes With a Conducting Wall Present

The two dominant modes found in no wall plasmas still exist when a conducting boundary condition is present, but with an altered eigenmode. In Fig. 5.4 spectrograms of B_θ from two locations of z (θ unchanged) and corresponding q profile evolution are shown. In these plots the plasma has the composite copper and stainless steel wall; however, results without the copper are largely the same. Ignoring the almost constant peak at 1 kHz, three modes are seen. These modes are the same as those discussed in Chapter 4. The peak around 35 kHz is from the ideal mode while the lower 10 kHz peak is the resistive mode. The feature at 20 kHz is an overtone of the resistive mode at 10 kHz. The frequency at which the resistive and ideal mode appear corresponds to their rate of rotation in the ReWM. Comparing the spectrograms at $z = .56$ m and $z = .84$ m allows one to see that the resistive mode is localized at the anode end ($z = .84$), as opposed to the ideal kink which peaks in the middle of the machine ($z = .56$).

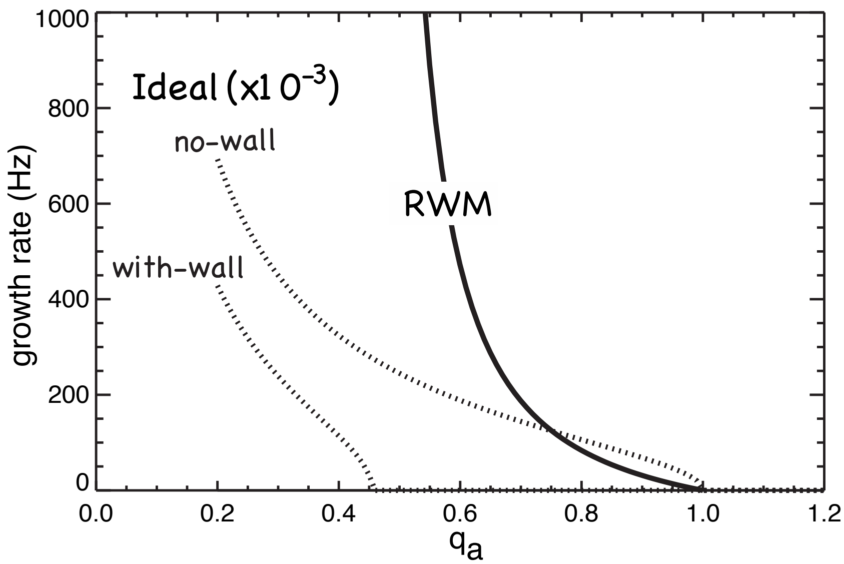

Figure 5.3 Growth rates predicted for ideal modes and RWM in a line tied pinch. The plasma radius a = 7.5 cm, the stationary wall radius $b = 10$ cm. The wall time $\tau_w \approx 10$ ms. Note that the ideal modes grow approximately 1000 times more quickly.

In Fig. 5.5 and Fig. 5.6 the B_r eigenmodes for the ideal and resistive modes are seen. As explained in Appendix B, these plots were generated by applying a band pass filter to the power spectrum from a B_r signal and then converting the now limited power spectrum back into a signal of B_r measured against time. These are the reconstructed eigenmodes with the composite wall boundary condition. Note in these Figures that values for B_θ and B_z are shown above and below the main contour plot. With only the stainless steel boundary, the eigenmode shapes are unchanged but the amplitude is larger (≈ 1 G). Differences between these modes and those seen in the no wall plasmas include a smaller amplitude in B_r and inversion in relative strength. The resistive mode is larger than the ideal mode in plasmas with either stainless steel or stainless steel and copper at the boundary. The resistive mode's association with the relaxation events seen in the current and q profile is maintained.

Generally the ideal and resistive modes have a similar eigenmode structure when the experiment has an insulating or conducting wall at the boundary condition. The amplitude of the eigenmode in B_r is different but explained below. The ideal mode maintains a clear helical twist while

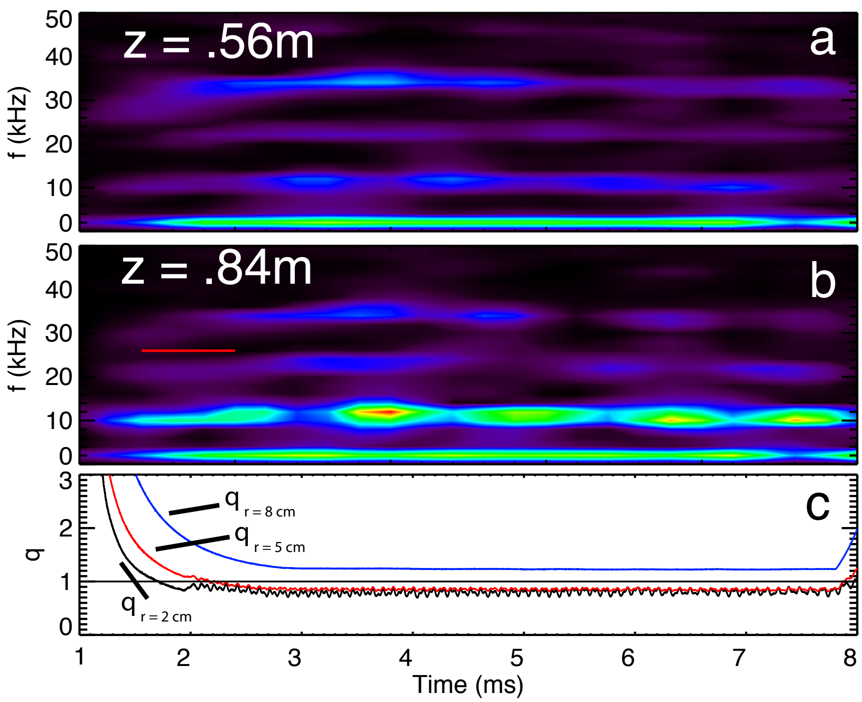

Figure 5.4 In (a) and (b) are spectrograms of B_θ measured at L = .56 m and .84 m, respectively. In (c), the q profile. The high frequency mode is seen at 35 kHz and peaked at the center of the machine, while the low frequency mode is at 10 kHz and largest at the anode.

the resistive mode is localized to the anode end. Unlike the no wall example, there is little to no helical component present in the resistive mode as seen in Fig. 5.6.

If these modes were external kinks either conducting boundary condition would stabilize them. The high rate of rotation for each mode is sufficient to satisfy the ideal wall boundary condition. Furthermore, the eigenmode is merely altered by the conducting walls, not suppressed. Only the amplitude of B_r is reduced in each mode. The modes are robustly present in B_θ and B_z. Inspection of the plots above and below the contour plots in Fig. 5.5 and Fig. 5.6 highlight the diminished size of B_r while B_θ and B_z are unchanged. With the rapid mode rotation, $B_r \approx 0$; however, the residual amplitude is further reduced by virtue of the fact that the measurement takes place outside of a conductor. The electro-magnetic skin effect diminishes the amplitude of B_r.

The onset of these two modes, seen in Fig. 5.7, is not indicative of an external kink. The normalized mode amplitude ($B_r(mode)/B_z(applied)$) is plotted against q measured at r = 2 and

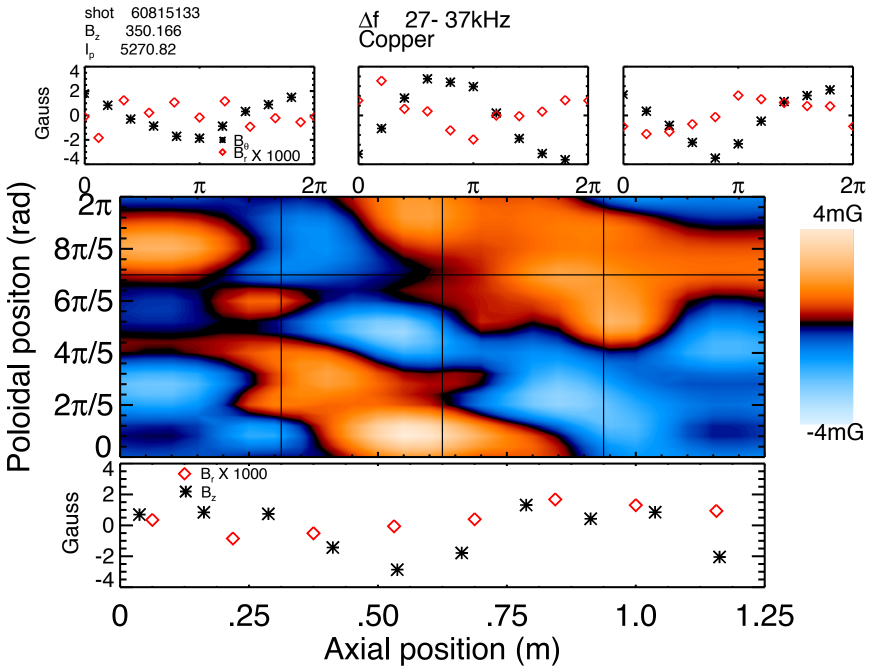

Figure 5.5 The reconstructed eigenmode of the high frequency mode. The helical structure of the mode can be seen in the contour plot. The band path filter is from 27 to 37 kHz. Plotted above the eigenmode are poloidal slices of B_r and B_θ, taken from the vertical lines drawn over the contour plot. Below is $B_r(z)$ and B_z from the horizontal line seen on the contour plot. Note the scale differences between the B_r and B_θ or B_z data.

5 cm for both the ideal and resistive mode. These plasmas were produced with the central 7 guns arced and biased for which $q_{r=5}$ approximates q_a. Mode onset occurs when $q_{r=2} \approx 1.1$ or $q_0 \approx 1$. Recall that the individual gun profiles are peaked which forces $q_0 < q_{r=2cm}$. At mode onset $q_{r=5cm}$ is above 1 for both the ideal and resistive modes. Were these external kinks, one would expect $q_{r=5cm} = 1$ at mode onset. The same result is observed in no wall plasmas. In Fig. 5.7 the resistive and ideal modes are strikingly similar in terms of onset and relative strength when $\tau_w = .5$ ms or 7 ms. The main difference of absolute mode amplitude is simply attributable to the wall time: a longer τ_w translates to a smaller B_r.

The growth of the high frequency mode has no relation to the wall time. In Fig. 5.8 the growth of the ideal mode is shown for plasmas with both types of conducting walls. No attempt to fit the mode growth to a $e^{\overline{\gamma}(t)^{3/2}}$ dependent model, as in Section 4.4, is made. Here the growth is

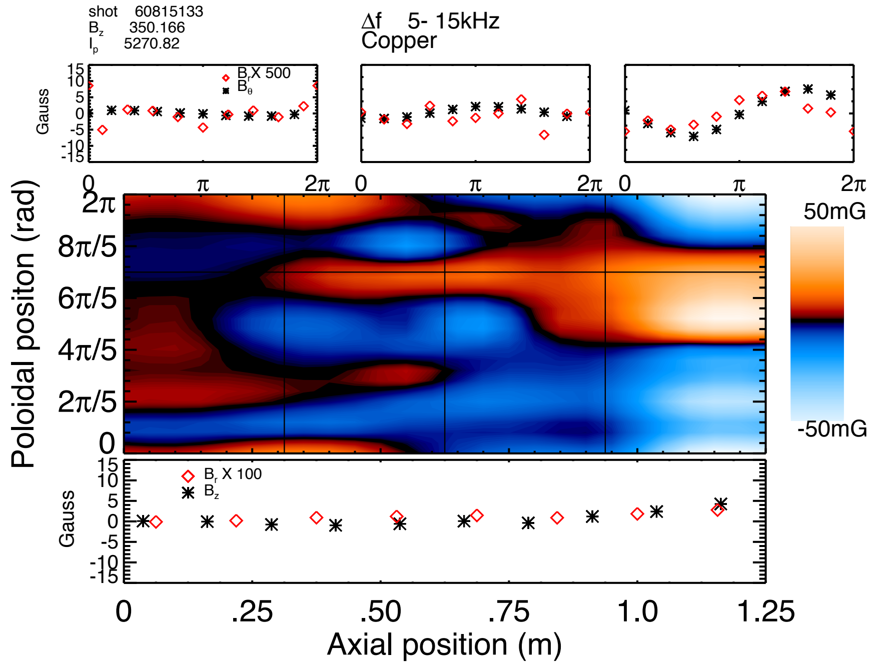

Figure 5.6 The reconstructed eigenmode of the low frequency mode. This mode is localized to the anode end of the machine. The band path filter is from 5 to 15 kHz. Plotted above and below the contour plot are subplots of B_r, B_θ, and B_z as in Fig. 5.5. The mode is larger than the high frequency mode with a conducting boundary at the wall.

measured from the linear phase of the natural log of the mode amplitude. Measuring the growth in such a fashion fails to account for the subtle effects of an evolving current profile but does provide general insight into the time scale of the mode growth. Figure 5.8 demonstrates the uniformity of the growth rate with different τ_w and its better alignment to the Alfvèn time than the wall time.

5.3 Onset and Growth of the Resistive Wall Mode

A candidate for the RWM has been discovered in the ReWM. The detection was initially complicated by three effects: the continuous presence of internal modes discussed above, field errors associated with coil misalignments and magnet leads, and a skewness in the machine alignment. The field errors and skewness have been reduced but residual errors remain in the measurements.

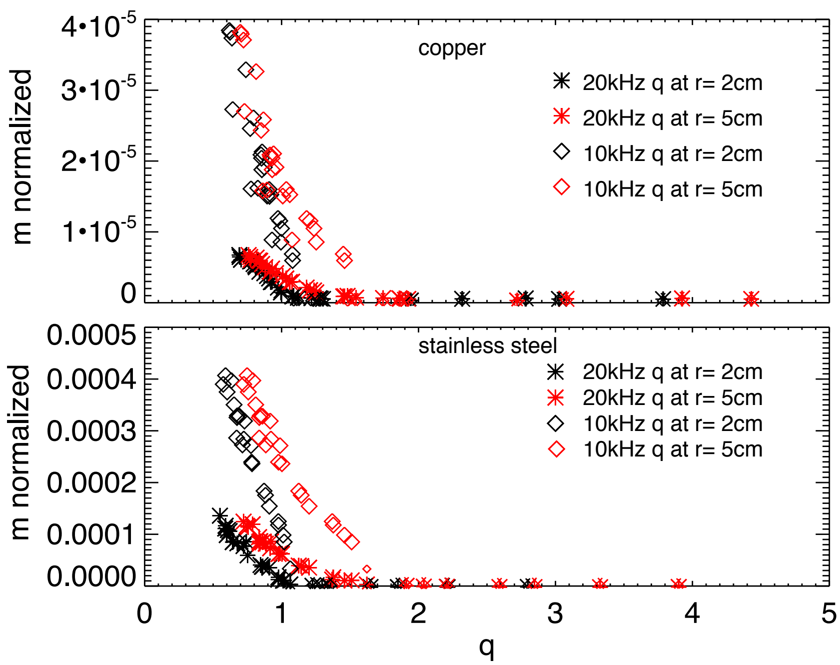

Figure 5.7 The amplitudes of the high and low frequency modes for copper and stainless steel boundary conditions at the wall. Mode amplitude is graphed in conjunction with two values for q, $q_{r=2cm}$, and $q_{r=5cm}$. For both boundary conditions mode onset occurs when $q_2 \approx 1$. Normalized mode amplitude = $\frac{B_r(mode)}{B_z(applied)}$

An example of a typical discharge with the RWM instability is shown in Fig. 5.9 where time histories of $m = 1$ and $m = 2$ signals are shown in (a). The growing amplitude of the $m = 1$ mode is the RWM, while the $m = 2$ mode is primarily an error field. The error field, with little axial structure, has a relatively fixed amplitude throughout the shot. The RWM grows with time and has a clear $m = 1$ signature, as seen in both panels in Fig. 5.10. For both Fig. 5.10 (a) and (b), the $m = 1$ character is seen in the dark and light islands (negative and positive polarization) on opposite sides of the machine at L = .6 m.

To find the onset condition, a series of discharges with increasing plasma current were used. The amplitude of the RWM was determined as the difference between the error field amplitude and the amplitude of the saturated mode (as shown in Fig. 5.11 (a)). Inspection of Fig. 5.11 reveals a linear dependence between the $m = 2$ error field and plasma current. The same dynamics are at play for the $m = 1$ error field; however, the $m = 1$ signal undergoes a transition around 3.5 kA. At

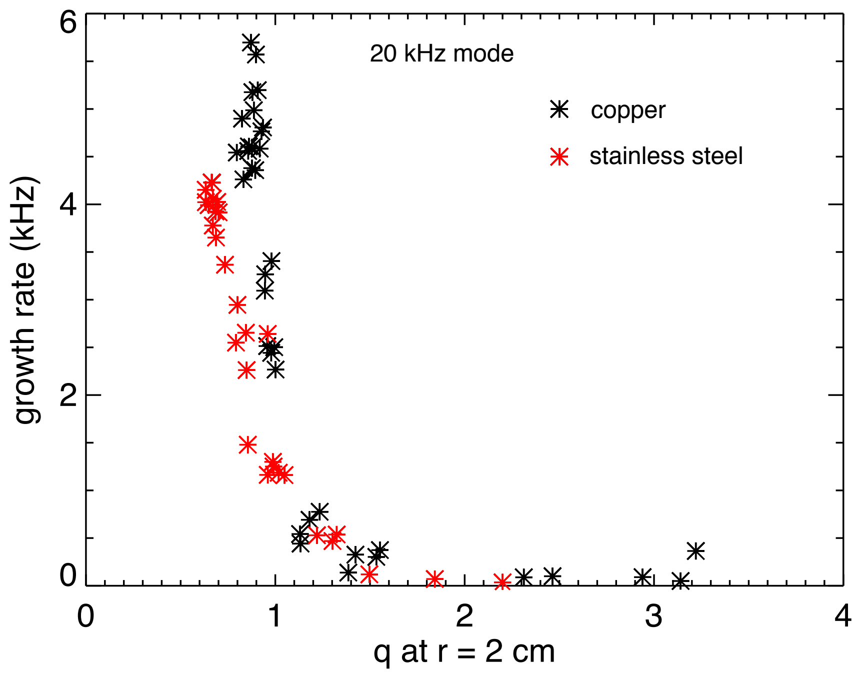

Figure 5.8 Growth of the high frequency mode with copper and stainless steel boundary conditions at the wall. The wall time has no effect on the growth of the mode.

this point the RWM is unstable and contributing to the mode amplitude. The error field amplitude is finite and linearly dependent on plasma current, while the RWM is only expected to be present for currents above some threshold condition. Knowing that the $m = 1$ signal at 5 kA contains both the RWM and an error field component linearly dependent on the plasma current allows one to subtract the error signal for analysis of the pure RWM information. In Fig. 5.11 (b) the amplitude of the RWM (error field subtracted out) is plotted against measurement of q at 2 cm and 5 cm. Again, for these plasma $q_a \approx q_{r=5cm}$. From Fig. 5.11 (b) it is apparent that the RWM is unstable when $q_{r=2cm} < 1$ or $q_{r=5cm} < 1.2$. Theoretically, the RWM should only be apparent when $q_a < 1$. This discrepancy will be discussed in Section 6.4.

To properly identify the RWM, the measured growth rate in conjunction with the wall time and q_a must be correlated to theoretical predictions. Strictly speaking Equation 5.1 is valid for a single wall only and must be modified to account for two distinct walls (and wall times) at different radii. Equation 2.37 recognizes two stationary walls with different wall times. For the 0.5 ms wall

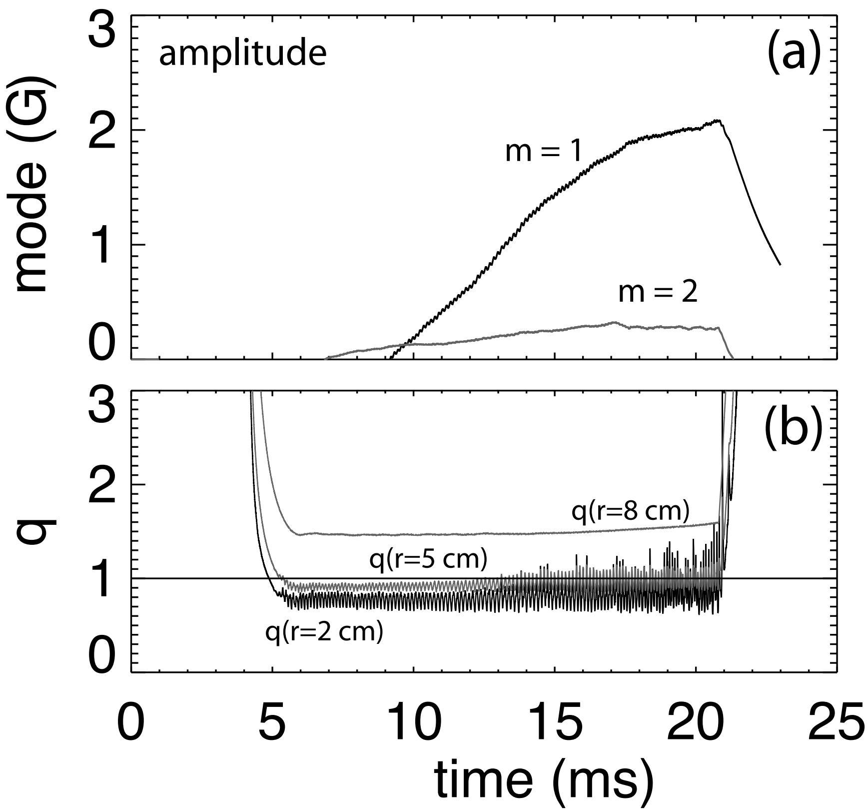

Figure 5.9 Typical resistive wall mode. In (a) the amplitudes of the both $m = 1$ and $m = 2$ modes as determined by a spectral analysis of the spatial variation in $B_r(\theta)$ at a fixed Z location (near the anode). For reference (b) shows the evolution of the q profile as monitored by the segmented anode (the plasma radius is approximately 6 cm).

Equation 5.1 is used to predict the growth rate, while Equation 2.37 predicts the growth for plasmas with the 7 ms wall.

The comparisons between experiment and theory for the growth of the mode in B_r are shown in Fig. 5.12. Prior to understanding the error field effects it was not possible to measure the growth in the stainless steel shell before mode saturation. Once the role of the error field became clear (on the 7 ms shell), the 0.5 ms shell could be revisited and the growth rate measured for a variety of plasma currents. The results, together with the prediction for the growth rate are plotted. In Fig. 5.12 three different values of a, the plasma radius, have been used in plotting projected growth rates. The agreement is very good (if not excellent): the wall time sets the growth rate, and the

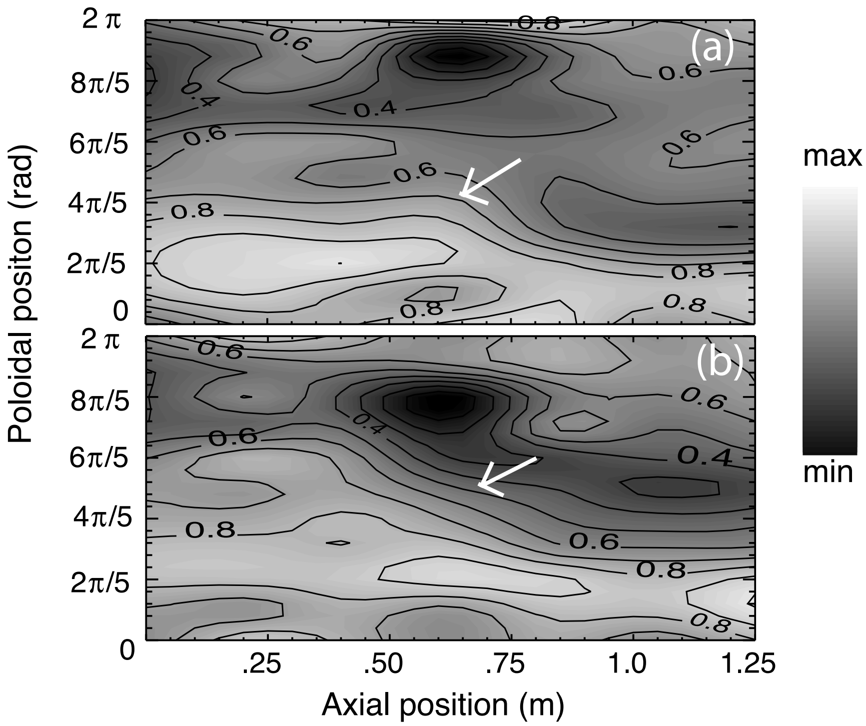

Figure 5.10 Normalized contour plots of B_r for the RWM. In (a) the RWM when $q_a \approx 0.8$. In (b) the RWM when $q_a \approx 0.6$. Note the $m = 1$ character in both plasmas as well as the dependence of the axial structure on q_a. A lower q_a translates into a tighter twist, seen with the highlighted (white arrows) contour lines, in the eigenmode of the RWM.

plasma becomes more unstable as q_a is driven lower. The growth rate of the RWM in B_p has been measured and found to match that of B_r, see Fig. 5.13. While not surprising, it is important to establish the observed mode as a global mode seen across different polarizations.

For both Fig. 5.12 and Fig. 5.13 the growth is plotted in relation to q at 2.3 cm and not 5 cm. The same growth rates are measured with $q_{r=5cm}$; however, mode onset would be seen to occur at a higher q ($q_a \approx 1.3$). There are known difficulties in accurately measuring q in the ReWM. This fact complicates determining the precise value of q at mode onset; however, it is important to stress that the growth of the mode largely matches predictions for a plasma with ReWM parameters. Further discussion on measuring q is found in Section 6.4.

The helical structure of the RWM eigenmode is present but not as clearly defined as the internal ideal mode. A helix is apparent and its dependence on q_a is seen by careful comparison of Fig. 5.10

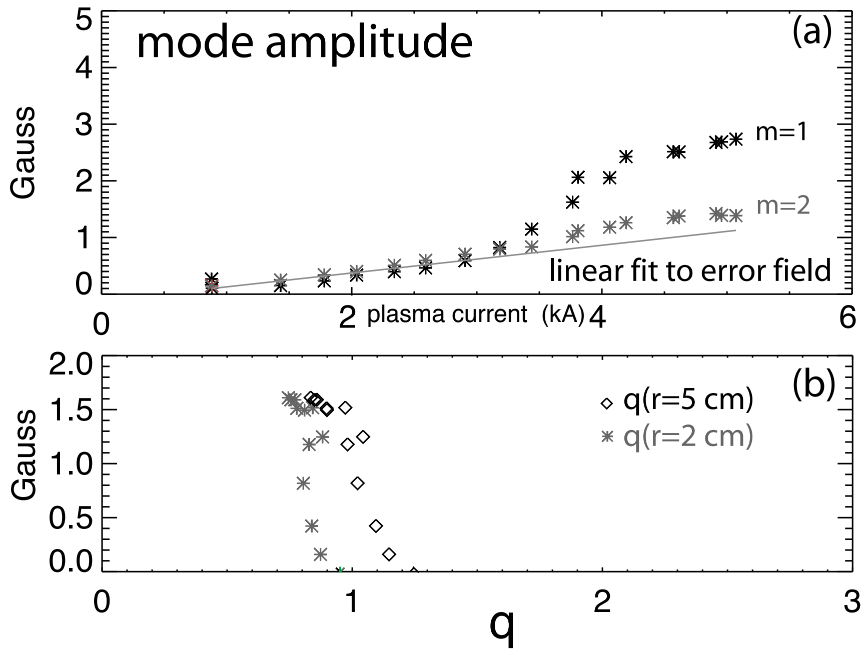

Figure 5.11 RWM dependence on plasma current. Top: (a) Saturation amplitudes for $m = 1$ and $m = 2$ modes at different plasma currents. (b) Difference between the amplitude of the $m = 1$ mode amplitude and the error field amplitude as determined from linear fit in (a) as a function of q, illustrating onset at q ≈1.

(a) where $q_a \approx 0.8$ and (b) where $q_a \approx 0.6$. Note the slope of the contouring lines (highlighted with the white arrow) between the lobes of the mode. In (a) they are largely linear, but twisted in (b). As predicted in Equation 2.22 and Fig. 4.13 the lower value of q_a corresponds to a tighter twist. The internal mode seen in Fig. 5.5 stands out far better because it can be isolated in frequency space and plotted with little error or noise. The same technique cannot be applied to the RWM as the error fields cannot be completely numerically decoupled from the RWM signature.

5.4 Interaction of Internal and External Modes

When performing experiments across a small range of mirror ratios ($.95 < R_m < 1.2$), it was unexpectedly found that the internal mode decreases and almost vanishes at higher mirror ratios. In plasmas where the internal mode is suppressed, the external mode growth does not saturate and reaches a larger amplitude. One can clearly see this effect in Fig. 5.14. The RWM in shot 70521130

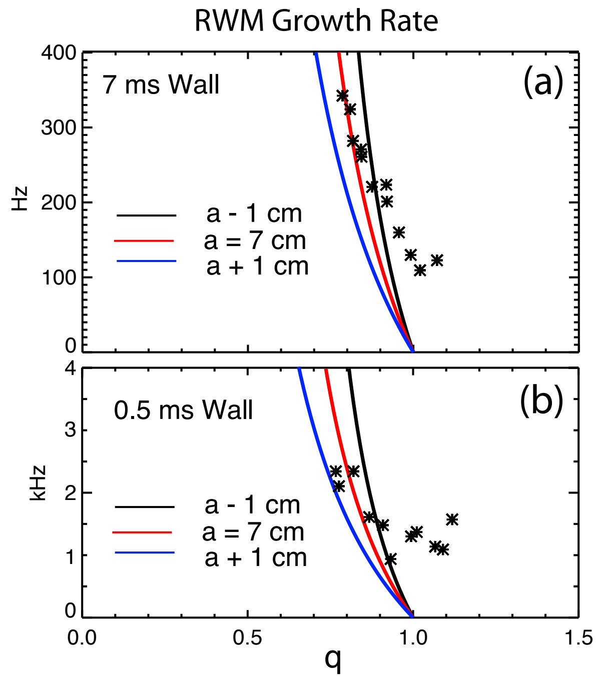

Figure 5.12 Growth rates for the observed RWM with different wall times, as measured from the growth rate of the $m = 1$ component of B_r using the flux loop array outside the conducting shells. The upper plot (a) is for the thick shell and the lower (b) is for the thin shell. Plotted as well in both cases are predicted growth rates for plasmas of different radii ($a = 7 \pm 1$ cm)

(hashed trace) does not saturate, while it does in shot 70405094 (solid trace). In the former, the internal mode is almost completely suppressed, as seen in Fig. 5.14 (b). An interesting occurrence between the internal and external kink can be seen within the dynamics of shot 70405094. The RWM saturation around 15 ms coincides with an increase in the internal mode as seen in Fig. 5.14 (b). It has been empirically observed that an excess of internal mode activity typically slows or stops the RWM growth. To summarize, with little or no internal mode, the external kink does not saturate. Note that the plasmas displayed in Fig. 5.14 have a closely matched q profile.

Figure 5.15 examines the amplitude of the external kink plotted against the amplitude of the internal kink for two different values of R_m. As the plasma current increases, when $R_m = 0.95$, the external kink saturates at 2 G while the amplitude of the internal kink continues to grow. The external kink saturates within 10 ms in these plasmas. Conversely, when $R_m = 1.04$ the internal

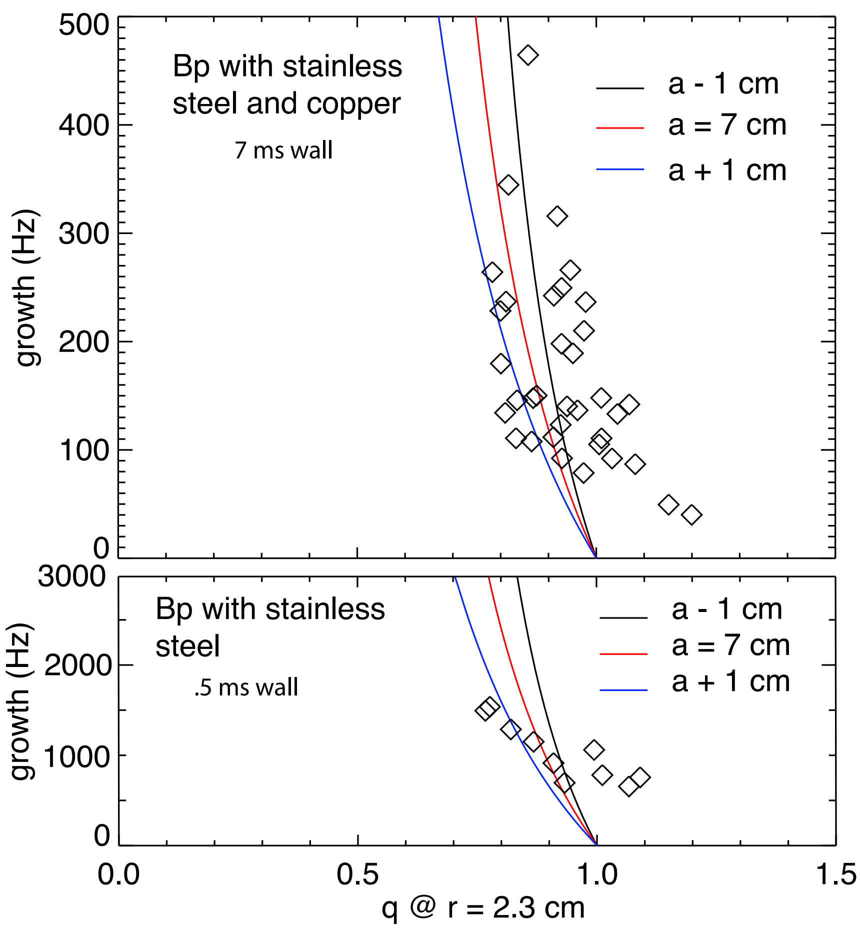

Figure 5.13 Growth rates for the observed RWM with stainless steel and copper wall, as measured from the growth rate of the $m = 1$ component of B_θ using the flux loop array inside the conducting shells. Plotted as well in both cases are predicted growth rates for plasmas of different radii ($a = 7 \pm 1$ cm).

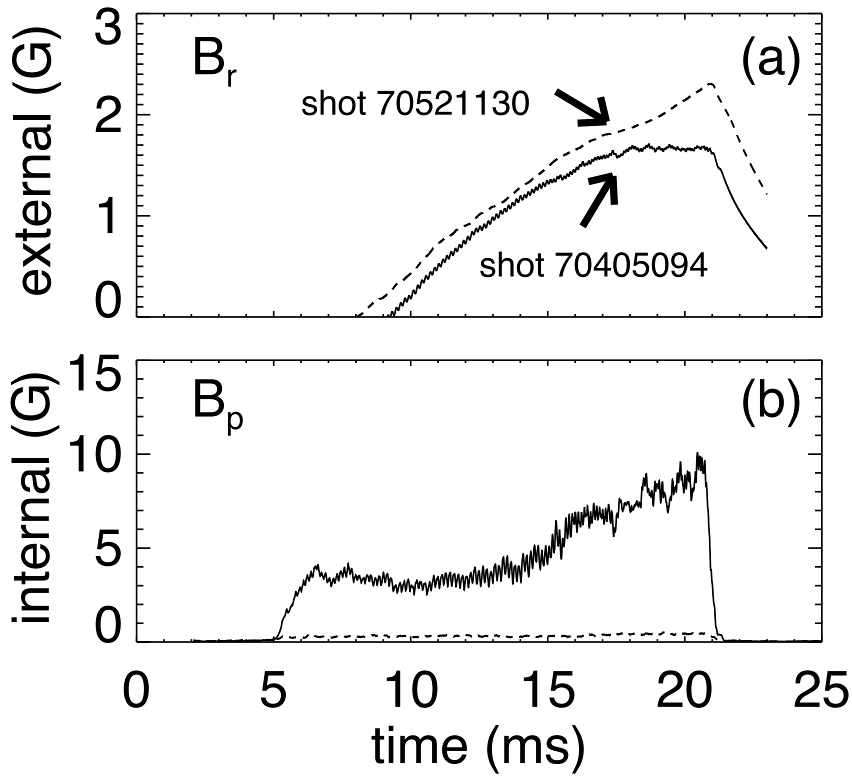

Figure 5.14 Interaction of the internal and external modes shown with two separate shots. In (a), the RWM from shot 70521130 (hashed line) does not saturate in comparison to the RWM in shot 70405094 (solid line). Below in (b), shot 70521130 has almost complete suppression of the internal kink while it is strongly present and growing in shot 70504094. For shot 70521130 q_2 = 0.4, q_5 = 0.6,q_8 = 1.0 and $R_m = 1.05$. For shot 70405094 q_2 = 0.6, q_5 = 0.7,q_8 = 1.0 and $R_m = .95$.

mode is essentially eliminated and the external mode continues to grow larger with increasing plasma current. The external kink only saturates in a few of the plasmas and only late in the shot. Thus, with a large internal kink the external kink quickly saturates, while without the internal kink the external kink grows throughout the shot.

The underlying physics of this phenomena are unknown. As both the internal and external kinks are current driven modes, the current profile itself is most likely responsible for the reported mode dynamics. In Fig. 5.16 the current and q profiles are plotted for plasmas with three different values of R_m. The value of q is determined by measuring the current at the anode and performing a Runge-Kunta integration of the field line. The plasma current sourced in each of the cases is the

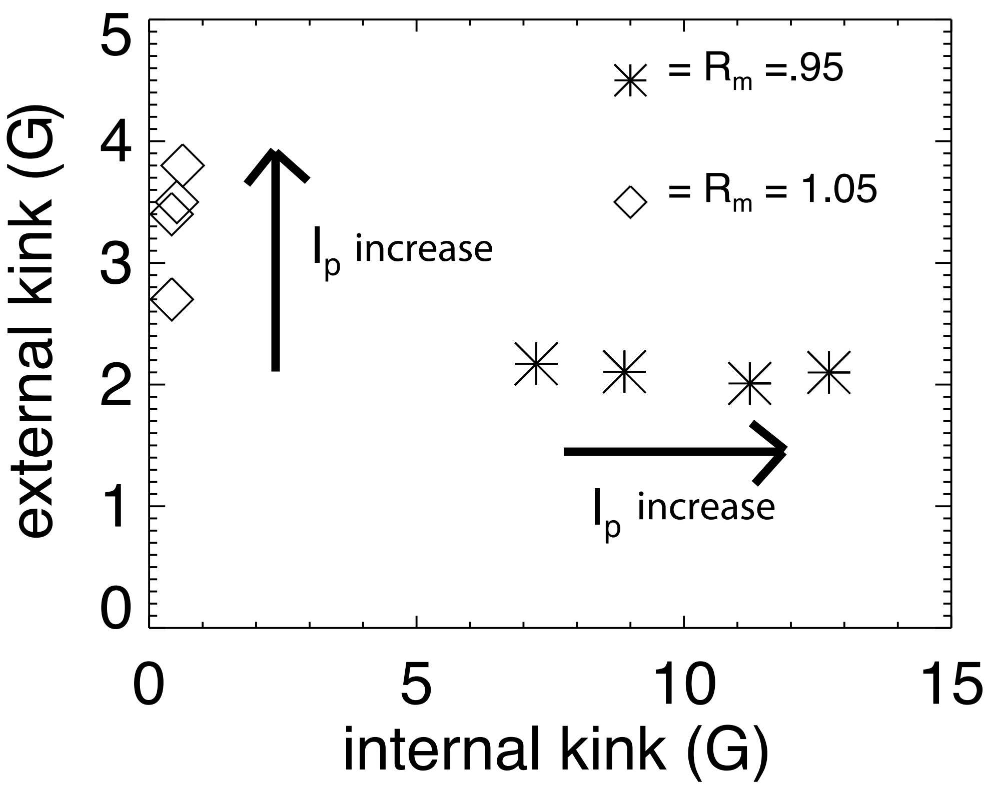

Figure 5.15 Two different series of shots highlighting the relationship between the internal and external kink. The plasma current associated with each data point, from left to right for $R_m = .95$ match those from the bottom to the top for $R_m = 1.05$. For $R_m = .95$ as I_p is increased, the external kink is saturated and only the internal kink increases in amplitude. The opposite is seen with $R_m = 1.05$. When the internal mode is almost quenched, the external mode amplitude increases with increasing I_p.

same and each gun itself is controlled uniformly relative to the other guns. The only variation in the three different cases is R_m. A cursory examination reveals more current, and correspondingly lower q, in the center of the plasma as R_m increases. Logically, as q lowers, the drive for the RWM increases. It is unclear though why this change in the profile would suppress the internal kink. This argument also fails to explain the data from shot 70405094 in Fig. 5.14 where R_m is not adjusted but changes in the RWM dynamics are coincident to changes in the internal kink dynamics. Unfortunately, numerical and analytical work performed thus far on line tied systems is unable to examine mode dynamics in association with different current profiles.

On a purely speculative note, suppression of the RWM in conjunction with strong internal mode activity has been reported in NSTX [62]. To the author's knowledge, this has not previously been reported in a cylindrical line tied geometry. Drawing parallel connections between these two machines is a stretch at best; however, the similar observations also offer an opportunity to explore the underlying unifying physics.

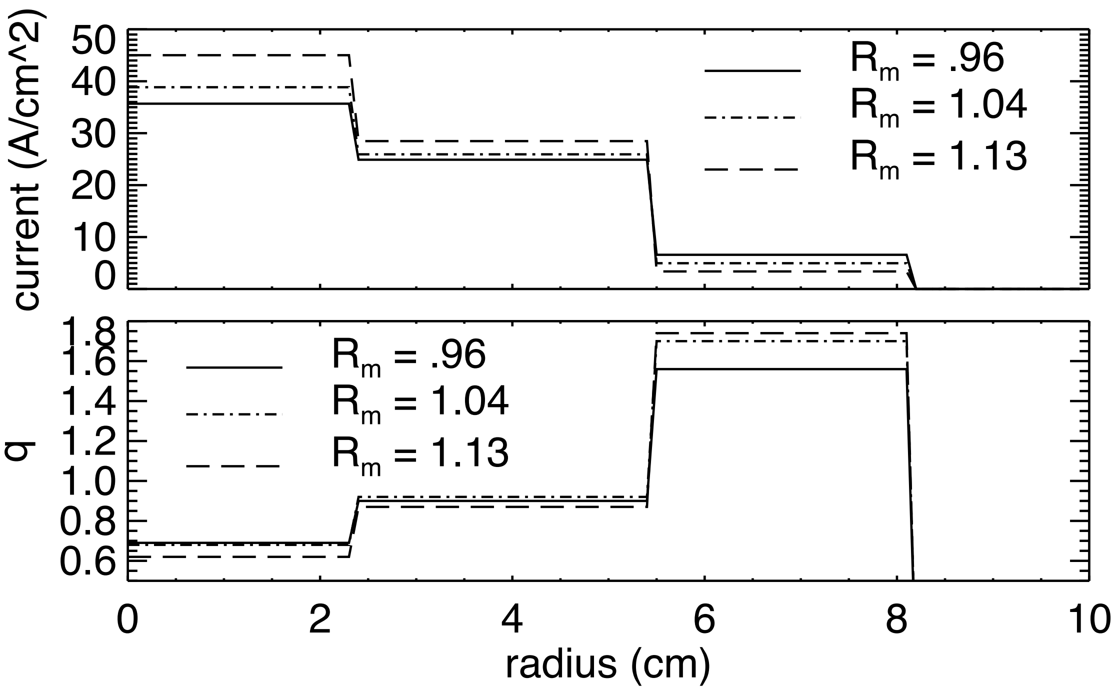

Figure 5.16 Above, the current density as measured by the segmented anode for three different values of R_m. Below, the corresponding values for q from these experiments. As R_m increases the current profile becomes more pitched.

Chapter 6

Conclusions

Line tied plasmas with different boundary conditions at the wall have been studied in the ReWM. Initial experiments focused on the no wall boundary condition while subsequent work examined plasmas with conducting walls. Studies with an insulating wall served to both confirm predictions of no wall stability theory in a line tied plasma as well as establish a baseline of plasma dynamics in the ReWM for future studies. In order to determine the role of the wall time in the MHD, two different wall materials with distinct wall times were used in experimental campaigns.

6.1 Observations

• Two modes, which are well separated in frequency and monochromatic, are observed in plasmas with a conducting or insulating wall at the boundary. Onset for both modes, with either boundary condition, occurs when $q < 1$ inside the plasma. For either mode the amplitude of the B_r eigenmode is essentially equal to zero when a conducting wall is present.

• The higher frequency mode has a growth rate of $e^{\gamma(t)^{3/2}}$, with $\gamma = 10.22 \times 10^3$ sec$^{-2/3}$, in plasmas without a conducting wall. The growth rate does not change dramatically when conducting walls are present. The eigenmode is peaked in the middle of the machine and tapers to zero towards the ends with clear $m = 1$, $n = 1$ characteristics. The mode rotates at a rate that is consistent with $E \times B$ rotation.

• The low frequency mode dominates the plasma when the current profile undergoes fast relaxation events. Conversely, when the current profile is quiescent, the high frequency mode is the principle mode. The eigenmode of the low frequency mode is substantially different from the high frequency mode. It is zero at the cathode end and peaked with a $m = 1$ structure at the anode end.

• Spontaneous relaxation dynamics in the current profile are observed in plasmas with or without a conducting wall at the boundary. These events flatten the q profile so that it approaches 1 everywhere in the plasma. The relaxations may be discrete or periodic; however, a periodic behavior is dominant when a conducting wall is present. The fast relaxations are only seen in the plasma when $q \approx 1$ and no other value of q.

• Experiments undertaken without a conducting wall demonstrate the stabilizing effect of non-current carrying plasma surrounding a current carrying plasma. With an outer layer of plasma, MHD fluctuations are reduced dramatically.

• With a conducting wall present, a mode is observed with a growth rate determined both by q and the wall time. Onset of the mode occurs when $q_0 = 1$ or $q_a \approx 1.2$. The eigenmode is clearly $m = 1$ and peaked in the middle of the machine. The mode has slight rotation, but is essentially locked in place.

• The addition of a magnetic material outside the composite stainless steel and copper walls produces a mode which begins to grow at 1.5 kHz when $q_a < 1.5$. Theoretical considerations and additional experimental observations of this mode are reported in Appendix C.

6.2 Interpretation of Observations

• The high and low frequency modes are considered to be internal modes. Onset of the modes is governed by $q < 1$ within the plasma and not $q_a < 1$, as theory predicts for an external kink. Additionally, the growth of the high frequency mode is not effected by the presence of conducting walls.

• The small measured amplitude of B_r for both internal modes is subject to two effects. Because the modes are rotating sufficiently quickly, the wall appears almost ideal. As such, $B_r \approx 0$, at the wall. A second effect concerns the electromagnetic skin depth of the conducting walls. For the high frequency mode ($\sim$ 20 kHz), each wall is roughly equal to the skin depth. Thus, what small signal there is for B_r is further reduced by measuring the amplitude outside of a conductor.

• The relaxation events in the current column and concurring dominance of the low frequency mode indicates reconnection may be present in the plasma. The gross alterations to the current profile are solely a result of plasma dynamics as the current source is static in time and fixed in place. Additionally, the lack of axial symmetry in the low frequency eigenmode can be attributed to reconnection in the plasma. With reconnection, field lines can originate at one r and θ at the cathode but terminate at a different r and θ at the anode.

• The stabilizing effect of plasma without current surrounding a current carrying plasma can be interpreted two ways. First, the extra plasma mimics a close fitting highly conductive wall, itself a stabilizing effect. Second, the extra plasma alters the current profile so that the external kink becomes an internal kink, unobservable outside the vacuum wall.

• The mode with a growth rate determined by wall time and q is the resistive wall mode. The mode fits predictions for the growth and structure of the RWM. Furthermore, the mode is global, observed in both B_r and B_θ, as expected for the RWM. That the mode is seen to destabilize when $q_{r=2cm} < 1$ or when $q_{r=5cm} =< 1.2$ and not explicitly when $q_a < 1$ as theory predicts is discussed in Section 6.4.

• The mode found in conjunction with a magnetic material present is thought to be the ferritic wall mode or FWM. Additional analysis of the FWM in relation to the ReWM is given in Appendix C.

6.3 Limitations of Ideal MHD

Before continuing it is important to stress the limitation of ideal MHD as it pertains to the plasmas in the ReWM. From table 6.1 it can be seen that the plasma is relatively cool, with the Lundquist number equal to 60. This strongly limits the applicability of the no wall results to coronal loops where $S \sim 10^{10}$. The resistive diffusion time in the ReWM is about .5 ms, which is also the time scale of the stainless steel wall. Differentiating these effects are problematic; however, testing the plasmas with a longer wall time and observing a change in the growth rate suggests the dominant effect is indeed the wall. Finally, ideal MHD is applicable in the limit where $r_{Li}/a \ll 1$. The plasma marginally meets this criteria, but the Hall, $\mathbf{J} \times \mathbf{B}$, and pressure, ∇p_e, terms may not

Plasma Parameters						
B_z	τ_A	S	β	r_{Li}	res.diff.time	a
300 G	10 μs	60	3%	2 cm	.6 ms	10 cm

Table 6.1 Plasma parameter values calculated with machine relevant conditions. For the calculations, $T_e \sim 10$ eV, $n_e \sim 1 \times 10^{19} m^{-3}$

be negligible in Ohm's law below

$$\mathbf{E} + \mathbf{v} \times \mathbf{B} = \frac{1}{en}(\mathbf{J} \times \mathbf{B} - \nabla p_e - \nabla \cdot \mathbf{\Pi_e} + \mathbf{R_e}) \tag{6.1}$$

No accounting has been made for any possible effects these terms may have upon either the internal or external kink conclusions presented herein. Furthermore, neither of these effects have been examined in a line tied geometry.

6.4 Missing Information in Calculating q

The imperfect agreement between theoretical and observed RWM onset may be partially explained by an improper measuring of q. Both of the techniques to measure q described in Section 3.6 assume that the amount of current within a particular radius is constant. Moreover, these calculations are based on the current profile as measured at the anode end. No accounting is made for the variations of current density along the plasma column. Figure 6.1 is an exaggeration of the current profile effects in the plasma. Measuring a current profile, as depicted in Fig. 6.1, at the anode while neglecting the tighter column at the cathode end incorrectly measures the value of q. Accounting for this effect would lower the value of q. The growth rates in Fig. 5.12 and Fig. 5.13 are expressed in relation to $q_{r=2cm}$ but an accurate measurement of the current profile would lower the q values and the onset would be closer to $q_{r=5cm} = 1$. The same argument applies to Fig. 5.11, where the RWM appears to have an onset related to either $q_{r=2cm} < 1$ or $q_{r=5cm} < 1.2$. A proper accounting of q would depress these measurements lower and the onset would be closer to $q_{r=5cm} = 1$. Future measurements of the current profile will attempt to quantify the axial variation and further refine the measurement of q.

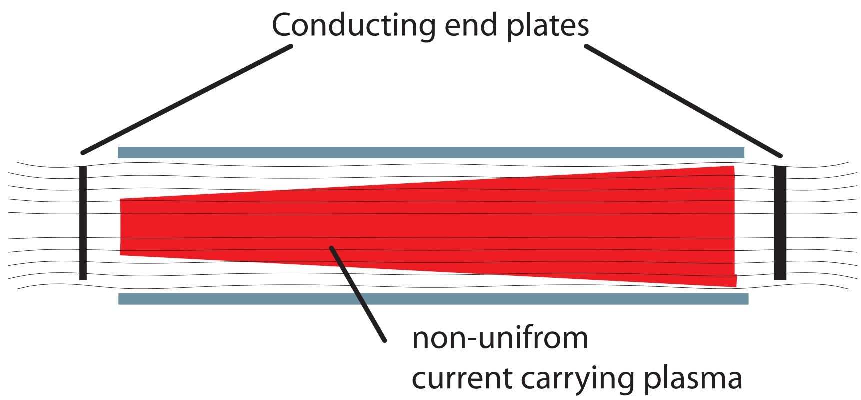

Figure 6.1 An exaggeration of the cross field diffusion present in the ReWM as the current goes from the cathode to the anode. The flaring current profile impedes the ability to clearly measure q.

6.5 Assessment of Agreement with External Kink Theory

The imperfect agreement between theoretical and experimental RWM onset may also stem from differences between the ReWM and the theory used in the predictions. The theory used to derive Equation 2.36 and Equation 2.37 assumes a uniform current and plasma density inside a and a vacuum region for $a < r < b$. In fact, the experimental density and current profile has an axial dependence, a result of finite cross-field diffusion. Additionally, a finite temperature, low density plasma exists in the device in the region $a < r < b$. This outer cool plasma complicates the determination of a and may contribute to bulk resistivity. Plasma resistivity itself is discussed further in Section 6.5.3 Any of these effects, non-trivial current or density profile, resistivity, or surrounding cool plasma, could modify the RWM onset.

The degree to which the plasma in the ReWM deviates from the constraints used in modeling the kink is an open question. In addition to the flat current profile assumption stated above, the theoretical model for the ReWM also assumes perfect line tying and no resistivity in the plasma. Considerations of experimental realities such as the presence of a sheath at the anode, axial plasma bulk flow, and plasma resistivity on the external kink are greatly illuminated by the phenomenological discussions and calculations in Reference [54]. These topics are discussed in Sections 6.5.1, 6.5.2, and 6.5.3.

6.5.1 Line Tying

An ongoing question concerning the ReWM has been the degree to which line tying assumptions are appropriate. Partially this stems from the difficultly in measuring ξ, the displacement vector and core feature of line tying theory. From a predicted ideal plasma model, ξ and in turn B_r can be calculated. As shown previously, the predicted and measured structures of the eigenmodes are in agreement.

Observation of RWM onset indicates that the line tying assumptions are sound. Ryutov claims that the presence of a sheath at the anode would half the critical current necessary for an external kink. In terms of q, this would result in $q_a = 2$, not the typical KS result of $q_a = 1$. The no wall kink discussed in Chapter 4 and RWM reported in Section 5.3 are both seen to have onset criteria related to $q = 1$ not $q = 2$. That the plasmas described in this thesis are unstable near $q = 1$ suggests that the anode in this machine does not have a pronounced sheath and that the line tying assumptions utilized are appropriate.

6.5.2 Plasma Flow

Recall that the plasmas are produced from an array of electrostactic guns which inject plasma into a vacuum. The injection most likely produces a flow which may effect the onset of the external kink. Taking into account axial bulk flow in the plasma would alter the critical current to

$$I_{crit} = I_{KS}\sqrt{1 - M^2} \tag{6.2}$$

where KS is the Kruskal and Shafranov limit and M is the Alfvén Mach number v/v_a. Despite not having Mach measurements in the plasma, one can assume an upper limit on the effect as the plasmas are not seen to become unstable above $q_a \approx 1.2$. If the mode onset at $q_a = 1.2$ were wholly attributed to the bulk flow, $M = .4$. Interestingly, if the plasma has a flow equal to the sound speed, not an unreasonable assumption considering the plasma is expanding into a vacuum, $M \approx .42$. It is entirely possible that the relaxed onset observed for the RWM is attributed to the plasma having a component of axial flow associated with it.

6.5.3 Resistivity

This relaxation on the stability threshold could also be influenced by resistivity in the bulk plasma. While offering more discussion than calculations on the matter, Ryutov suggests that the effect could be a replacement of a hard instability limit with one more gradual where relatively low currents could produce an instability. Stepping back though, Fig. 5.11 does indeed suggest a hard stability limit, though one that may be slightly above $q_a = 1$. Work by Finn $et.al.$ on internal modes in line tied systems also points to a lowering of the critical current (raising of q_a) when allowing resistive effects in the plasma [11]. The applicability of this result with internal modes to the external RWM is not known at this time.

6.6 Open Questions and Future Directions

In determining that the ideal and resistive modes are internal modes through both the onset and growth, a problem is presented. Strictly speaking internal modes are not observable outside of the plasma. The general model of plasma dynamics predicts that the signature of the kink, a B_r signal, would be shielded by the plasma when originating from an internal mode. The question at hand is how these modes can be labeled internal yet be observable outside of the plasma. That walls with distinct values of τ_w produce no differences in either the growth or onset of these modes does indeed indicate that these are internal modes.

One theory proposed concerning the high frequency internal mode in the ReWM is that while the mode onset is related to $q_0 = 1$, the mode grows outward following the $q = 1$ surface as the current increases. This produces an internal kink growing and saturating into an external kink. Interestingly, the mode's high rotation (≈ 20 kHz) would cause the resistive wall to appear ideal and stabilizing. That these high frequency modes do not suddenly stabilize when they reach a particular rotation rate again indicates that these are internal modes, unaware of the boundary condition at the wall. The paradox of clearly measuring an internal mode outside of the plasma is not well understood at this point. Further confounding is the degree to which the ideal internal eigenmode matches predictions of the external eigenmode. Resolution of this last point may reside in the twisted nature of both internal and external kinks.

Also not understood at this juncture of the project is any interdependence between the external RWM and internal modes. Data and observations have been presented which indicate strong internal mode activity interferes with the RWM. This coincides with observations on NSTX. Again though, the physical mechanism of such an interaction is unknown.

A linear line tied screw pinch has been experimented upon with and without conducting walls at the boundary. Internal modes are present in either geometry when $q_0 < 1$. With a conducting wall the RWM is observed with a growth rate dependent on the wall time. The onset of the RWM is slightly higher than expected but may be attributed to bulk flow in the plasma or an improper measurement of q. Future studies include a better measurement of q and flow velocity in the plasma to elucidate the onset criteria of the RWM. Thus far, little effort has been undertaken to model the plasma in the ReWM with numerical simulation. A fuller understanding of plasma behavior and mode dynamics would certainly result from such a study. The ReWM is ready to explore the ability to passively stabilize the RWM with a double shell configuration in which the outer conductor is spun.

LIST OF REFERENCES

[1] T. E. Allibone, D. R. Chick, G. P. Thomson, and A. A. Ware. *Review of Controlled Thermonuclear Research at A. E. I. Research Laboratory*, volume 32. United Nations, Geneva, 1958.

[2] R. Aymar, C. Etievant, P. Hubert, A. Samain, B. Taquet, and A. Torossian. *Experimental Studies of the Pinch Phenomenon*, volume 32. United Nations, Geneva, 1958.

[3] D. A. Baker, G. A. Sawyer, and T. F. Stratton. *Low Voltage-Gradient Pinches in Metal-Walled Systems*, volume 32. United Nations, Geneva, 1958.

[4] P.R. Brunsell, D. Yadikin, D. Gregoratto, R. Paccagnella, T. Bolzonello, M. Cavinato, M. Cecconello, J.R. Drake, *et al.* Feedback stabilization of multiple resistive wall modes. *Phys. Rev. Lett.*, 93:"225001", 2004.

[5] L. C. Burkhardt and R. H. Lovberg. *Field Configurations and Linear Discharge Stability*, volume 32. United Nations, Geneva, 1958.

[6] E. P. Butt, R. Carruthers, J. T. D. Mitchell, R. S. Pease, P. C. Thonemann, M. A. Bird, J. Blears, and E. R. hartill. *The Design and Performance of ZETA*, volume 32. United Nations, Geneva, 1958.

[7] J. D. Callen, C. C. Hegna, B. W. Rice, E. J. Strait, and A. D. Turnbull. Growth of ideal magnetohydrodynamic modes driven slowly through their instability threshold: Application to disruption precursors. *Phys. Plasmas*, 6:2963, 1999.

[8] C. Cates, M. Shilov, M. E. Mauel, G. A. Navratil, D. Maurer, S. Mukherjee, D. Nadle, J. Bialek, *et al.* Suppression of resistive wall instabilities with distributed, independently controlled, active feedback coils. *Phys. Plasmas*, 7:3133, 2000.

[9] S. A. Colgate, J. P. Ferguson, and H. P. Furth. *A Toroidal Stabilized Pinch*, volume 32. United Nations, Geneva, 1958.

[10] G. L. Delzanno, E. G. Evstatiev, and J. M. Finn. Resistive effects on line-tied magnetohydrodynamic modes in cylindrical geometry. *Phys. Plasmas*, 14:092901, 2007.

[11] G. L. Delzanno, E. G. Evstatiev, and J. M. Finn. The role of resistivity on line-tied kink modes in cylindrical geometry. *Phys. Plasmas*, 14:070702, 2007.

[12] G. G. Dolgov-Saveliev, D. P. Ivanov, V. S. Mukhovatov, K. A. Razumova, V. S. Strelkov, M. N. Shepelyev, and N. A. Yavlinsky. *Investigations of the Stability and Heating of Plasmas in Toroidal Chambers*, volume 32. United Nations, Geneva, 1958.

[13] G. Einaudi and G. Van Hoven. Stability of a diffuse linear pinch with axial boundaries. *Phys. Fluids*, 24:1092, 1980.

[14] G. Fiksel, A.F. Almagri, D. Craig, M. Iida, S. C. Prager, and J.S. Sarff. High current electron emitter. *Plasma Sources Sci. Techn.*, 5:78, 1996.

[15] J. P. Freidberg. *Ideal Magnetohydrodynamics*. Plenum, 1993.

[16] J. P. Freidberg and R. Betti. Stabilization of the resistive wall mode by differentially rotating walls. *Phys. Plasmas*, 8:383, 2001.

[17] I. Furno, T. P. Intrator, E. W. Hernsing, S. C. Hsu, and S. Abbate. Coalescence of two magnetic flux ropes via collisional magnetic reconnection. *Phys. Plasmas*, 12:055702, 2005.

[18] I. Furno, T. P. Intrator, G. Lapenta, L. Dorf, and S. Abbate. Effects of boundary conditions and flow on the kink instability in a cylindrical plasma column. *Phys. Plasmas*, 14:022103, 2007.

[19] I. Furno, D. D. Ryutov, S. Abbate, T. Madziwa-Nussinov, A. Light, L. Dorf, and G. Lapenta. Current-driven rotating-kink mode in a plasma column with a non-line-tied free end. *Phys. Rev. Lett.*, 97:015002, 2006.

[20] A. M. Garofalo, E. J. Strait, L. C. Johnson, R. J. La Haye, E. A. Lazarus, G. A. Navratil, M. okabayashi, J. T. Scoville, *et al.* Sustained stabilization of the resistive-wall mode by plasma rotation in the diii-d tokamak. *Phys. Rev. Lett.*, 89:235001, 2002.

[21] A. M. Garofalo, A. D. Turnbull, M. E. Austin, J. Bialek, M. S. Chu, K. J. Comer, E. D. Fredrickson, R. J. Groebner, *et al.* Direct observation of the resisitive wall mode in a tokamak and its interaction with plasma rotation. *Phys. Rev. Lett.*, 82:3811, 1999.

[22] A.M. Garofalo, A.D. Turnbull, E.J. Strait, M.E. Austin, J. Bialek, M.S. Chu, E. Fredrickson, R.J. LaHaye, *et al.* Stabilization of the external kink and control of the resistive wall mode in tokamaks. *Phys. Plasmas*, 6:1893, 1999.

[23] C. G. Gimblett and R. J. Hastie. A rotating shell and stabilization of the tokamak resistive wall mode. *Phys. Plasmas*, 7:5007, 2000.

[24] C.G. Gimblett. Stabilization of thin shell modes by a rotating secondary wall. *Plasma Phys. Controlled Fusion*, 31:2183, 1989.

[25] I. N. Golovin, D. P. Ivanov, V. D. Kirillov, D. P. Petrov, K. A. Razumova, and N. A. Yavlinsky. *Stable Plasma Column in a Longitudinal Magnetic Field*, volume 32. United Nations, Geneva, 1958.

[26] M. P. Gryaznevich, C. G. Gimblett, T. C. Hender, D. F. Howell, S. Pinches, R. J. La Haye, Y. Q. lie, and A. Bondeson. *Bull. Am. Phys. Soc.*, 48:307, 2003.

[27] A. B. Hassam. Tearing modes in solar coronal loops. *Astrophys. J.*, 348:778, 1990.

[28] C.C. Hegna. Stabilization of line tied resistive wall kink modes with rotating walls. *Phys. Plasmas*, 11:4230, 2004.

[29] A. W. Hood and E. R. Priest. Kink instability of solar coronal loops as the cause of solar flares. *Solar Physics*, 64:303, 1979.

[30] Yi-Min Huang, Ellen G. Zweibel, and Carl R. Sovinec. m = 1 ideal internal kink modes in a line-tied screw pinch. *Phys. Plasmas*, 13:092102, 2006.

[31] T.H. Ivers, E. Eisner, A. Garofalo, R. Kombargi, M.E. Mauel, D. Maurer, D. Nadle, G.A. Navratil, *et al.* Observation of wall stabilization and active control of low-n magnetohydrodynamic instabilities in a tokamak. *Phys. Plasmas*, 3:1926, 1996.

[32] R. Kaita, R. Majeski, T. Gray, H. Kugel, D. Mansfield, J. Spaleta, J. Timberlake, L. Zakharov, *et al.* Low recycling and high power density handling physics in the current drive experiment-upgrade with lithium plasma-facing components. *Phys. Plasmas*, 14:056111, 2007.

[33] A. J. Klein, D. A. Maurer, T. S. Pedersen, M. E. Mauel, G. A. Navratil, C. Cates, M. Shilov, Y. Liu, *et al.* Suppression of rotating external kink instabilities using optimized mode control feedback. *Phys. Plasmas*, 12:040703, 2005.

[34] M.D. Kruskal and M. Schwarzschild. Some instabilities of a completely ionized plasma. *Proc. R. Soc. London A*, 223:348, 1954.

[35] G. Kurita, T. Tuda, M. Azumi, S. Ishida, S. Takeji, A. Sakasai, M. Matsukawa, T. Ozeki, *et al.* Ferromagnetic and resistive wall effects on the beta limit in a tokamak. *Nuclear Fusion*, 43:949, 2003.

[36] I.M. Lanskii and A.I. Shchetnikov. Kink instability of plasma column with frozen-in ends. *Sov. J. Plasma Phys.*, 16:322, 1990.

[37] R. Lionello, Z. Mikic, J. A. Linker, and T. Amari. Magnetic field topology in prominences. *The Astrophysical Journal*, 581:718, 2002.

[38] R. Lionello, M. Velli, G. Einaudi, and Z. Mikic. Nonlinear magnetohydrodynamic evolution of line-tied coronal loops. *Astrophys. J.*, 494:840, 1998.

[39] B. C. Low and M. A. Berger. A morphological study of helical coronal magnetic structures. *The Astrophysical Journal*, 589:644, 2003.

[40] J. W. Mather and A. H. Williams. *Neutron Production in Columbus II*, volume 32. United Nations, Geneva, 1958.

[41] M. E. Mauel, J. Bialek, A. Boozer, C. Cates, R. James, O. Katsuro-Hopkins, A. Klein, Y. Liu, *et al.* Dynamics and control of resistive wall modes with magnetic feedback control coils: experiment and theory. *Nuclear Fusion*, 45:285, 2005.

[42] V. V. Mirnov, C. B. Forest, and C.C.Hegna. Role of external background plasma and non-mhd effects for kink stability of line tied screw pinch. *Bull. Am. Phys. Soc.*, 49:231, 2004.

[43] V. V. Mirnov, C. B. Forest, and C.C.Hegna. Internal current-driven kink modes in line tied screw pinch. *Bull. Am. Phys. Soc.*, 50:238, 2005.

[44] Y. Mok and G. Van Hoven. Resistive magnetic tearing in a finite length pinch. *Phys. Fluids*, 25:636, 1982.

[45] W. A. Newcomb. *Ann. Phys.*, 10:232, 1960.

[46] R. Paccagnella, S. Ortolani, P. Zanca, A. Alfier, T. Bolzonella, L. Marrelli, M.E. Puiatti, G. Serianni, *et al.* Active-feedback control of the magnetic boundary for magnetohydrodynamic stabilization of a fusion plasma. *Phys. Rev. Lett.*, 97:"075001", 2006.

[47] M. A. Raadu. Suppression of the kink instability for magnetic flux ropes in the chromosphere. *Solar Phys.*, 22:425, 1972.

[48] H. L. Rappaport. Coupling of the resistive wall mode to liquid wall surface modes. *Phys. Plasmas*, 8:3620, 2001.

[49] H. Reimerdes, A.M. Garofalo, G.L. Jackson, M. Okabayashi, E.J. Strait, M.S. Chu, Y. In, R.J. La Haye, *et al.* Reduced critical rotation for resistive wall mode stabilization in a near-axisymmetric configuration. *Phys. Rev. Lett.*, 98:"055001", 2007.

[50] H. Reimerdes, T. C. Hender, S. A. sabbagh, J. M. Bialek, M. S. Chu, A. M Garofalo, M. P. Gryaznevich, D. F. Howell, *et al.* Cross-machine comparison of resonant field amplification and resistive wall mode stabilization by plasma rotation. *Phys. Plasmas*, 13:056107, 2006.

[51] M. N. Rosenbluth. *Stability and Heating in the Pinch Effect*, volume 31. United Nations, Geneva, 1958.

[52] M. N. Rosenbluth, R. Y. Dagazian, and P. H. Rutherford. Nonlinear propertied of the internal m = 1 kink instability in the cylindrical tokamak. *Phys. Fluids*, 16:1894, 1973.

[53] D. D. Ryutov, R. H. Cohen, and L. D. Pearlstein. Stability of a finite-length screw pinch revisited. *Phys. Plasmas*, 11:4740, 2004.

[54] D.D. Ryutov, T.P. Intrator, S. Abbate, and T. Madziwa-Nussinov. Phenomenological theory of the kink instability in a slender plasma column. *Phys. Plasmas*, 13:032105, 2006.

[55] S. A. Sabbagh, R. E. Bell, M. G. Bell, J. Bialek, A. H. Glasser, B. LeBlanc, J. E. Menard, F. Paoletti, *et al.* Beta-limiting instabilities and global mode stabilization in the national spherical torus experiment. *Phys. Plasmas*, 9:2085, 2002.

[56] S. A. Sabbagh, J. M. Bialek, R. E. Bell, A. H. Glasser, B. P. LeBlanc, J. E. Menard, F. Paoletti, M. G. Bell, *et al.* The resistive wall mode and feedback control physics design in nstx. *Nuclear Fusion*, 44:560, 2004.

[57] S. A. Sabbagh, A. C. Sontag, J. M. Bialek, D. A. Gates, A. H. Glasser, J. E. Menard, W. Zhu, M. G. Bell, *et al.* Resistive wall stabilized operation in rotating high beta nstx plasmas. *Nuclear Fusion*, 46:635, 2006.

[58] S.A. Sabbagh, R.E. Bell, J.E. Menard, D.A. Gates, A.C. Sontag, J.M. Bialek, B.P. LeBlanc, F.M. Levinton, *et al.* Active stabilization of the resistive wall mode in high-beta, low rotation plasmas. *Phys. Rev. Lett.*, 97:"045004", 2006.

[59] V.D. Shafranov. *At. Energy*, 5:38, 1956.

[60] M. Shilov, C. Cates, R. James, A. Klein, O. Katsuro-Hopkins, Y. Liu, M. E. Mauel, G. A. Navratil, *et al.* Dynamical plasma response of resistive wall modes to changing external magnetic perturbations. *Phys. Plasmas*, 11:2573, 2004.

[61] A. C. Sontag, S. A. Sabbagh, W. Zhu, J. M. Bialek, D. A. Gates, A. H. Glasser, R. E. Bell, B. P. LeBlanc, *et al.* Resistive wall mode stabilization on high-β plasmas in the national spherical torus experiment. *Phys. Plasmas*, 12:056112, 2005.

[62] A. C. Sontag, S. A. Sabbagh, W. Zhu, J. E. Menard, R. E. Bell, J. M. Bialek, M. G. Bell, D. A. Gates, *et al.* Investigation of resistive wall mode stabilization physics in high-beta plasmas using applied non-axisymmetric fields in nstx. *Nuc. Fusion*, 47:1005, 2007.

[63] C.R. Sovinec, J.M. Finn, and D. del Castillo-Negrete. Formation and sustainment of electrostatically driven spheromaks in the resistive magnetohydrodynamic model. *Phys. Plasmas*, 8:475, 2001.

[64] E. J. Strait, A. D. Turnbull, J. R. Ferron, L. L. Lao, B. Rice, O. Sauter, S. J. Thompson, and D. Wroblewskii. Wall stabilization of high beta tokamak discharges in diii-d. *Phys. Rev. Lett.*, 74:2483, 1995.

[65] H. Takamaru and T. Sato. Intermittent self-organization: Nonlinear responses of twisting multiple flux tubes. *Phys. Plasmas*, 4:2845, 1997.

[66] J. L. Tuck. *Review of Controlled Thermonuclear Research at Los Alamos for mid 1958*, volume 32. United Nations, Geneva, 1958.

[67] M. V. Umansky, R. Betti, and J. P. freidberg. Stabilization of the resistive wall mode by flowing metal walls. *Phys. Plasmas*, 8:4427, 2001.

[68] M. Velli, G. Einaudi, and A. W. Hood. Boundary effects on the magnetohydrodynamic stability of a resistive plasma. *Astrophys. J.*, 350:419, 1990.

[69] M. Velli and A. W. Hood. Resistive tearing in line-tied magnetic fields: slab geometry. *Solar phys.*, 119:107, 1989.

Appendix A: Pulse Width Modulation for Plasma Current

Experimental plasma physics relies heavily on high power pulsed waveforms for heating the plasma, powering diagnostic beams, or providing control over a magnetic field produced by electromagnetic coils. Analog designs can satisfactorily offer a robust, precise, and economic solution to pulsed power needs; however, limitations of material or expertise can present severe impediments. Facing such barriers digital applications may offer equally elegant solutions with a better fit towards material supplies and personal expertise. Pulse Width Modulation (PWM) systems are more digital then analog and suitable towards either pulsed or continuous applications. However, PWM systems are typically dependent on four solid state switches in the H-bridge. While these switches are modestly priced for low current or slow switching applications, their cost increases substantially with faster switching and higher current applications. When individual switches approach $\$10000$, quadrupling the cost to built a PWM system may be unfeasible for many laboratories.

A modified PWM system has been developed which utilizes one solid state switch and a trio of capacitor banks working in conjunction to deliver a high current pulse able to match an external control waveform. Control of the current in the circuit to within 3% is achieved for modified flat top profiles. Experimental studies in the ReWM require a high power circuit which can emulate a master waveform with a gentle ramp-up from 70% of the target value to the final value in 3-4 ms, followed by a precise flat top for up to 20 ms. It is critical that the rate of the ramp-up and maximum current be adjustable on a shot by shot basis. An arbitrary waveform generator would certainly be able to produce such master waveforms; however, its cost may outweigh the advantages. Due to experimental concerns, the laboratory needs seven such circuits, able to function independently in parallel. Finally, circuit control and precision are paramount because the current is passing through a plasma upon which basic plasma studies of current driven instabilities are undertaken.

As this is a direct current circuit without complicated waveform restrictions, the typical PWM system with an H-bridge could be modified to use just one switch with multiple supply voltages. A high voltage supply initiates a fast ramp to 70% of the target current. A secondary supply provides

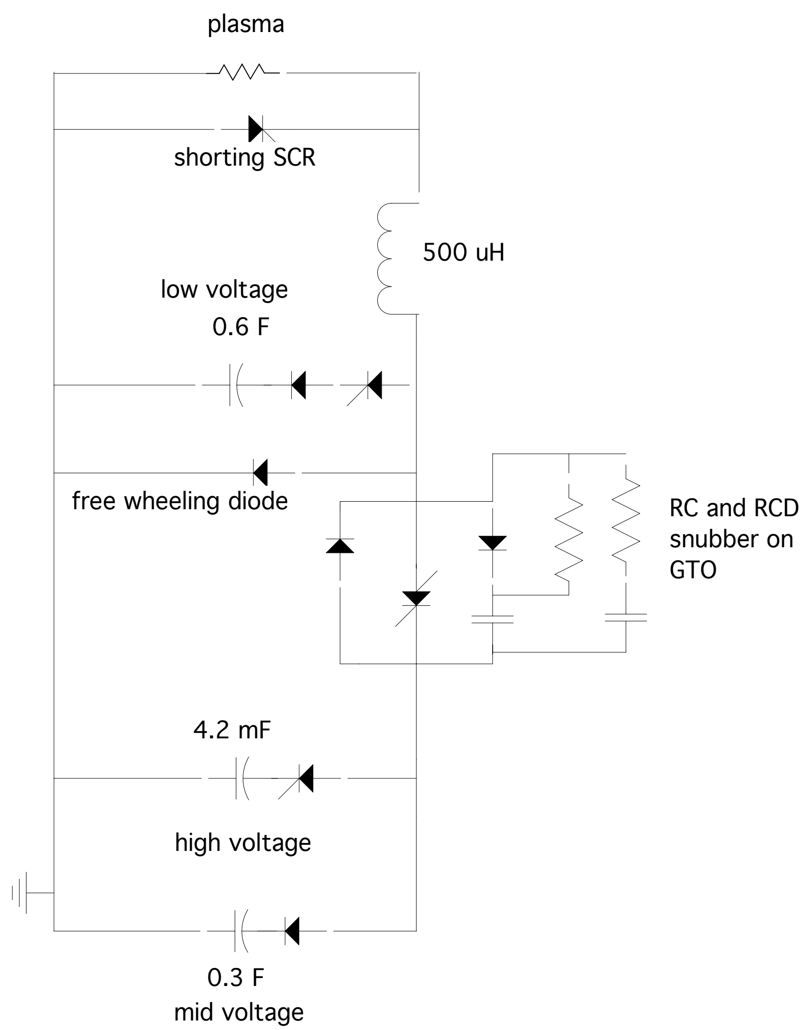

Figure A.1 Layout of circuit in the RWM lab. Note the three capacitor banks in the circuit. Two banks are behind the GTO while one is in parallel with the freewheeling diode. Diodes provide isolation from transient voltages as well as other banks. The .6F, .3F, and 4.2mF banks are the low (LV), middle (MV), and high (HV) banks, respectively.

the slow ramp to the target current. Finally, the flat top is maintained by switching between this secondary supply and a low voltage supply. Comparisons between the current and the output from the waveform generator provide a feedback signal sent to the main switch in the circuit.

A.1 Circuit and Timing

Prior to outlining the different elements of the circuit it is worth pausing to detail the solid state switch at the core of the modified PWM system. The ReWM laboratory utilizes a gate turn-off thyristor (GTO) from Dynex Semiconductor. The particular switches are robust, able to switch over 3000 amps at 4500 volts. The downside to switching this magnitude of power is the time required to open and close the gate. These switches have a minimum permissible off and on time of 100 μs and 50 μs, respectively. The problems surrounding the long switching times will be elaborated below. A GTO is an antisymmetric device and this model can only withstand a reverse bias of 16 volts across the anode and cathode. A large snubber protects the GTO from transient voltage spikes (larger than 16 volts) at turn off.

Figure A.1 shows the fundamental components of the single switch PWM system. The circuit consists of three capacitor banks. The 4.2 mF high voltage bank (HV) and .3 F middle voltage bank (MV) sit behind the GTO and snubber assembly. The large .6 F low voltage bank (LV) is wired into the circuit after the GTO switch and is not directly controlled by the GTO. The HV and LV banks are wired with an SCR in series. The HV SCR mitigates current leakage from the HV bank to the MV bank through the MV diode. The LV SCR is explained below. Critical to the circuit is the 500 μH inductor wired in series to slow down the rise and fall times when the GTO is conducting or non-conducting. The free wheeling diode dissipates the energy stored in the external inductance (that which is outside of the GTO and snubber assembly) back into the plasma when the GTO switches off. The shorting SCR is turned on at the end of the pulse to provide a low resistance path for current flow. This quenches current in the plasma and protects elements in the plasma from a long current ramp down.

The rational for the HV bank is as follows. Without the high voltage supply, the MV bank would be responsible for both powering the current up to and maintaining the flat top. Initial trials

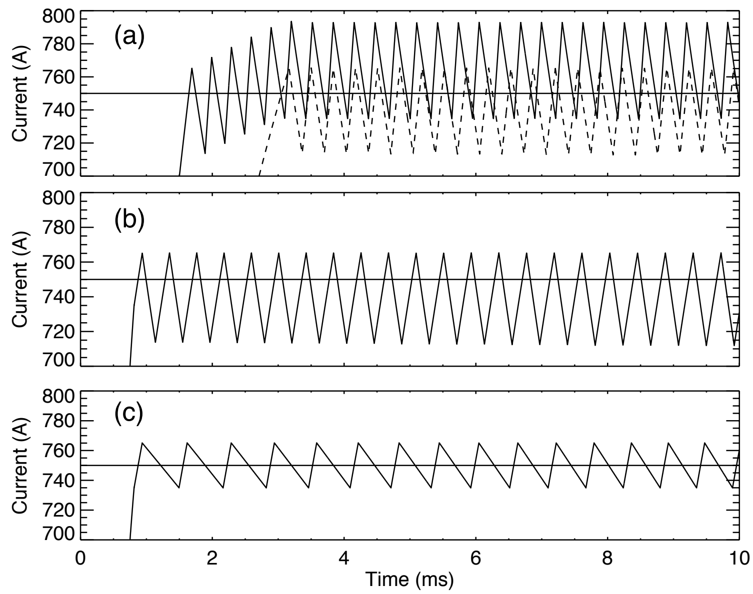

Figure A.2 One can model the characteristics of the circuit assuming an ideal switch and constant resistance. Here, a constant model current of 750A is used. In (a) only the MV bank is energized to 300V (solid) and 200V (dashed). Neither approach is able to simultaneously quickly reach (2ms) and refrain from overshooting the target current. In (b), the addition of the HV bank (600V) to the MV bank (125) in the simulation eliminates the problems in (a). Finally, the LV bank (100V) has been added in (c) to alleviate the drop off in current when the GTO is off. MV at 125V and HV at 600V in (c).

did not utilize the high voltage supply and inherent problems could not be overcome. When the MV bank is charged so as to facilitate a 3 ms ramp to its final value, the flat top is not well maintained. In the flat top phase, the higher voltage necessary for a timely ramp provides an unacceptable current overshoot from the target value. The GTO could not be turned off sooner as it was already being run at its minimum on-time. A shorter on-time would damage the switch. Conversely, should the MV bank be charged to a lower value to mitigate the overshoot in the flat top phase, the time required to ramp up to the target value is too long. These dynamics are modeled in Fig. A.2 (a). The MV bank is charged to 300 V and 200 V for the solid and dashed traces, respectively. Neither trace has a LV or HV bank in the simulation and both are attempting to match a constant current of 750 A. A small amount of high voltage capacitance in parallel with the MV supply solved both of these problems. At turn on the HV supply energizes the system and initiates a fast rise in the current. The small capacitance soon runs out of energy and no longer contributes to the system. At this point the MV bank provides the power to complete the ramp up. As the brunt of the rise was performed by the high voltage bank, a smaller voltage can be put on the MV bank which allows for no overshoot of the target current in the flat top phase of the waveform. In Fig. A.2 (b), with the MV and HV banks at 125 V and 600 V, the simulation shows rapid current rise to the 750 A and reasonable overshoot.

The persistence of large current fall off seen in Fig. A.2 (b) is related to the minimum off-time for the GTO and lead to the necessity of the LV bank. As the GTO on-time contributed to overshooting the target current, a long off-time allowed the current to fall too far below the target value. The initial solution of a larger inductance in the circuit proved troublesome for the start up phase of the pulse because too much energy was required to energize the inductor. A secondary approach of using two switches staggered in their duty cycle offered promise on paper of reducing the current fall off from the target value. This option was never fully explored though as it immediately doubled the cost of the switches. The addition of a large low voltage bank outside the GTO (in parallel with the free wheeling diode) provides a virtual ground across the inductor. Without the LV bank, the voltage across the inductor is whatever the MV bank's voltage happens to be. With the LV bank, a buffer voltage is provided so that the voltage across the inductor is now the differential between the LV and MV banks. A smaller voltage differential causes the current fall-off to have a shallower slope and smaller net loss during turn off. Fig. A.2 (c) simulates the circuit (HV, MV, and LV at 600 V, 125 V, 100 V, respectively) matching a 750 A target with a 2% error.

The small HV bank and large LV bank working in concert with the MV bank create flat top current profiles accurate to within 1% of a target value. A tighter match to a flat top profile requires a smaller voltage spread between the MV and LV banks while a more dynamic profile does well with a larger differential between the banks. It should be noted that the size of the MV and LV banks is larger than needed. The extra capacitance does allow for less voltage drop in the banks

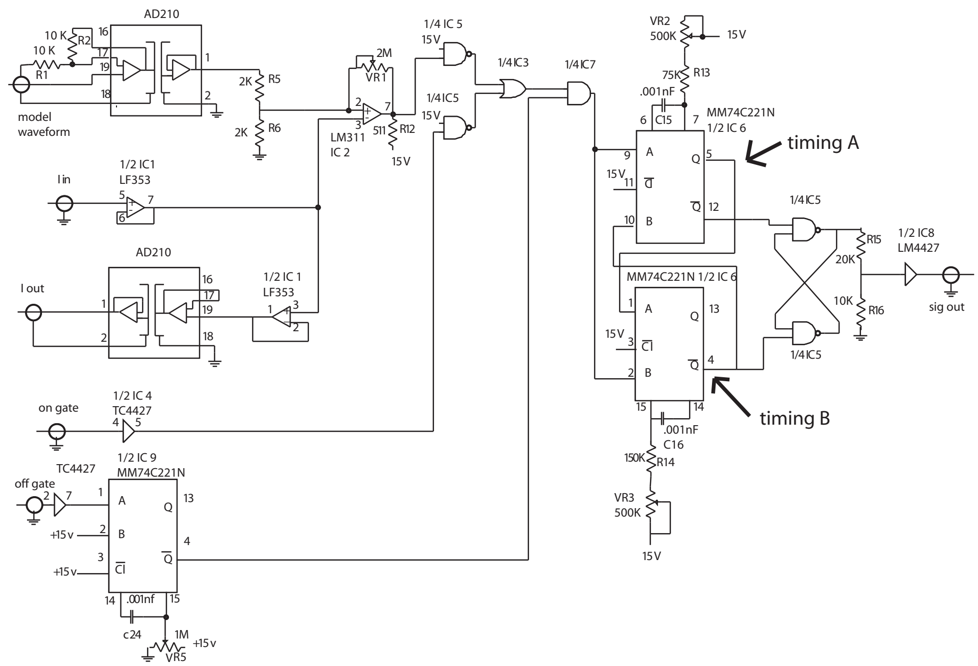

Figure A.3 Circuit board design developed at the University of Wisconsin, consisting of feedback logic and supporting inputs and outputs. I_{in} is a voltage signal from a current shunt in the circuit. I_{out} is a buffered signal of I_{in} sent to a transient digital recorder. The model waveform is a voltage signal from an arbitrary waveform generator. The timing signals (on gate and off gate) and logic they feed into are shown.

throughout a shot; however, smaller banks in conjunction with a larger inductor would provide similar function to the circuit presented.

Triggering the SCRs is controlled by two timed gates that start together but end at different times. The duration of the first pulse, the 'on' pulse, determines the lifetime for which the circuit is trying to follow a model. The positive edge of the first pulse triggers the HV SCR. This coincides with the GTO turning on as well. The LV SCR is sent the second pulse, the 'off' pulse. The off pulse, several hundred milliseconds shorter than the on pulse, continually triggers the LV SCR. Whenever the GTO is turned off the LV SCR sees a positive potential across it and is therefore open. When the GTO conducts the MV bank turns off the LV SCR because it is now reverse biased. The use of a gate to the LV SCR allows it to automatically turn on as soon as the GTO is turned off. The shorter gate to the LV SCR, in conjunction with the GTO being on at the end of the pulse, ensures that the LV SCR will be turned off at the end of the pulse. Finally, the negative edge of the on pulse triggers the shorting SCR in parallel with the plasma. At this point the energy in the inductor is dissipated via line resistance through the shorting SCR and free wheeling diode.

The off pulse facilitates the turn off characteristics for the power circuitry. As mentioned above, the LV SCR must be turned off by the GTO turning on and reverse biasing the LV SCR at the conclusion of the pulse. If the LV SCR were not turned off, there exists the possibility of dumping the stored energy in the LV bank into either the line resistance, plasma, or SCRs outside of the GTO. None of these options are acceptable. The feedback board (discussed below) coordinates with the timing pulses to ensure that the GTO is sent an on signal while the LV SCR is not triggered.

A.2 Feedback

Figure A.3 displays the schematic of the control board, with feedback monitoring, for the GTO. The core function of the PWM circuit to match an external waveform rests in the feedback abilities. The extra capacitor banks only serve to compensate that switching occurs without a H-bridge. The principle switching signal originates at IC2 with the hysteresis set by VR1. The output from IC2 is channeled through logic that incorporates the two timing gates for the circuit mentioned above. The on pulse provides a check that the GTO should obey the result of the feedback. This allows for the possibility that the model waveform is either a constant value, a repeating waveform like a sine wave, or anything that is not pulsed. The negative edge from the off gate signals the impending end to the pulse. After the external logic has been checked the result of the feedback is sent into a timing section on the board.

The GTO could be extensively damaged if a momentary on or off pulse were sent which violated the minimum times. The minimum on and off times for the GTO are maintained at IC6. Here a momentary on signal is forced to be an on signal for the duration of the minimum on time. The same is true for a transient off signal from IC2. IC6 can be wired to perform self checks in addition to those already mentioned. An on or off signal cannot be interrupted or forced to change state. Thus, the GTO is protected from transients issued from IC2.

As described thus far a problem exists in the circuit. If the feedback results in turning the GTO on, IC6 will produce an on pulse of the minimum time. If the feedback has not changed state, that is the current has not reached the target and the switch should still be on, no new on pulse will be formed because IC6 is edge triggered. The on pulse will end after the minimum time and the signal to the GTO will actually transition from on to off. The addition of the two nand gates inter-wired ensures that the logic to the GTO will only change state when a new pulse is sent to the nand gates. Continuing with the previous example, even though the on pulse will end, the output of the nand gates will not change state until an off pulse is initiated from IC6. Because the nand gates are edge triggered, the output to the GTO will change state immediately.

The interplay between the minimum switching times, output to the GTO, real current, and output from IC2 is seen in Fig. A.4 for a hypothetical current. This current waveform is not achievable with the circuit described, but is chosen to highlight different logic paths in the feedback board. In Fig. A.4 (a) the model current, its accompanying error (set by hysteresis at VR1), and real current are shown. In Fig. A.4 (b) different timing values are shown and should be read in conjunction with events in panel (a). The output from IC2 with its hysteresis is easiest to understand in that it is similar to a running comparison between the real and model current. On the up slope, IC2 reads high until the real current has passed above the upper level of hysteresis. Conversely, it reads low while the current is falling from the upper error to the lower error. When the real current reaches the lower level of hysteresis, the output from IC2 is again high. This is true no matter how quickly the real current is rising or falling. Towards the end of the pulse, one can see that the output of IC2 can be very short if the real current is rising or falling quickly. This highlights the problem with using the output of IC2 to directly trigger the GTO. The output may be shorter than then the minimum on or off times.

To protect the GTO the output from IC2 is fed into IC6 which has the minimum times hard wired into it. The labels of timing A and B are the outputs from IC6 which are then fed into the nand gates. The final output from the nand gates is the output to the GTO. Timing A and B are

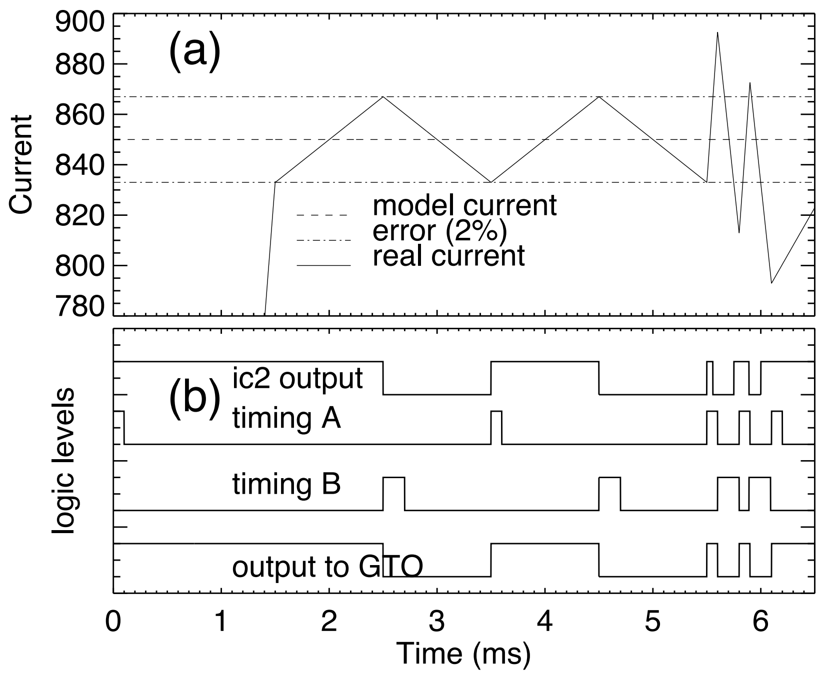

Figure A.4 In (a) a mock current is plotted in conjunction with a realistic target (750A) and error. In (b) the accompanying responses from the feedback board. From 0 to 5.5 ms the switching is governed by the error levels. After 5.5 ms the minimum on and off times control the GTO. In the later phase, the mock current cannot be maintained within the error levels.

pulsed outputs related to the minimum on and off times. The length of each gate is hard wired and will not change, thus the pulse lengths are static. For the first 5 ms one can see the simple interplay between the four signals. When IC2 goes high, timing A issues a high pulse, which goes through the nand gates to the GTO output. When IC2 is low a high pulse is issued from timing B. The edge of timing B allows the nand gates to change state and the GTO is signaled to turn off. The GTO will stay off until the nand gates change state which will only occur when timing A is again high. This happens when IC2 goes high around 3.5 ms. Until the real current begins rising and falling rapidly (around 5.5 ms) the GTO switching is determined by the hysteresis of VR1. The time required for the real current to rise or fall through the error region is longer than the minimum times.

After 5.5 ms the GTO switching is governed not by the hysteresis levels but the minimum on and off times. Because of this, the real current goes beyond the error levels. The behavior of IC2 has not changed; however, its interaction with timing A and B has. At 5.5 ms IC2 goes high which pushes timing A and the GTO output high. Now though, IC2 is low before the minimum time. The minimum time keeps the GTO on. At the end of the minimum on time, IC6 has a low signal from IC2 and a negative edge from timing A. This edge from timing A now triggers a pulse from timing B which turns off the GTO. The reverse is presented at $t \approx 5.7$ ms. Here IC2 goes high, but the minimum off time has not been reached. After the minimum off time, IC6 has a high signal from IC2 and a negative edge from timing B. The edge on timing B, while IC2 is high, initiates the pulse from timing A.

The logic after IC2 plays a role when the pulse is about to terminate. The negative edge of the off pulse initiates a .5ms pulse from IC9. This pulse goes through IC6 and the nand gates to force the GTO on. At the conclusion of this .5 ms pulse the on gate is now terminated. The GTO is forced on for the final .5 ms of the pulse and then forced off regardless of what the logic condition at IC2. Note then when the off pulse ends, the triggering gate to the LV SCR will also end. The shut off of the LV bank is ensured because the GTO is forced on at the end (reverse biasing the LV SCR) of the pulse while the LV SCR is off.

A.3 Application of Modified PWM System

In figure A.5 the current profile and GTO switching duty are shown for the circuit when it is matching a constant model current. In this case the circuit is attempting to match a 980 A flat top with no ramp up phase. With the high voltage bank, this waveform reaches the target current in 1.3 ms. This shot had a tight voltage spread between the MV and LV banks to minimize any peak to peak errors in matching the model current when turning the GTO on or off. Over the length of the pulse there is a drop of about 7 amps (0.714% over the total of 980 amps) which is partially attributed to losing driving voltage in the LV bank during the shot. The actual error of overshooting the model current can be seen at 6.2 ms. At that feature, the current rises from 970A to 980A, a change of 10 amps or 1.0% peak to peak. It should be noted though that this feature is the worst

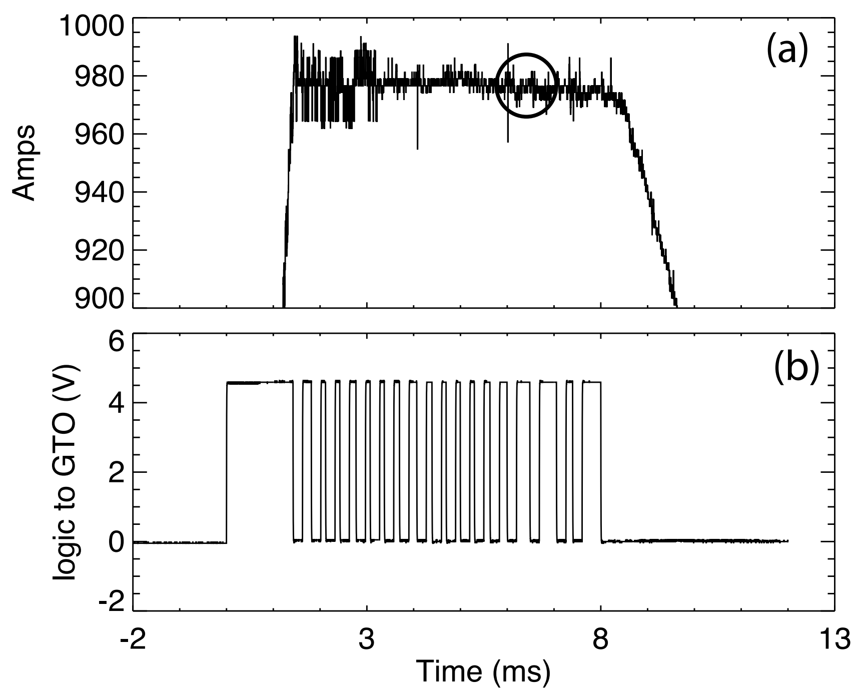

Figure A.5 In (a) the modified PWM circuit when the feedback board is fed a DC voltage that corresponds to a target current of 980 amps. Below in (b), the switching signal from the feedback board to the GTO. The high, middle, and low voltage banks are charged to 600, 180, and 165 volts, respectively. Note that the target current is reached well within 2 ms with the help of the high voltage bank. The narrow spread between the LV and MV banks allows for tight matching of the target value. Peak to peak error (highlighted by circle) is less than 1%.

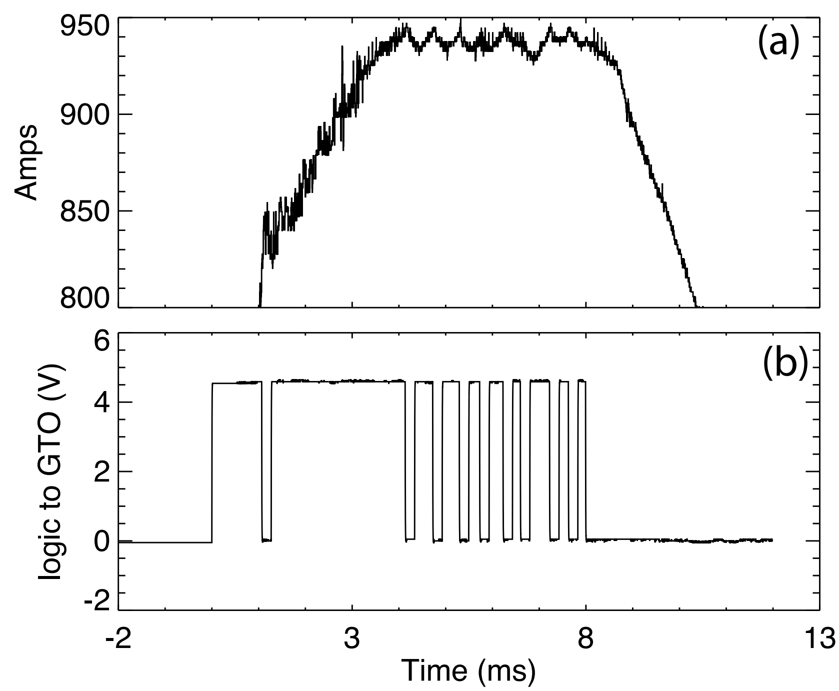

Figure A.6 The modified PWM circuit is now following a dynamic waveform created by a programmable pulsed arbitrary waveform generator. The current trace is shown in (a). The profile fed to the circuit differs from a simple flat top by the addition of the ramp-up from 800 amps to 950 amps. The high, middle, and low voltage banks are charged to 585, 180, and 135 volts, respectively. The switching signal to the GTO is seen in (b). Note that the high voltage bank reaches the target value of 800 amps in 1 ms. The GTO turns off once it reaches the ramp, at 1 ms, but then turns on again because the current in the circuit has not reached the model value.

case scenario in this shot. Careful inspection of the pulse between 2.5 and 4.5 ms reveals the peak to peak error associated with switching the GTO is within the noise level of the data. The high frequency features at the onset of the flat top are noise associated with the initial turn-off of the GTO. It is a combination of bit noise at the digitizer and noise pickup at the current shunt in the circuit. The modified pulse width modulation system can match a flat top to within 1% peak to peak at high current.

As an aside it is worth mentioning that the model waveform used for this pulse did not originate from an arbitrary waveform generator. Rather the source is a simple adjustable DC voltage supply. In this pulse the on timing gate is actively turning the GTO on instead of the output from IC2. Recall that the output from IC2 is subservient to the on timing gate. The utility of this control scheme rests in its simplicity and cost effectiveness. Spare voltage supplies are in abundance in many labs.

Figure A.6 shows the current and GTO switching profiles as in fig. A.5 for a pulse with a ramp up to a final target value. In this pulse the model waveform started at 800 A and was ramped to 950 A in 4 ms. There were some slight offsets between the model and actual current such that the ramp in the shown waveform is from 810 A to 945 A. This is a result of calibration errors in the feedback circuit when paired with a different source for the model waveform. Figure A.6 shows a clear ability to follow a dynamic waveform by varying the duty cycle for the GTO. A larger peak to peak error is seen in the flat top region ($\approx 3\%$) of the pulse and is a direct result of a higher voltage on the MV bank. This elevated voltage is a requirement because the MV bank must provide the energy to bring the current up to the target value from the beginning of the ramp-up.

In both Fig. A.5 and Fig. A.6 the shorting SCR has not been installed in parallel to the plasma in the circuit. The result of this can be seen in the current profiles after the GTO has been turned off in the pulse. In both profiles, the current is still at 80% the target value 2 ms after the final turn-off. This slow current decay may be acceptable in other applications but could damage this circuit.

As mentioned in the introduction this circuit was developed for a plasma laboratory which needed a cost effective method to control high current pulses. Furthermore, the laboratory needed

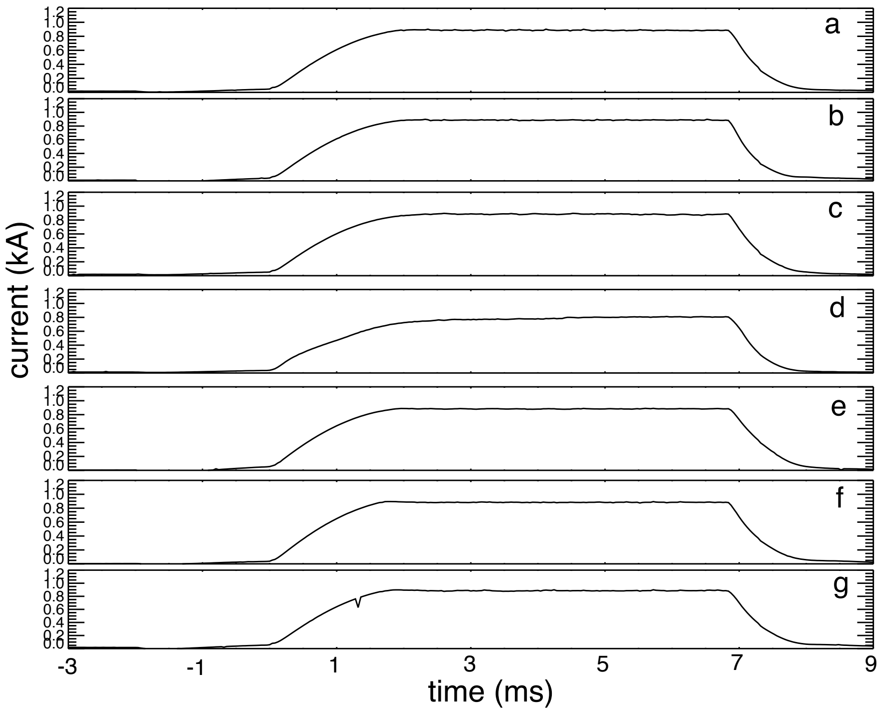

Figure A.7 The seven current profiles for circuits a-g when matching a DC voltage signal corresponding to 875 amps. The high, middle, and low voltages for each bank are roughly charged to 450, 140, and 90 volts, respectively. Here the shorting SCR's functionality is seen in the rapid current fall off in each profile. This feature serves to protect components of the circuit relating to the plasma interface.

not one such circuit, but seven. This brought about the concern of crosstalk between separate circuits. Figure A.7 shows the current traces from seven independent circuits that have been fed the same model waveform, in this case a flat top. In this example, the shorting SCR has been added to the circuit and a prompt mitigation of current can been seen within 1 ms on all current waveforms at the conclusion of the pulse.

Figure A.8 displays the switching signals being sent to each of the seven GTOs. The independent switching seen in Fig. A.8 is particularly encouraging in that it indicates the ability to alter the duty cycle of each GTO to its waveform and environment. Here the longer start up phase of the central current profile, seen by its long initial GTO on pulse is a result of that circuit having a

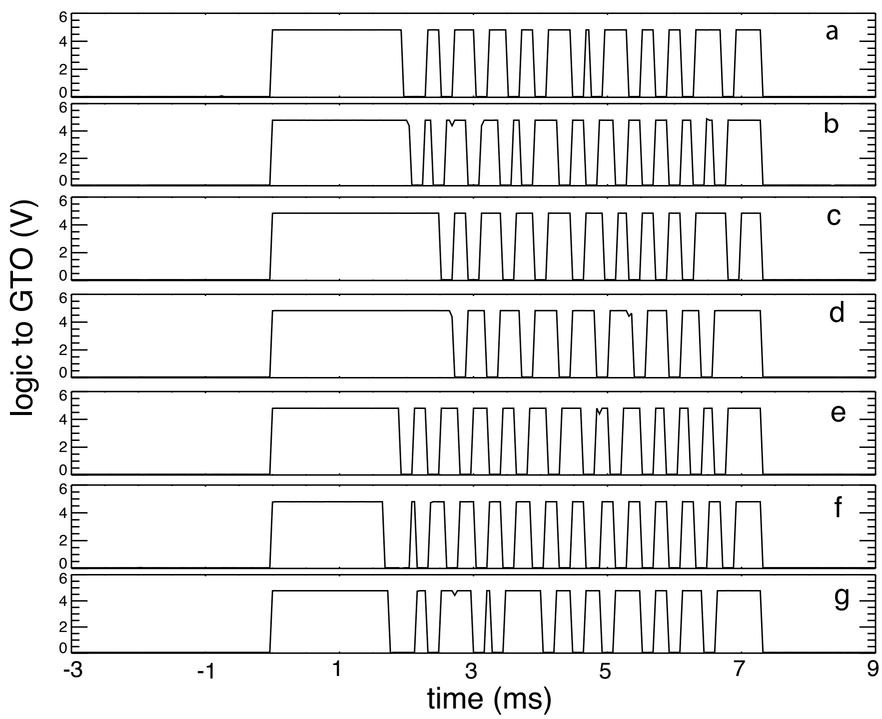

Figure A.8 Traces of the switching logic sent to each of the seven GTOs in a-g. While each feedback board is sent the same model, feedback is independent for each circuit and allows for discrepancies in the switching profiles.

higher impedance. Conversely, the consistently short on pulses seen in fig. A.8 (f) is a result of that circuit's MV bank being charged 15 V higher than all other MV banks.

All feedback boards are mounted in one box and current monitoring is through 75 ft co-ax cables wired into current shunts. The inductors for all seven circuits are located next to one another. Coupling is minimized by mounting the inductors ninety degrees out of phase with one another. Despite these constraints excellent profiles are achieved without any crosstalk problems.

Appendix B: Signal Analysis and Expected Eigenmodes

Plasma dynamics can be studied with a simple spectrogram. A spectrogram is a contour plot created from a series of power spectra calculated throughout a shot from a single magnetic flux loop. The power spectra are generally calculated with low resolution (≈ 1 kHz), but one after another. A sequence of these spectra reveals what frequencies are present in the plasma and how they evolve throughout the shot.

There are different approaches to mode identification and spectrograms provide a starting point for visual identification. Unprocessed, the B_r trace looks muddled (see Fig 4.4 (c)) because it is a jumble of different frequencies. Numeric filtering and reconstruction of the signals after the shot eases identification by disentangling the individual modes. Applying a band pass filter to a peak in a power spectrum isolates a narrow range of frequencies. Reversing the power spectrum calculation on this selected range of frequencies recreates a signal of B_r. Capturing a particular frequency range in B_r is analogous to looking at a distinct mode in the original recording. Repeating this analysis on all 80 B_r coils can create a global measurement of each mode. With the full two dimensional coverage of B_r, eigenmode characteristics are straightforward to identify. A contour plot is created at a single point in time with all 80 B_r coils. Examples can be seen in Fig. 4.5 and Fig. 4.6.

Fourier transforms in periodic systems are a natural tool for mode identification. Partially this stems from there being a clear fundamental wavelength in the system. The periodicity in the azimuthal direction of a cylindrical geometry creates a fundamental wavelength related to the circumference. In the ReWM, the 10 poloidal flux loops allow modes from $m = 0$ to $m = 4$ to be identified. Torii support the same argument for the toroidal mode number, n. However, Fourier transforms are ill posed to identify the toroidal mode in a line tied system. For the sake of analysis, one can impose a fundamental wavelength for the system and perform the Fourier transform. One needs only to supply the fundamental wavelength, a surprisingly murky proposition. Arguments from acoustic physics offer some illumination into the choice of wavelength. Sound wavelengths

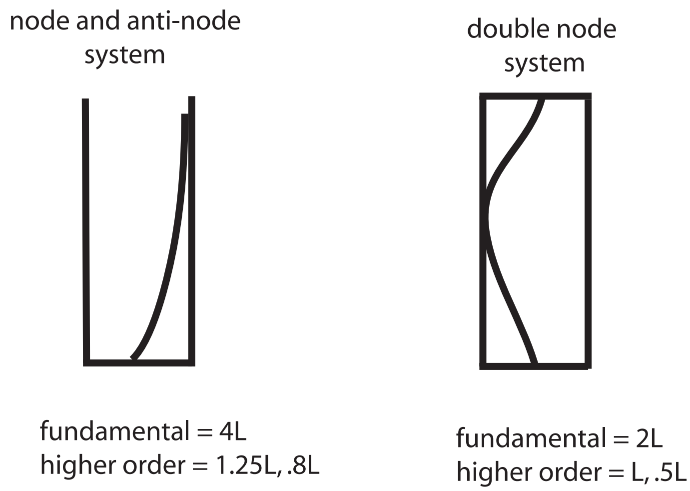

Figure B.1 A reminder of allowable acoustic wavelengths in pipes. At left, a pipe with both a node and anti-node. At right, a pipe with only nodes. The environment of the ReWM may produce similar nodes and anti-nodes for the magnetic signals.

in pipes are the classic example in which the fundamental standing wave is governed by the ends being nodes or anti-nodes. Figure B.1 refreshes these considerations.

Experimental considerations of the ReWM offer additional insight into the question of axial eigenmodes. The union of the cylindrical plasma region with the end chambers, seen in Fig 3.1, is a vacuum seal. In order to accomplish the seal, large flanges are affixed to the end chambers. In practice, these metal flanges inductively respond to magnetic changes from the plasma and act to cancel changing magnetic fields close to them. While the flanges are made out of resistive stainless steel, they are many centimeters thick and have a decay time longer than the lifetime of the plasma. Flange effects would limit the ability to accurately measure nearby B_r signals as some of the magnetic field would be canceled by the flange.

A second experimental consideration yields a different conclusion. The plasma is not symmetric about the plane defined by $L = 0.6$ m. The cathode array holds the plasma production source and by definition, limits the physical location of the plasma. At the anode, there is no corresponding mechanism to restrict or limit the plasma. From this viewpoint, it is not clear that the ends would behave in a uniform fashion. Indeed, returning to the organ pipe example, the cathode is clearly a node while the anode might be an anti-node. The resulting fundamental would be four times the length of the plasma.

The physics of a line tied cylinder are more subtle than determining what standing wave will be supported by the cylinder. Much of the complexity in line tied plasmas stems from determining a good basis function that accurately captures the critical end dynamics of line tying. Hegna's analysis in Reference [28] allows one to construct individual eigenfunctions of B_r for the ReWM. The model constructed therein is based upon a plasma represented by ideal MHD with a force-free equilibrium, $\nabla p_0 = 0$, and a heaviside step function to describe the current profile. The induction equation is

$$\tilde{\mathbf{B}} = \nabla \times \left(\tilde{\xi} \times \mathbf{B_0}\right) \tag{B.1}$$

where $\tilde{\xi}$ is expressed in Equation 2.22. From Equation B.1 B_r simplifies to

$$\tilde{\mathbf{B_r}} = \mathbf{B_z}\frac{\partial\tilde{\xi}}{\partial z} + \frac{\mathbf{B}_\theta}{r}\frac{\partial\tilde{\xi}}{\partial\theta} - \tilde{\xi}\frac{\partial\mathbf{B}_\theta}{\partial r}. \tag{B.2}$$

Individual eigenfunctions of $\tilde{\xi}$ can be constructed when machine parameters are substituted into Equation 2.22. These eigenfunctions can in turn be used in association with equation B.2 to plot profiles of $B_r(z)$. Such a calculation has been performed in Figs. B.2 ($n = 1$) and B.3 ($n = 2$). For the calculations the plasma parameters chosen were $a = .08$ cm, $I_p = 7000$ A, $B_z = 100$ G, and $L = 1.2$ m. In these figures, both $B_r(z)$ and $\xi(z)$ are plotted. A cursory examination reveals that line tied eigenmodes are not like Fourier eigenmodes. While $\xi = 0$ at $L = 0, L = 1.2$, B_r is not forced to zero at the ends. This is a common misunderstanding concerning line tied plasmas. Line tying does not mandate that $B_r = 0$ at the endplates, only that $\xi = 0$. It is incorrect to assume that a line tied plasma would have a fundamental wavelength equal to the length of the system. Inspection of Fig. B.2 shows that the wavelength of B_r is close, but not exact, to the machine length. These eigenfunctions are only valid in the simplified model of the ReWM; yet, the current profile in the ReWM differs from this model and is discussed further in Section 6.4. While the eigenfunctions shown only approximate the ReWM conditions, they are a starting point.

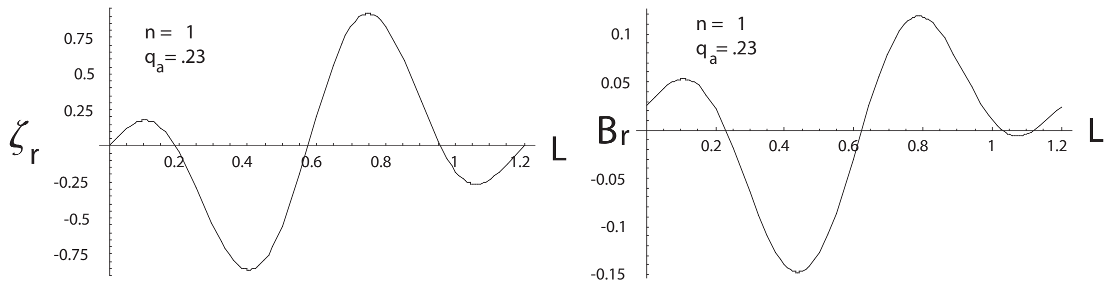

Figure B.2 The predicted eigenmode of ξ_r and B_r for a plasma with I_p = 7000 A, B_z = 100 G, a = 8 cm, and $n = 1$. With these parameters, $q_a = .23$. Note that ξ_r goes to zero at the ends of the machine, while B_r is close but not equal to zero. The wavelength of B_r is close to a full period, but line tying introduces slight deviations.

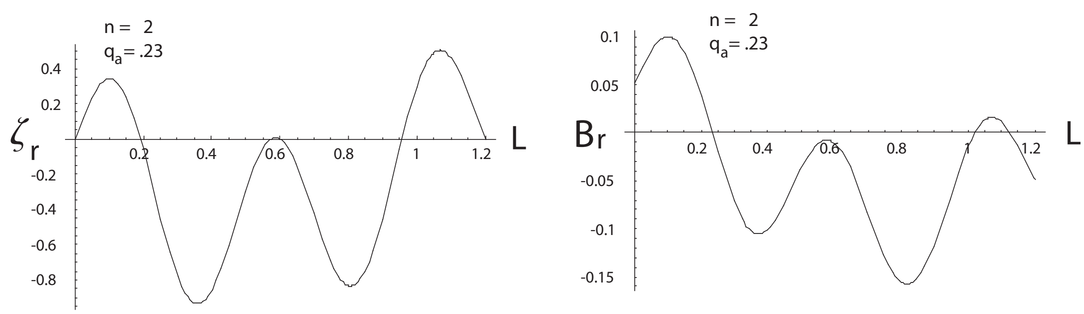

Figure B.3 The predicted eigenmode of ξ and B_r for a plasma with I_p = 7000 A, B_z = 100 G, a = 8 cm, and $n = 2$. With these parameters $q_a = .23$. Again note that only ξ_r goes to zero at the ends, and that the B_r eigenmode is not simply two full periods.

Appendix C: The Ferritic Wall Mode

Interest in ferritic materials has grown in recent years because of their low activation from neutron radiation and ability to act as a magnetic shim to adjust magnetic field profiles. A major concern in working with ferritic materials though is mode destabilization. The analog of the RWM is the Ferritic Wall Mode (FWM), a $m = 1$ external kink whose stability is dependent upon both the wall time of the material and its relative permeability, μ. In high field applications, like a tokamak, $\mu \approx 2$ as the ambient field strength leaves the ferritic material nearly saturated. In the ReWM, the field strength is much lower and relative permeability correspondingly higher. In general, the magnetic wall destabilizes external kinks because it pulls flux into it.

C.1 Theoretical considerations

Kurita performed the initial analysis of the FWM in Reference [35] in relation to its effect on the $\beta-$limit in tokamaks. The main result from the analysis finds the FWM reduces the $\beta-$limit by about 10%. Kurita's analysis considers a long cylinder with plasma constrained within radius a, and vacuum region between the plasma and wall at radius b. The wall is considered to be thin, resistive, and magnetic. The thin wall approximation is applied and the steps in the analysis are similar to those in Chapter 2 for the RWM analysis. Because the relative permeability of the wall is not equal to one, the matching conditions for B_r across the wall are different from those reported in Chapter 2.

The growth of the FWM in the model described above is reported as

$$\gamma\tau_w = \Gamma_w + \Gamma_\mu, \tag{C.1}$$

where

$$\Gamma_w = \frac{\alpha}{(a/b)^{2m} - \alpha}, \tag{C.2}$$

$$\Gamma_\mu = \left(\frac{m\delta}{2b}\right) \frac{\alpha(\hat{\mu} + \hat{\mu}^{-1} - 2) + (\hat{\mu} - \hat{\mu}^{-1})(a/b)^{2m}}{(a/b)^{2m} - \alpha}, \tag{C.3}$$

with $\hat{\mu} = \mu/\mu_0$ and $\alpha = (\Delta_a^* + 1)/(\Delta_a^* - 1)$. Δ_a^* is analogous to Δ_+ in Chapter 2 in that it contains information about the jump condition at the wall and geometry of the system. For the long cylinder $\alpha = nq_a - m + 1$.

The analysis as it stands is only marginally applicable to the ReWM. As has been discussed previously, finite length cylinders have subtle differences from long periodic cylinders in terms of mode stability. Fortunately, the independent analyses of Kurita and Hegna from Reference [28] can be joined to consider the stability of a finite length multiple wall system where one of the walls is magnetic. From Equation C.1 it can be seen that the growth of the mode is separable into resistive and magnetic components. Hegna's work allows one to take into consideration two resistive walls, while Kurita's compensates for one of the walls being magnetic. One needs only to determine the correct form of α. This can be accomplished by setting the expression for Γ_w equal to

$$\frac{1 - q_a}{q_a - 1 + \left(\frac{a}{b}\right)^2}. \tag{C.4}$$

and solving for α. Equation C.4 is essentially the single wall RWM growth from Chapter 2. Solving for α in the above allows one to express α in terms of a finite length cylinder and,

$$\alpha = 1 - q_a. \tag{C.5}$$

Returning to Equation C.3, the correct form of α can be substituted into the expression. Γ_w is essentially the expression for RWM growth with two walls.

Finally, the growth of the FWM in a finite length cylinder with two resistive walls present, one of which is magnetic is

$$\gamma = -\frac{1}{\epsilon}\left[\frac{1}{\tau_c} + \frac{X_c}{\tau_b X_b}\right] \pm \frac{1}{\epsilon}\sqrt{\left[\frac{1}{\tau_c} + \frac{X_c}{\tau_b X_b}\right]^2 - \frac{4X_\infty \epsilon}{X_b \tau_b \tau_c}} + \left(\frac{\eta}{\mu_0 c^2 \pi}\right)\frac{\alpha(\hat{\mu} + \hat{\mu}^{-1} - 2) + (\hat{\mu} - \hat{\mu}^{-1})(a/b)^{2m}}{(a/b)^{2m} - \alpha}, \tag{C.6}$$

where the resistive wall is at b and magnetic wall, with resistivity η at c. The first two terms in Equation C.6 describe the growth of the mode from the resistive effects of the walls and is identical to Equation 2.37. The final term in Equation C.6 is similar to Γ_μ from above however the factor in front corrects the dimensionality and α corrects for a finite length cylinder. It should be noted that Equation C.6 only models two walls. In reality the ReWM, shown in Section C.2, has three walls.

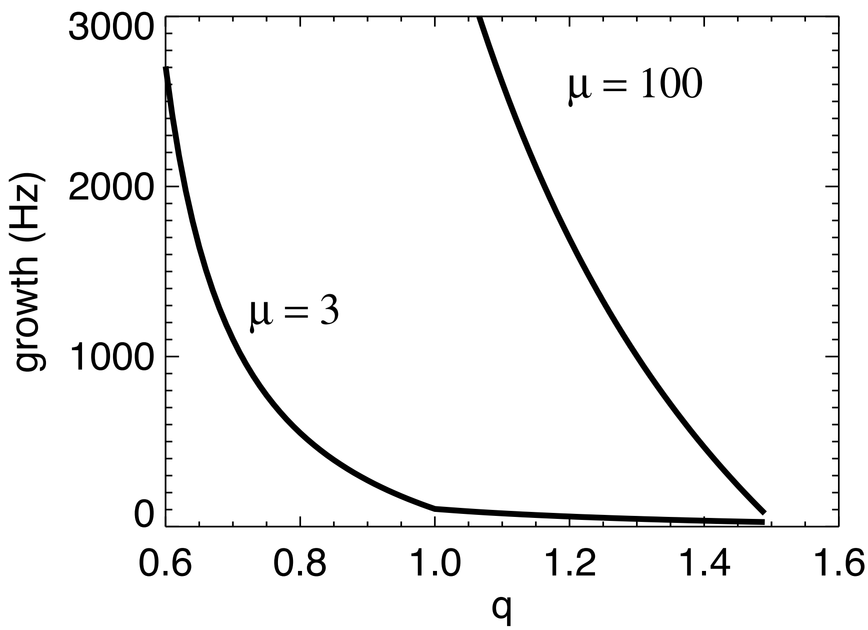

Figure C.1 Growth rates predicted for the FWM in a line tied pinch. The plasma radius a = 7 cm, a copper wall at radius $b = 9.8$ cm and magnetic wall at radius $c = 10$ cm. The wall time $\tau_w \approx$ 7 ms. The FWM onset occurs at a higher value of q_a in either case; however, at low μ the growth is dominated by the RWM effects. Conversely, at high μ mode growth is determined by magnetic effects.

There is a stainless steel wall at b, a copper wall at c, and a magnetic wall at d. The stainless steel wall at b is ignored in the analysis as its resistivity is effectively muted by the copper wall.

In Fig. C.1 the predicted growth of the FWM is shown when μ = 3 and 100. The mode onset occurs at a higher value of q_a than the RWM and demonstrates the destabilizing effect of placing a magnetic material close to the plasma. The value of q_{onset} is determined by the wall location in relation to the plasma radius. When μ = 3 the resistive wall effects dominate the FWM growth and a change in the growth occurs when $q_a < 1$. The opposite is true when μ = 100. Here the magnetic nature of the wall dominates the FWM growth.

In Fig. C.2 the growth rates of the RWM and FWM are plotted together. For the RWM two scenarios are presented, a single stainless steel wall ($\tau_w \approx .5$ ms) and stainless steel and copper wall ($\tau_w \approx 7$ ms). The FWM is measured in association with a copper and magnetic wall ($\mu = 1200$). Perhaps the most important conclusion to draw from Fig. C.2 is the wide separation in mode onset

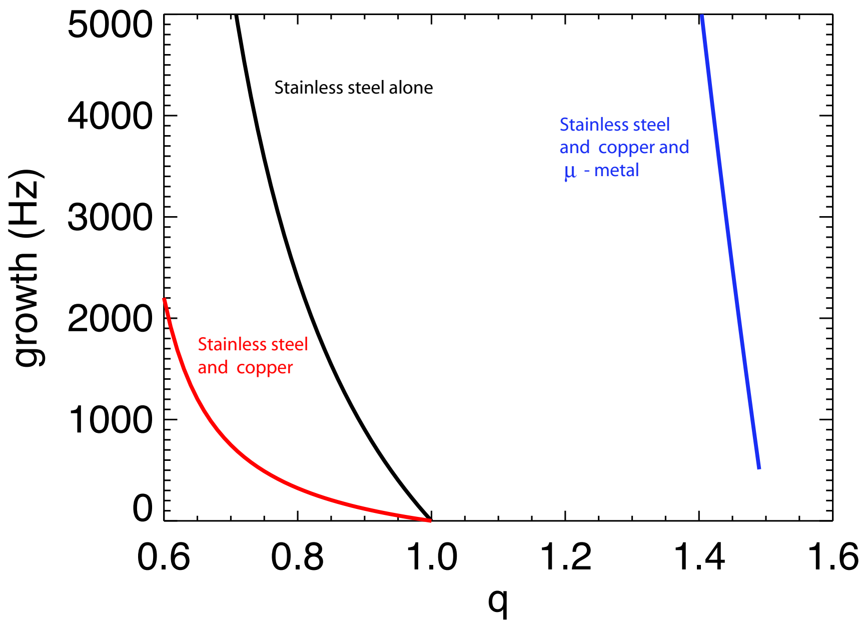

Figure C.2 Growth rates predicted for the FWM and RWM in a line tied pinch. For the calculations, the stainless steel wall time is ≈ .5 ms, the wall time for the copper and stainless steel wall is ≈ 7 ms, for the copper and magnetic wall μ = 1200. The FWM onset occurs above $q_a = 1$ and grows quickly.

and growth when a magnetic wall is present. This presents the possibility of clearly observing the FWM.

C.2 Experimental Observations

The ReWM has been modified to accommodate an experimental investigation of the FWM. Figure C.3 depicts the addition of a thin magnetic material just outside the stainless steel and copper walls. The magnetic material is Netic and has known DC permeability properties. In a 300 G field $\mu = 1200$ for this material. The wall time of the system is dominated by the copper shell and $\tau_w \approx 7$ ms.

In order to determine if any mode activity is present in the plasma it is often instructive to conduct a current scan and monitor the amplitudes of the $m = 1$ and $m = 2$ mode. Figure C.4 plots the results of such a scan. The $m = 2$ mode amplitude is essentially linear with plasma

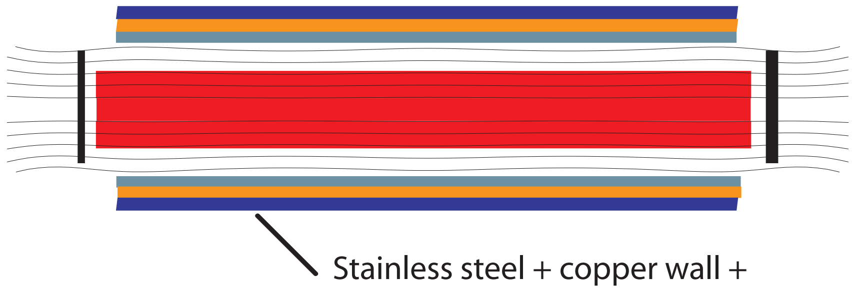

Figure C.3 The ReWM has been modified from the RWM studies with the addition of a thin layer of magnetic material outside the stainless steel and copper shells.

current. This result is in keeping with the $m = 2$ signature resulting from residual field errors in the machine. The $m = 1$ amplitude is linear until a critical current is surpassed. At this point there is a signal present in addition to the field error portion of the amplitude. This extra signal is thought to be the FWM.

The time history of a single shot with the FWM present is instructive in separating the plasma mode from the field errors. In Fig. C.5 such a shot is plotted. In (a) the amplitudes of the $m = 1$ and $m = 2$ modes are plotted, while in (b) the phase of the two modes is shown. In (c) the q profile is shown as measured from the three sections of the anode. Note that the $m = 2$ mode amplitude and phase are static in time. The $m = 1$ mode through is growing just after the bias circuit is fired. This strongly indicates that the measurement is not a field error. Moreover, the phase of the $m = 1$ mode rolls over from one orientation at the beginning of the shot to a different phase for the majority of the pulse. The change in phase is indicative of a transition from a signal dominated by field errors to plasma MHD.

Finally the measurement of the FWM growth from a series of shots is presented in Fig. C.6. The mode begins to grow when $q_a = 1.5$. These plasmas were created with the central guns pulsed, thus $q_{r=5cm}$ approximates the value of q_a. When the mode is first observed, the growth is 1.5 kHz. As q is lowered, the mode is seen to grow at a quicker rate; however, the mode growth is far lower than predicted from Fig. C.2.

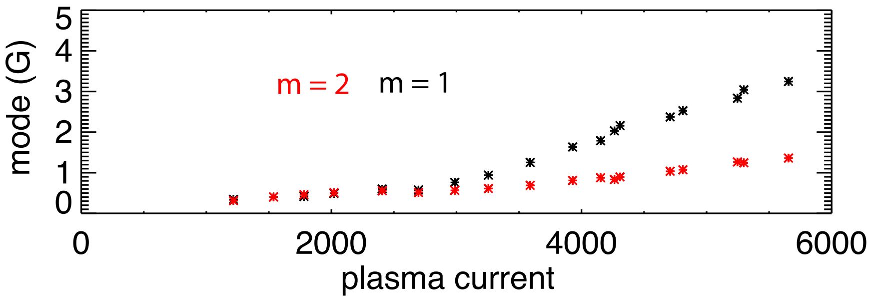

Figure C.4 A current scan which depicts the $m = 2$ mode amplitude is linear with plasma current. The $m = 1$ mode amplitude is also linear with plasma current until a critical current is reached at which point the $m = 1$ amplitude has both a field error portion and FWM portion.

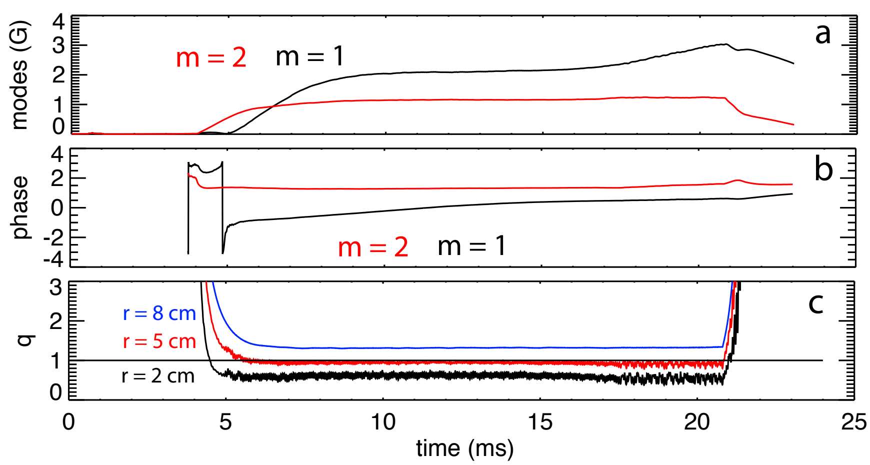

Figure C.5 The time history of a shot with the magnetic wall present. In (a), the mode amplitudes for $m = 1$ and $m = 2$. In (b) the phase of the modes from (a). In (c) the value of q in the machine as measured from the segmented anode. Note the $m = 2$ mode is static in phase and amplitude while the $m = 1$ mode has dynamics in both.

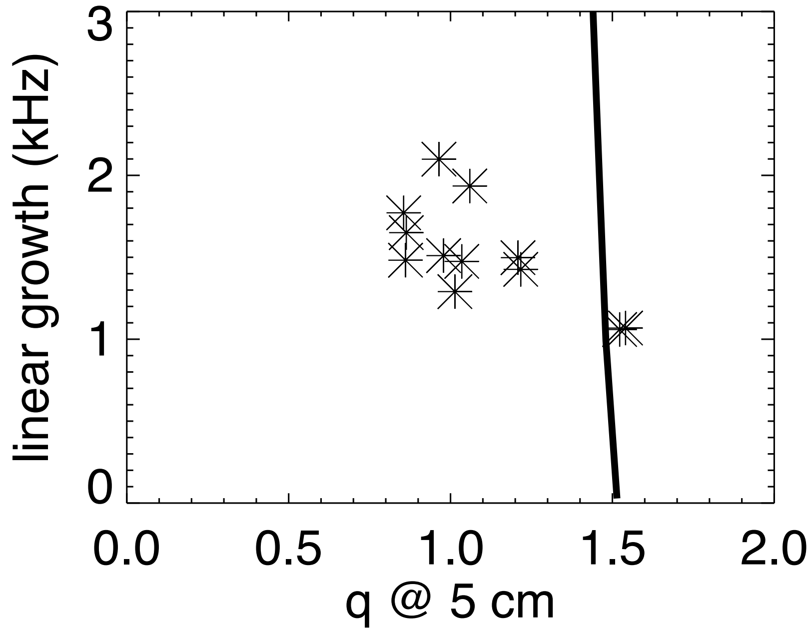

Figure C.6 Comparison of the measured and predicted growth rates for the FWM in the ReWM.

C.3 Discussion

The onset of the mode and its initial growth are in good agreement with predictions; however, the subsequently slower growth is not all in keeping with the predicted growth rates. That the only addition to the ReWM of a thin magnetic wall causes fast mode onset at a comparably higher q_a suggests this mode is the FWM.

The frequency response of the magnetic wall is unknown. It is safe to assume that as the frequency increases the value of μ decreases. Moreover, the time scale of the problem is difficult to determine. The growth of the mode is fast (1.5 kHz), yet the mode is present throughout the lifetime of the shot ($\approx$ 100 Hz). The FWM dynamics may be less dependent on μ at lower q_a. A natural cause would be a mode growing rapidly enough to outpace the μ effects. With sufficient rotation a resistive wall appears ideal. An analogous situation may exist with the FWM in terms of growth, not rotation. This dynamic quality of μ may be responsible for the observed growth rates.